DYNAMICS AND SPECTRAL ANALYSIS OF LASER PRODUCED PLASMAS IN THE PRESENCE OF EXTERNAL MAGNETIC FIELD

A Thesis submitted
in partial fulfillment for the Degree of

Doctor of Philosophy

by

MAKARAJU SRINIVASA RAJU

Department of Physics

INDIAN INSTITUTE OF SPACE SCIENCE AND TECHNOLOGY

THIRUVANANTHAPURAM

JULY, 2015

CERTIFICATE

This is to certify that the thesis entitled **Dynamics and Spectral Analysis of Laser Produced Plasmas in the Presence of External Magnetic Field**, submitted by **Makaraju Srinivasa Raju**, to the Indian Institute of Space Science and Technology, Thiruvananthapuram, in partial fulfillment for the award of the degree of **Doctor of Philosophy**, is a *bona fide* record of the research work done by him under my supervision. The contents of this thesis, in full or in parts, have not been submitted to any other Institute or University for the award of any degree or diploma.

Dr. Pramod Gopinath

Supervisor

Department of Physics

Place: Thiruvananthapuram

July, 2015

Counter signature of Head,

Department of Physics with seal

DECLARATION

I declare that this thesis entitled **Dynamics and Spectral Analysis of Laser Produced Plasmas in the Presence of External Magnetic Field** submitted in partial fulfillment of the Degree of Doctor of Philosophy is a record of original work carried out by me under the supervision of **Dr. Pramod Gopinath**, and has not formed the basis for the award of any other degree or diploma, in this or any other Institution or University. In keeping with the ethical practice in reporting scientific information, due acknowledgements have been made wherever the findings of others have been cited.

M Srinivasa Raju

SC10D010

Place: Thiruvananthapuram

23/07/2015

ACKNOWLEDGEMENTS

The thesis would not have been possible without the help of several people. I acknowledge the Supreme Power for providing the companion of such a people.

First and foremost I offer my sincerest gratitude to my research supervisor, Dr. Pramod Gopinath, who has supported me throughout my Ph.D. with his profound knowledge, kindness and personality. Without his able guidance, this thesis would not have been possible.

My sincere thanks to Prof. Ajai Kumar, Group Leader, Plasma Diagnostics Development Group, IPR for giving an opportunity to join his team, for giving access to the research facilities and providing all necessary logistic support. Without his precious support it would not have been possible to conduct these experiments. I thank Dr. R.K. Singh, IPR for enlightening me the first glance of experiments which helped a lot to conduct my experiments. His brotherly support was appreciable. I thank Jinto Thomas, Vishnu Chaudhari, Kiran Patel, Shravan Kumar, Pankaj Srivastava of IPR, for their friendly interaction and timely help.

I am very much indebted to my external doctoral committee members Prof. C Vijayan, IIT, Madras, Prof. Reji Philip, RRI, Bangalore, Dr. Ravi A V Kumar, Scientist-SG, IPR, Gandhinagar for reviewing my work regularly and for suggestions and motivation throughout my research period. I would also like to thank Dr. Rakesh Kumar, Dr. Bindu Krishnan and Dr. Deepak T. G., for thoughtful discussions.

I thank Prof. C. S. Narayanamurthy, Head, Department of Physics and Chairman, Doctoral Committee for his encouragement to improve my research. I am grateful to the teachers who taught me during my course work. I am extremely thankful to Director, IIST for his support and permitting me to carry out the experiments at IPR, Gandhinagar.

M Srinivasa Raju

ABSTRACT

Plasma is produced by focussing a laser beam on to a material and study of it has grown importance since last few decades due to its rich physics and substantial applications to space physics, inertial confinement fusion, laser plasma thruster, pulsed laser deposition, material characterization, etc. Magnetic field can be used to control the dynamics of plasma and plays important role in these applications.

In the present work, the effects of transverse magnetic field and argon ambient on the Nd:YAG laser produced barium and tungsten plasmas have been studied using optical emission spectroscopy and fast imaging. Barium and tungsten were used as the target materials due to their importance in space and tokamak applications, respectively. Experiments were performed at various magnetic fields of 0.3, 0.45, 0.52 Tesla and Ar pressures of 10^{-5}, 10^{-2}, 10^{-1}, 1, 3 Torr. Laser fluence is varied from 12 to 31 J/cm^2 in these experiments. The time-of-flight spectroscopy gives the detailed information about the velocity distribution of a particular species while the fast imaging gives the structural information of the plasma plume.

In the time of flight studies, the temporal profiles of two neutral lines and two ionic lines of barium are recorded at various distances 2 mm, 4 mm, up to 12 mm in vacuum (10^{-5} Torr). The temporal profiles of neutral lines are broadened in presence of magnetic field due to increased collisions where as the temporal profiles of ionic lines are narrowed down which showed that all emitting ionic species are confined in a small volume. Since the particle distribution in laser produced plasma can be described by a one-dimensional Shifted Maxwell-Boltzmann distribution function and therefore, a multiple component Shifted Maxwell-Boltzmann distribution was adopted to resolve the individual components. The neutral profiles showed two components in the absence of magnetic field where as an additional component appears in presence of magnetic field. The ionic profiles could be fitted with two Shifted Maxwell-Boltzmann components. Possible mechanisms of various SMB components are explained on the basis of collisions among plume species and correlated to electron temperature, electron density, etc. The ionic profiles showed efficient confinement in the presence of the magnetic field at higher fluences (This part of the work is published in Journal of Applied Physics, 2014).

Time of flight studies of barium plasma were performed at different ambient argon pressures of 10^{-5},10^{-2}, 10^{-1}, 1 and 3 Torr. The time-of-flight profiles of ions showed ambient pressure independent behaviour at 6 mm distance from the target which is attributed to diamagnetic behavior of laser plasma. A theoretical model is proposed to explain the compression of temporal profiles of the ionic lines. The neutral lines showed a fast peak which is attributed to recombination of singly ionized atoms (This part of the work is published in Optics Letters, 2015).

Effect of uniform magnetic fields of different strengths on tungsten and barium plasmas has been investigated using fast-imaging. Field aligned striations are observed in barium and tungsten plasmas in the presence of magnetic field at very low pressure of 10^{-5} Torr. These striations are investigated at different magnetic fields of 0.3, 0.45 and

0.52 Tesla. Different instabilities were discussed and electron-ion hybrid instability induced by the shear in the electron speed is identified as the potential mechanism for the observed striations. The plume front of the tungsten plasma showed a sharpening feature at 10^{-1} Torr pressure which is attributed to Laser Supported Detonation wave. At higher pressures of 1 Torr and 3 Torr, plasma showed turbulence attributed to R-T instability (This part of the work is communicated to Physics of Plasmas).

In conclusion, this thesis presents the dynamics and formation of structures in the expanding barium and tungsten plasmas in presence of magnetic field and argon ambient gas.

TABLE OF CONTENTS

LIST OF FIGURES

LIST OF TABLES

ABBREVIATIONS

CCD	Charge Couped Device
ICCD	Intensified Charge Couped Device
ITER	International Thermonuclear Experimental Reactor
J	Joule
K-H	Kelvin-Helmholtz
LLR K-H	Large Larmor Radius Kelvin-Helmholtz
LLR R-T	Large Larmor Radius Rayleigh-Taylor
LSD	Laser Supported Detonation
LTE	Local Thermodynamic Equilibrium
m	meter
μg	microgram
μs	microsecond
μm	micrometer
nm	nanometer
ns	nano second
OES	Optical Emission Spectroscopy
R-T	Rayleigh-Taylor
s	second
SMB	Shifted Maxwell-Boltzmann
T	Tesla
T-S	Taylor-Seldov
UV	Ultraviolet
W	Watt

NOTATION

A	Transition probability of a spectral line, s^{-1}
a	Acceleration of the plume front, s^{-2}
α_Z	Radiative recombination rate, $\text{cm}^3\,\text{s}^{-1}$
$\boldsymbol{B}$	Magnetic field, T
β	Deceleration coefficient, s^{-1}
c	Velocity of light in vacuum, $\text{m}\,\text{s}^{-1}$
ΔE	Energy difference, eV
$\boldsymbol{E}$	Electric field, $\text{V}\,\text{m}^{-1}$
E	Energy level of a spectroscopic state, eV
E_0	Incident laser energy, J
$\boldsymbol{E_{pol}}$	Polarization electric field, $\text{V}\,\text{m}^{-1}$
E_{av}	Average kinetic energy, J
e	Charge of an electron, C
ϵ_0	Permittivity of free space, $\text{F}\,\text{m}^{-1}$
f	Probability density function, $\text{m}^{-2}\,\text{s}^{-1}$
f_{ij}	Transition oscillator strength
g	Statistical weight factor of the upper state of a spectral state
γ	Ratio of specific heat
I	Intensity of a spectral line, cd
I_a	Intensity of the laser beam, W/cm^2
I_m	Image in the form of matrix
$\boldsymbol{J}$	Current density, Am^{-2}
K	Boltzmann's constant, JK^{-1}
χ	Absorption coefficient of radiation, m^{-1}
L	Dimension of plasma, m
L_0	Initial length of plasma stream, m

$L_s(\lambda)$	Line shape function, mm
l	Length of the plasma emitting region, mm
$\ln \Lambda$	Coulomb logarithm
λ	Wavelength, nm
λ_D	Debye length, m
λ_{RT}	Growth time of R-T instability, s
$\Delta\lambda_{1/2}$	Full width half maximum of a Stark profile fitted with Lorentzian , nm
m	Mass of a particle, kg
m_e	Mass of an electron, kg
m_0	Mass of ablated material, μ gr
$\dot{m}$	Rate of ablated mass, kg s^{-1} cm^{-2}
N	Number density of emitting species
N_c	Number turns in a coil
N_D	Number of particles in Debye sphere
n_c	Critical density of plasma, cm^{-3}
n_e	Electron density, cm^{-3}
n_i	Ion density, cm^{-3}
P_g	Pressure of background gas, Torr
p	Unitary matrix
ϕ	Electric potential, V
ρ_g	Background gas density, cm^{-3}
ρ_p	Plasma density, cm^{-3}
q	Diagonal matrix
R	Distance travelled by plasma plume, mm
R_b	Bubble radius, mm
R_0	Stopping distance of plasma plume, mm
r	Unitary matrix
σ	Electrical conductivity, S m^{-1}
t	Time, s
t_d	Magnetic diffusion time, s
T	Temperature, eV
T_e	Electron temperature, eV

T_i	Ion temperature, eV
τ	Growth time, s
τ_d	Optical depth
τ_c	Mean free time of collisions, s
u	Velocity of a particle, m s^{-1}
$u_\perp$	Velocity of a charged particle perpendicular to magnetic field, m s^{-1}
V	Flow velocity of plasma fluid, m s^{-1}
V_p	Volume of the plasma, cm^3
v	Velocity of plasma plume, m s^{-1}
v_0	Initial velocity of plasma slab, m s^{-1}
W_0	Initial width of the plasma stream, m
w	Electron impact parameter
w_s	Laser spot size, mm
Ω_e	Electron cyclotron frequency, Hz
ω	Frequency of waves or oscillations, Hz
ω_{LH}	Lower hybrid frequency, Hz
ω_p	Plasma frequency, Hz
ω_{pe}	Electron plasma frequency, Hz
ω_{pi}	Ion plasma frequency, Hz
Z	Atomic number
Z_p	Partition function
z	Distance form the target, mm

Subscripts

e	Electron
i	Ion
LH	Lower Hybrid
eff	Effective
g	Gas
b	Bubble
R-T	Rayleigh-Taylor
K-W	Kelvin-Helmholtz
EIH	Electron-Ion Hybrid

NOMENCLATURE

Nd:YAG	Neodymium-doped Yttrium Aluminium Garnet
Ba	Barium
W	Tungsten
NdFeB	Alloy of Neodymium, Iron and Boron
Ar	Ar

CHAPTER 1

INTRODUCTION

In this chapter, a brief introduction to plasma, laser ablation mechanism and important parameters of laser produced plasma are given. Dynamics of plasma expansion in vacuum, ambient gas, and magnetic field are discussed. Various diagnostics and applications of laser produced plasma are briefly discussed. Finally, the motivation and objective of the study are presented.

1.1 Plasma

A plasma is a quasineutral gas of charged and neutral particles which exhibits collective behaviour (Chen, 1984). The motion of any charged particle in a plasma produce electric and magnetic fields and interacts simultaneously with considerable number of other charged particles even in remote region by means of long range electromagnetic forces. This is called as *collective behaviour*.

1.1.1 Temperature and Density of Plasma

The temperature of a plasma is defined by thermodynamics. Assuming a gas in thermal equilibrium, the distribution of velocity of particles follows Maxwellian

$$f(u)\ du = A\ exp(-\frac{1}{2}mu^2/KT)\ du \qquad (1.1)$$

Here $f(u)du$ is the number of particles per m^3 with velocity between u and $u + du$, and K is Boltzmann's constant and $\frac{1}{2}mu^2$ is the kinetic energy of the particle, A is a constant. Here 'T' is the temperature, which gives the width of the Maxwellian distribution. If a gas is having three degrees of freedom, we can prove that the average kinetic energy is (Chen, 1984)

$$E_{av} = \frac{3}{2}KT \qquad (1.2)$$

The plasma may contain different temperatures for electrons (T_e) and ions (T_i).

The density of particles is defined as the number of particles in a unit volume having all possible velocities and can be written as

$$n = \int_{-\infty}^{\infty} f(u) \, du \tag{1.3}$$

A plasma has two densities, electron density (n_e) and ion density (n_i).

1.2 Criteria for Plasma

An ionized gas has to satisfy the following criteria to be called as a plasma.

1.2.1 Debye Length

The charged particles in a plasma try to shield any electrostatic field by arranging themselves. The Debye length (λ_D) is a measure of distance over which the influence of a non-zero potential is experienced by the charged particles in a plasma. A positive potential at certain place (x=0) inside a plasma is shielded by the accumulation of negative charges and it decreases with distance as (Chen, 1984)

$$\phi = \phi_0 \, e^{-|x|/\lambda_D} \tag{1.4}$$

where

$$\lambda_D = \left(\frac{\epsilon_0 K T_e}{n_e e^2} \right)^{1/2} \tag{1.5}$$

here n_e is the electron density and T_e is the electron temperature. The imaginary sphere inside a plasma of radius λ_D is called as Debye sphere. The concept of Debye shielding is statistically valid only when the Debye sphere contains a large number of particles. The number of particles in a Debye sphere is given by

$$N_D = n_e \, \frac{4}{3} \pi \lambda_D^3 \gg 1 \tag{1.6}$$

This is one of the criteria for a ionized gas to be called as a plasma.

1.2.2 Quasineutrality of a Plasma

If the dimension of a system of charged particles L is much larger than λ_D, then any local concentrations of charge or external potential are shielded out in a distance short compared to L. Then, the bulk of the plasma is neutral enough so that electron and ion densities can be taken as equal, but not so neutral that all the electromagnetic forces vanish. This is called as quasineutrality and can be expressed as

$$L \gg \lambda_D \tag{1.7}$$

or

$$n_i \simeq n_e \simeq n \tag{1.8}$$

1.2.3 Plasma Frequency

In a weakly ionized gas the charged particles collide so frequently with neutral atoms and the motion is controlled by ordinary hydrodynamics. Unlike an ordinary gas, plasma has certain oscillations because of electromagnetic forces. The frequency of a typical plasma oscillation should be greater than the collision frequency among the neutral atoms so that the gas behave like a plasma rather than an ordinary gas. If ω_p is the frequency of plasma oscillations and τ_c is the mean free time between the collisions with the neutral atoms, plasma requires

$$\omega_\mathrm{p}\,\tau_c > 1 \tag{1.9}$$

Equations 1.6, 1.7, 1.9 are the criteria for the plasma.

1.3 Production of plasma in laboratory

There are several ways to produce plasma in laboratory. Commonly used processes like electric discharge, photoionization, laser-induced breakdown, particle beams, etc., are discussed below.

Electric Discharge

In this process, an electric field is applied across an ionized gas that accelerates free electrons. These electrons collide with other atoms and ionize to form a plasma. Since the electric field can transfer energy to electrons more efficiently relative to ions, the electron temperature is higher than ion temperature in gas discharge plasmas.

Photo-ionization

Process of ionization of an atom by absorption of photons of energy equal or greater than its ionization potential is called as photoionization. The earth's ionosphere is an example for this kind of plasmas in nature. In laboratory, we can produce this type of plasma by laser heating of a low density gas (Wang et al., 2008). In this process, a low electron density is required so that collisional ionization is dominated by photoionization.

Laser produced plasma

When a laser pulse of extremely high intensity falls on the target material, the surface layer is immediately ionized and transformed into hot expanding plasma (Rubenchik and Witkowski, 1991). This type of plasma can be produced by lasers of different pulse widths nano-second, pico-second, femto-second, etc. The ablation mechanism, electron density, electron temperature, and dynamics of the plasma depends on different parameters such as pulse width, wavelength, intensity of the laser, etc.

Apart from the above methods, there are several other methods to produce plasma such as by heating of a gas using Heavy Ion Beams (HIB) and Relativistic Electron Beams (REB) (Griegel et al., 1990; Bret et al., 2005), etc.

1.4　Ablation Mechanism of Laser Produced Plasma

There are two steps in the formation of laser produced plasma from a gas. In the first step, a high power laser pulse incident on the target ionize the gas in the focal volume due to the interaction of electric field associated with the light wave and produce charged particles. In the second step, the ionization grows due to processes such as multiphoton ionization, multiphoton excitation, etc. In multiphoton ionization, an atom simultaneously absorb several photons to dissociate into electron and positive ion. When the laser irradiance is greater than a threshold, breakdown occurs and the gas becomes opaque (Singh and Thakur, 2007).

The typical values of threshold of laser irradiation for breakdown of a solid target are lower compared to a gas. The laser pulse falling on a solid target causes melting and vaporization of the target surface. The laser pulse interacts with the vapour, heating and ionizing it, making it opaque to the trailing edge of the pulse. When the laser pulse ends, the plasma becomes hot so that thermal radiation emitted from the plasma can cause more ionization of the target surface. If the pulse width of the laser is very less such as pico second or femto second, then there is no reheating of the plasma by the laser pulse. Under similar fluence conditions, mass ablated by the femto second lasers is more compared to that of the nano second lasers.

The suggestion by Dawson that giant pulse lasers can be used to produce plasmas (Dawson, 1964) triggered research activities on laser produced plasma. Effects of different experimental parameters such as target purity (Ehler et al., 1980), focal spot size (Tao et al., 2006), wavelength of the laser (Abdellatif and Imam, 2002), fluence (Kumar et al., 2006) etc., on laser produced plasma were reported. Plasmas produced by using different types of lasers with different pulse widths such as excimer laser (248 nm) with 15 ns pulse width (Rothenberg and Koren, 1984), Phosphate Neodynium glass laser (1.06 μm) with 3 ns pulse width (Goldstein et al., 1987), neodymium-glass laser (0.53 μm) with pulse width 2 ns, Nd:YAG laser (1.064 μm) with 5 ns pulse width (Orthaber et al., 2014) were studied. Self generated magnetic fields and their scaling laws in laser produced plasmas were

also reported. Study of laser produced plasma with two pulses have been used to enhance the emission intensity from the plasma (Uebbing et al., 1991; Babushok et al., 2006).

1.5 Plasma Parameters of Laser Produced Plasma

Some of the important plasma parameters that are used throughout the thesis are given below:

1.5.1 Electron temperature

Electron temperature can be determined from the spectroscopic measurements of relative line intensities of the emissions from same or neighbouring ionizations states of different atoms (Griem, 2005). It can also be measured by using the Langmuir probe (Kumari et al., 2012; Lunney et al., 2007). Electron temperature can be estimated from the ratio of intensities of the two spectral lines which belong to the same ionized state using the relation (Griem, 2012)

$$\frac{I_1}{I_2} = \frac{g_1}{g_2}\frac{A_1}{A_2}\frac{\lambda_2}{\lambda_1}\, e^{-\frac{(E_1 - E_2)}{K T_e}} \tag{1.10}$$

Here I_1, I_2 are the intensities of the spectral lines of wavelengths λ_1 and λ_2; g_1, g_2 are the statistical weight factors, A_1, A_2 are the transition probabilities, E_1, E_2 are the energies of the excited states of the two spectral lines, K is the Boltzmann's constant and T_e is the electron temperature.

1.5.2 Electron density

Electron density of a laser produced plasma can be determined by interferometry (Ovsyannikov and Zhukov, 2000; Patra et al., 2005), spectroscopy (Griem, 2012; Shaikh et al., 2006), Thomson scattering (Hutchinson, 2005; Diwakar and Hahn, 2008), etc. One of the commonly used method for determining electron density is by using Stark broadening. In this method, the electron density n_e is deduced

by the relation (Griem, 2012)

$$\Delta\lambda_{1/2} = \frac{2wn_e}{10^{16}} \tag{1.11}$$

where $\Delta\lambda_{1/2}$ is the FWHM of Stark profile fitted with Lorentzian and w is the electron impact parameter of the stark broadened line. The electron density of a laser produced plasma depends on the incident laser wavelength, fluence, power, as well as material of the target.

1.5.3 Optical Depth

The process of absorption of radiation by the atoms of the same kind by which the radiation was emitted is called self-absorption. This weakens the real intensities of the spectral lines. The equation for radiative transfer can be written as (Cooper, 1966)

$$\frac{1}{\chi_a(\nu,x)} \frac{dI(\nu,x)}{dx} = -I(\nu,x) + \frac{J_e(\nu,x)}{\chi(\nu,x)} \tag{1.12}$$

Here $I(\nu,x)$ is the intensity of radiation at a frequency ν at a point of distance x in the direction of line of sight, $\chi_a(\nu,x)$ is the absorption coefficient, $J_e(\nu,x)$ represents emission coefficient. The optical depth (τ_d) is defined as

$$d\tau_d(\nu) = -\chi_a(\nu,x)\, dx \tag{1.13}$$

Then the intensity of spectral line emitted can be written as

$$I = I_P(\nu_0) \int_0^\infty \left(1 - e^{\tau_d(\nu)}\right) d\nu \tag{1.14}$$

For the plasma in LTE, the optical depth can be written as (Aragon et al., 2001)

$$\tau_d(\lambda) = \chi_a(\lambda)\, N\, l\, L_s(\lambda) \tag{1.15}$$

where

$$\chi_a(\lambda) = \frac{e^2\lambda_0^2}{4\epsilon_0 m_e c^2}\, f_{ij} \frac{g_i e^{-\frac{E_i}{KT_e}}}{Z_p(T_e)} \left(1 - e^{-\frac{E_i-E_j}{KT_e}}\right) \tag{1.16}$$

Here l is the length of the emitting region, c is the speed of light, ϵ_0 is the permittivity of free space, m_e is the mass of electron, λ_0 is the center wavelength of the emission line, f_{ij} is the transition oscillator strength, E_i and E_j are the energies of the lower and upper levels respectively, N is the number density of emitting species, T_e is the electron temperature, $Z_p(T_e)$ is the partition function which depends on the charge state, and $L_s(\lambda)$ is the line shape function.

If the optical depth has a very small value, the plasma is called as optically thin and the self-absorption effects can be neglected, or else, the plasma is called as optically thick and the correction of self-absorption for the intensity of spectral lines should be taken into account.

1.6 Oscillations and Waves in Plasma

There are two theories for prediction of plasma behaviour, namely, fluid theory and kinetic theory. In fluid theory, the identity of the individual particle in a fluid or plasma is neglected and only motion of the fluid elements is taken into account. Kinetic theory of plasma is more refined treatment of the plasma. In this theory, the velocity distribution function of each species of the plasma is considered to explain the behaviour of plasma. By assuming plasma as a fluid, different oscillations and waves are possible in a plasma and are discussed below.

1.6.1 Electron Plasma Oscillations

Even though plasma contains electrons and positive particles, the massive ions can be treated as a background. If the electrons are disturbed from their equilibrium position, electric fields will be built up to restore the neutrality of the plasma. The electrons will overshoot because of their inertia and oscillate around their equilibrium position with a characteristic frequency known as electron plasma frequency and is given by (Chen, 1984)

$$\omega_{pe} = \left(\frac{n_e e^2}{\epsilon_0 m_e}\right)^{1/2} \tag{1.17}$$

1.6.2 Electron Plasma Waves

The thermal motion of the electrons can cause plasma oscillations to propagate. Then the electron plasma oscillations can be called as electron plasma waves. The dispersion relation for the electron plasma wave can be written as

$$\omega^2 = \omega_p^2 + \frac{3}{2}k^2 v_{th}^2 \tag{1.18}$$

where ω is the frequency of the wave and k is the wave number of the wave and v_{th} is the thermal velocity given by $v_{th} = 2KT_e/m_e$.

1.6.3 Ion Acoustic Waves

In the above two cases, the ions are assumed to be a uniform positive background. Even though the mass of the ions is large compared to that of electrons, they can cause low frequency waves called as ion waves or ion acoustic waves. The dispersion relation can be written as

$$\frac{\omega}{k} = \left(\frac{KT_e + \gamma_i KT_i}{M} \right)^{1/2} = v_s \tag{1.19}$$

where ω is the frequency, k is the wave number, K is Boltzmann's constant, T_e is electron temperature, T_i is ion temperature and M is the mass of each ion, γ_i is the ratio of specific heats of ions. The mechanisms of the electron plasma oscillations and ion acoustic waves are different. In electron plasma waves, ions are assumed to be fixed and form a uniform background. But in ion acoustic waves, the ions are moving and the electrons are also pulled along with the ions. The electrons tend to shield out electric field arising from the ions. This shielding is not perfect because of the electron thermal motion and potentials of the order of KT_e/e can leak out. The ions form compressions and rarefactions in ion acoustic waves. The compressed regions try to expand into rarefactions due to two reasons. One of the reasons is due to the thermal motion of ions which is contributed by the term $\gamma_i KT_i/M$ in Equation 1.19. Secondly, the ion bunches are positively charged and

disperse because of the electric field. Since this field is largely shielded out by electrons, only a fraction proportional to KT_e is available to act on the ion bunches. This is accounted by the KT_e term in Equation 1.19. The ions overshoot because of inertia and compressions and rarefactions are generated. From Equation 1.19, we can see that the ion acoustic waves can be present in plasma even when the ion temperature is zero, which is not possible in ordinary gas.

1.6.4 Electromagnetic Waves in Plasma in the Absence of External Magneitc Field

When electromagnetic waves travel in plasma without any external magnetic field, the dispersion relation can be written as

$$\omega^2 = \omega_p^2 + c^2 k^2 \tag{1.20}$$

If we send a electromagnetic wave with a frequency ω, the wavelength of the wave $(2\pi/k)$ after entering into plasma can be determined by above equation. When the frequency of the wave is increased, wave number k decreases. At a particular frequency of microwave, k becomes zero. This frequency is called as cut-off frequency. Corresponding density of the plasma is called as critical density which can be written as

$$n_c = \frac{m\epsilon_0 \omega_{pe}^2}{c^2} \tag{1.21}$$

where ϵ_0 is the permittivity of free space and m_e is the mass of the electron. If the frequency of microwave is greater than the cut off frequency, the wave will attenuate exponentially.

1.6.5 Electromagnetic Waves in Plasma in Presence of External Magneitc Field

The behaviour of electromagnetic wave entering into a plasma when an external magnetic field is present depends on the relative orientation of electric and magnetic field vectors of the electro magnetic wave and the external magnetic field.

If the electric field of a transverse electromagnetic wave is parallel to magnetic field, there is no effect of magnetic field on the electron motion and the dispersion relation is identical to Equation 1.20. These waves are called as ordinary waves.

If the electric field vector of an incident electromagnetic wave is perpendicular to the external magnetic field, then such a wave develops an electric field component along the propagation direction in the plasma. These waves are partly longitudinal and partly transverse and called as extraordinary waves. The dispersion relation for such a waves can be deduced as

$$\frac{c^2 k^2}{\omega^2} = \frac{c^2}{v_\phi^2} = 1 - \frac{\omega_p^2}{\omega^2} \frac{\omega^2 - \omega_p^2}{\omega^2 - \omega_h^2} \tag{1.22}$$

where v_ϕ is the phase velocity, ω is the frequency, k is the wave number, c is the velocity of light in vacuum, and ω_h is the upper hybrid frequency which is given by

$$\omega_h^2 = \omega_{pe}^2 + \omega_{ce}^2 \tag{1.23}$$

Here ω_{ce} is the electron cyclotron frequency.

1.7 Dynamics of Laser Produced plasma in Vacuum and Ambient gas

1.7.1 Vacuum

In vacuum, the plasma expansion process can be described by using adiabatic expansion model and the Euler equations of hydrodynamics. The Euler's equations of motion are, the conservation of mass

$$\frac{\partial \rho}{\partial t} = -\frac{\partial(\rho v)}{\partial x} \tag{1.24}$$

the conservation of momentum,

$$\frac{\partial(\rho v)}{\partial t} = -\frac{\partial}{\partial x}\left[p + \rho v^2\right] \qquad (1.25)$$

and conservation of energy

$$\frac{\partial}{\partial t}\left[\rho\left(E_d + \frac{v^2}{2}\right)\right] = -\frac{\partial}{\partial x}\left[\rho v\left(E_d + \frac{p}{\rho} + \frac{v^2}{2}\right)\right] + \alpha_{IB}I \qquad (1.26)$$

Here v is the flow velocity, ρ represents mass density, p is the pressure and E_d is the energy density. The expansion velocity can be obtained by (Zeldovich et al., 2002)

$$v = \sqrt{\frac{4\gamma + 10}{3}\frac{E}{M}} \qquad (1.27)$$

where E is the energy of the plume, M is the mass evaporated and γ is the ratio of specific heats. Numerous experiments (Harilal et al., 2005a; Geohegan, 1992; Sharma and Thareja, 2005) were carried out on the laser produced plasma expanding in vacuum, reporting that the plasma follows linear expansion. This is because, at very low pressure, the mean free path of the gas molecules is very small so that there is no much interaction between the expanding plasma and the ambient gas.

1.7.2 Ambient gas

The presence of ambient gas causes deceleration and confinement of the plasma. There are two models to explain the dynamics of laser produced plasma in presence of an ambient gas, namely, shock model and drag model.

Shock Model

In the high background pressure regime, the plume expansion can be explained by shock model (Geohegan, 1992). This is valid when the ablated mass is small compared to mass of the background gas swept by the plasma and a shock is

formed in front of the plasma. The R-t plot follows (Zeldovich et al., 2002)

$$R = \zeta_0 \, (E_0/\rho_0)^{1/5} \, t^{2/5} \qquad (1.28)$$

where R is the distance of the plume at a time t, ζ_0 is a constant depending on the specific heat capacity of the gas, ρ_0 is the density of background gas and E_0 is the energy released to the background gas. If the temporal region prior to the formation of shock wave is ignored, the shock wave model describes the expansion of plasma increasingly well at higher background pressures (Geohegan, 1992).

Drag Model

This is valid at low background pressures at the initial stages of the plasma (Geohegan, 1992). According to this model, the plasma plume experiences a viscous force proportional to its velocity through the background gas. The R-t plot follows

$$R = R_0 \, (1 - exp(-\beta t)) \qquad (1.29)$$

where R is the distance of the plume at a time t, R_0 is the stopping distance of the plume and β is the deceleration coefficient given by

$$R_0\beta = v_0 \qquad (1.30)$$

Here v_0 is the initial velocity of the ejected species.

1.8 Laser produced plasma in presence of external magnetic field

Expansion of laser produced plasma in presence of external magnetic field can be expalined by using two models, one is the self-polarization of plasma, and the other is diamagnetic cavity model .

1.8.1 Self-Polarization of Plasma

The generalized ohms law in Magnetohydrodynamics can be written as (Bittencourt, 2013)

$$\boldsymbol{E} + \boldsymbol{V} \times \boldsymbol{B} = \frac{\boldsymbol{J}}{\sigma} + \frac{\boldsymbol{J} \times \boldsymbol{B}}{n_e e} \tag{1.31}$$

where $\boldsymbol{E}$ represents electric field, $\boldsymbol{B}$ is the magnetic field, $\boldsymbol{V}$ is the flow velocity of the plasma fluid, $\boldsymbol{J}$ is the current density, σ is the electrical conductivity, and n_e is the electron density . As the plasma expands in a transverse magnetic field, the negative electrons and positive ions are deflected in opposite directions because of the Lorentz force. Consequently, charge layers are formed on either side of the plasma stream. The polarization electric field arise due to the separation of charge layers which balance the Lorentz force so that the remaining charge particles inside the plasma are not affected (Borovsky, 1987). By equating these two forces, we can deduce the velocity of the plasma stream

$$\boldsymbol{v_0} = \frac{(\boldsymbol{E_{pol}} \times \boldsymbol{B_0})}{B_0^2} \tag{1.32}$$

where $\boldsymbol{v_0}$ is the original plume velocity, $\boldsymbol{B_0}$ is the external magnetic field and $\boldsymbol{E_{pol}}$ is the polarization electric field. The plasma gets polarized until the $\boldsymbol{E} \times \boldsymbol{B}$ drift velocity equals to its original velocity. The magnitude of the polarization electric field is maximum inside the bulk plasma while it is less in the charge layers at the boundary so that the $\boldsymbol{E} \times \boldsymbol{B}$ drift velocity of charge layers at boundary is less than that of the bulk plasma inside. As the plasma propagates in field, the charge layers fall behind of the bulk plasma and the plasma need to supply fresh charge layers from inside. This leads to the erosion of the plasma stream. Thus the propagation distance of the plasma decreases in presence of magnetic field. Assuming a plasma of slab shape and having no divergence, the distance of propagation can be written as (Borovsky, 1987)

$$R_{stripping} \leq L \frac{\omega_{pe}^2}{\omega_{ce}} \frac{2W}{v_0} \tag{1.33}$$

where L is the initial length, W is the initial width of the plasma stream, v_0 is the initial stream velocity, ω_{pe} is the electron plasma frequency and ω_{ce} is the cyclotron

frequency of electrons. By assuming one-dimensional flow with no conduction currents, we can write the Lorentz force equation as $E_y = v_x B_z$ where the plasma is expanding in x-direction, magnetic field is in z-direction while the polarization electric field is in y-direction. By taking into account that the expansion of the plasma plume is three-dimensional, the polarization electric field transverse to the flow varies over plume cross-section, since v_x decreases at larger angles with respect to perpendicular to the target surface. The field gradient at the boundary causes the formation of closed current paths. Inside the plasma plume, the current interacts with the plasma plume and gives $\mathbf{J} \times \mathbf{B}$ force, and decelerates the plasma. In the outer regions of the plume, the plume experiences acceleration because of - $\mathbf{J} \times \mathbf{B}$ force since the return current is opposite to the current inside the plasma (Neogi and Thareja, 1999). These two forces gives rise to the splitting of the laser produced plasma in presence of external magnetic field.

1.8.2 Diamagnetic Cavity Model

In a laser produced plasma, generally, the Larmor radius of ions is greater than or comparable to the scale length of the plasma while that of electrons is very less. So practically the electrons can have number of gyrations around field lines while the ions cannot have. The ions can be treated as unmagnetized whereas electrons are magnetized (Ganguli et al., 1988). Even though the ions can move across the magnetic field, the electrons which are captured by the magnetic field hold them back. This generates an electric field pointing radially inward (VanZeeland and Gekelman, 2004) and the $\mathbf{E} \times \mathbf{B}$ drift of electrons, gives rise to a diamagnetic current. Since the induced magnetic field due to the electron drift opposes the applied magnetic field, the plasma behaves as a diamagnetic cavity, which is also called as magnetic bubble. In this process, the plasma kinetic energy is converted into the magnetic potential energy. The relation between the radius of the diamagnetic cavity and velocity of ions can be derived from the energy balance equation (Collette

and Gekelman, 2011)

$$\frac{1}{2}Mv_\perp^2(t) + \frac{2\pi\boldsymbol{B_0}^2}{3\mu_0}R^3(t) = U_0 \qquad (1.34)$$

Where M is the mass of the plasma, $v_\perp$ is the velocity of the ions in the direction perpendicular to the external magnetic field $\boldsymbol{B_0}$, μ_0 is the permeability of free space, R is the cavity radius and U_0 is the initial energy. It has been reported in experiments using magnetic probes that the self-generated magnetic field increases with time and reaches a peak value and then decreases after the magnetic bubble cross the probe (Kacenjar et al., 1986).

1.9   Plasma Parameters in Magnetic Field

1.9.1   Larmor Radius

The Larmor radius or gyroradius of a charged particle is defined as the radius of the circular motion of a charged particle in presence of a magnetic field. The equation for Larmor radius is

$$r = \frac{mu_\perp}{qB} \qquad (1.35)$$

where B is the magnetic field, q is the charge, m is the mass, and $u_\perp$ is the velocity of the particle perpendicular to the magnetic field of the particle. The dynamics of plasma in presence of a magnetic field depends on Larmor radius and the scale length of the plasma. When the Larmor radius of the plasma is comparable or greater than the density scale length of the plasma, the particle can not make much gyrations and travels almost in a straight line path. Such a charged particle can be treated as unmagnetized. In general, in laser produced plasma, the electrons are magnetized while the ions are unmagnetized.

1.9.2 Plasma beta

Thermal beta

The thermal beta of a plasma is defined as the ratio of plasma thermal pressure to the magnetic pressure. It can be calculated by using

$$\beta_t = \frac{8\pi n_e K T_e}{B^2} \tag{1.36}$$

Directed beta

After the initial conversion of plasma thermal energy into directed energy, it is appropriate to define directed beta instead of thermal beta (Harilal et al., 2005b). Directed beta is defined as the ratio of plasma kinetic pressure to the magnetic pressure and can be estimated by using

$$\beta_d = \frac{4\pi n_e m v^2}{B^2} \tag{1.37}$$

Bubble Radius

According to the diamagnetic cavity model, expanding laser produced plasma behaves as a magnetic bubble. As the plasma expands, the plasma kinetic energy is converted into magnetic potential energy. Thus for an expanding plasma, the value of β decreases with distance and becomes unity where the plasma cannot expand. This distance is called as bubble radius or confinement radius. The bubble radius R_b can be estimated by (VanZeeland et al., 2003)

$$R_b = \left(\frac{3\mu_0 E_{lpp}}{\pi B^2}\right)^{1/3} \tag{1.38}$$

Here E_{lpp} is the kinetic energy of the laser plasma which is approximated as half of the initial laser beam energy and B is the applied magnetic field. At the bubble radius R_b, where the total excluded magnetic energy becomes equal to the kinetic

energy of the plasma, the diamagnetic current is maximum (VanZeeland and Gekelman, 2004).

Classical Magnetic Diffusion Time

When the magnetic bubble reaches the confinement radius, the field diffuses back into the bubble rapidly at first and then slows down to a time which is called classical magnetic diffusion time. The magnetic diffusion time is defined by (VanZeeland and Gekelman, 2004) as

$$t_b = \frac{4\pi\sigma R_b^2}{c^2} \qquad (1.39)$$

where σ is the plasma conductivity which can be obtained using the relation (Chen, 1984)

$$\sigma = \frac{50\pi^{1/2}\epsilon_0^2 (KT_e)^{3/2}}{m_e^{1/2} e^2 z \ln \Lambda} \qquad (1.40)$$

where T_e is the electron temperature, $\ln \Lambda$ is the coulomb logarithm, which can be estimated by (Spitzer, 2013)

$$\ln \Lambda = ln\left[\frac{3}{2}\sqrt{\frac{(KT_e)^3}{\pi n_e}}\frac{1}{Ze^3}\right] \qquad (1.41)$$

1.10 Atomic Processes in Plasma

Various atomic processes such as ionization and recombination processes are possible in a laser produced plasma. The atomic process that dominates in a particular plasma depends on the electron temperature, density, dimensions of the plasma, laser wavelength, pulse duration, laser energy, etc. (Pagano et al., 2009; Farid et al., 2013). Various atomic processes in a plasma are discussed below.

1.10.1 Ionization

Autoionization

In autoionization, an excited atom spontaneously loses an electron without any interaction with external energy source (McNaught and McNaught, 1997). This process takes place when two or more valence electrons are excited and one of them is spontaneously ejected from the atom (Riviere et al., 2012). This can also occur when one inner shell electron is missing in which case an electron form an upper shell occupies the hole and another electron is ejected, which is known as Auger effect.

Collisional Ionization

In this process, the electrons or other plasma constituents collide either among themselves or with the ambient gas so that ionization takes place. If the collisional ionization is due to an electron, it is called as electron impact ionization. In the laser produced plasma, it was reported that, the plasma constituents can cause ionization of the ambient gas by means of collisional ionization (Neogi and Thareja, 1999). When a plasma is expanding in a magnetic field, the confinement of electrons causes the collisional ionization of neutrals (Kokai et al., 1996).

Photoionization

Photoionization is a process in which a photon is absorbed by an atom and an electron is ejected by electromagnetic field (Rybicki and Lightman, 2008). In laser plasma, photoionization of neutrals may occur due to the Ultraviolet (UV) and X-rays emitted by the plasma (Pant et al., 1998). Multiphoton ionization is a photoionization process where an atom absorbs more than one photon within its excitation lifetime and gets ionized (Kroll and Watson, 1972). This process dominates in the plasma generation when the pulse width of the laser is in pico-second and nano-second regime (Oraevsky et al., 1996).

1.10.2 Recombination

Radiative Recombination

This is a two body recombination process. Here a continuum electron is captured by an ion via a spontaneous emission of a photon (Hussain et al., 2006). The rate of recombination rate is given by

$$\left|\frac{\partial n_e}{\partial t}\right|_\alpha = n_e n_i \alpha_Z \tag{1.42}$$

where n_e is electron density and n_i is ion density, and α_Z is radiative recombination rate, which can be estimated by (Gupta and Sinha, 1997)

$$\alpha_z = \frac{8.5 \times 10^{-14} Z \; \beta^{3/2}}{\beta + 0.6} cm^3 s^{-1} \tag{1.43}$$

where $\beta = Z^2 \chi_H / T_e$. Here χ_H is ionization potential of hydrogen and Z is the charge state of the ion. The radiative recombination has a dependence of $T_e^{-1/2}$.

Three-body recombination

This is one of the processes which produce hot electrons in laser produced plasma (Bulgakova et al., 2000). This process starts with the capture of an electron by an ion and forms an atom in an excited state. This excited atom loses its energy by electron impact and comes to lower excited state by transferring energy to another electron. Further, the atom comes to ground state by radiative transfer (Fridman and Kennedy, 2004). The rate constant of three-body recombination can be estimated from the temporal variation of electron density (Camacho et al., 2010). The radiative recombination has a dependence of $T_e^{-1/2}$ while three-body recombination follows $T_e^{-9/2}$ dependence (Zeldovich et al., 2002). So, the cold electrons are likely to collide with ions as a second particle while the hot electrons act as third particle in three-body recombination.

Di-electronic Recombination

Di-electronic recombination is a two step process. Firstly, a free electron excites an electron in an ion X^{+z} and transfers sufficient of its energy so that it is captured into an autoionizing state of the ion X^{+z-1}. This step is a reversible process. In the second step, either the captured electron or an electron in the parent core makes a spontaneous radiative transition and leaves the ion in non-autoionizing state (N. R. Badnell et al., 2003). The recombination is complete through the second step. This is very important in coronal or less dense plasmas (Timmer et al., 1991).

Charge Exchange Recombination

This is a combined process of recombination as well as ionization. Here an ion interacts with a neutral atom captures one or more electrons from the atom so that the ion recombines with that electron while the atom becomes ionized (Beiersdorfer et al., 2000). Expanding plasma can interact with an ambient gas via charge exchange recombination (Harilal et al., 2003). The charge exchange interaction also plays a very important role in the x-ray laser using a plasma column (Suckewer and Fishman, 1980).

1.11 Plasma Diagnostics

The relevant plasma diagnostics like optical emission spectroscopy, fast imaging, interferometry, scattering, Langmuir probe and magnetic diagnostics are discussed below.

1.11.1 Optical Emission Spectroscopy

Neutral atoms, ions and electrons in the laser produced plasma emit radiation which is characteristic of the target material. The analysis of the emission from the plasma can be used to determine the dynamics as well as plasma parameters (Griem, 2012).

Spectral Line Profiles

There are different diagnostics for plasma based on the spectral line intensity and line shape. As discussed in Section 1.5.1, the electron temperature can be determined from relative intensities of spectral lines. Spectral lines emitted by plasma are also broadened and shifted compared to their natural line width and vacuum wavelengths (Griem, 2012). Commonly observed broadenings are Stark broadening and Doppler broadening. The Stark broadening can be used to find the electron density of the plasma as explained in Section 1.5.2.

Time of Flight Spectroscopy

In this technique, emission intensity of particular spectral line from laser produced plasma is monitored with time at a particular distance from the target surface. Here the emission from the plasma is taken to the entrance slit of the monochromator. The wavelength of the spectral line to be monitored can be set in the monochromator. The monochromator is coupled to a Photomultiplier Tube (PMT) where the optical signal is converted into electric signal. The electric signal from PMT is stored in a digital phosphor oscilloscope. The recorded profile is called as temporal profile or time-of-flight profile. By recording these profiles at different distances from the target surface, dynamics of different neutral and ionic species in ground and excited states in the plasma can be understood. By fitting the temporal profiles with Shifted Maxwell-Boltzmann Distribution (SMB), we can find different components of a particular species.

1.11.2   Fast Imaging

Fast imaging is recording of two-dimensional snap shots of emission from an expanding plasma plume using a gated Intensified Charge Coupled Device (ICCD) with very short gate widths in nano-second and pico-second regime. Using this technique, propagation distance, velocity and acceleration of the plasma can be estimated. Plume splitting and instabilities in the plasma can also be observed from the recorded images. By using filters which can transmit only a particular wave-

length, this technique can also be used to study the dynamics of a particular species in plasma.

1.11.3 Interferometry

The classic two beam interferometry can be used for interference examination of plasma using lasers (Ovsyannikov and Zhukov, 2000). Time resolution is large for this experiments with the possibility of using ultra-short laser pulses. There are different methods in interferometry of the plasma such as non-linear interferometry, resonance interferometry, laser interferometry, etc.

In case of non-linear interferometry (Ovsyannikov and Zhukov, 2000), plasma probing is carried out by simultaneous radiation of the fundamental and second harmonic of a high power laser and two interferograms corresponding to two wavelengths are recorded. In this method, it is possible to separate the contributions to the refraction of the plasma of electrons and ions. This method can be used to determine the electron density. Resonance interferometry method uses the radiation close to one of the resonance lines in the plasma. This method is useful to study a particular species in the plasma. Tunable dye lasers are useful in resonance interferometry with different species in the plasma. Using this method, the concentration of the absorbing atoms can be estimated from the fringe shift. In laser interferometry method, laser is used as a light source as well as interferometer. Here the plasma to be probed is introduced in an additional cavity which is linked with the main laser so that the intensity of the laser radiation depends on the phase shift introduced by the plasma. The changes in the parameters of the laser causes change in the optical length of the cavity which in turn causes the modulation of the laser intensity. Phase shifts are recorded by photoelectric methods.

1.11.4 Scattering of Electromagnetic Radiation from Plasma

When an electromagnetic wave impinges on the plasma particle, the particle gets accelerated and emits electromagnetic radiation in all directions. The

classical limit of scattering of electromagnetic radiation with free charges is called as Thomson scattering (Hutchinson, 2005). This diagnostic can be used to find the distribution function of electrons as well as ions. There are two types of Thomson Scattering, namely, Incoherent and Coherent. Incoherent Thomson scattering ignores the particle correlations and total scattered power can be obtained as an incoherent sum of scattered powers from single electrons. But the fraction of incoherently scattered photons is very less leading to problems in its detection. So experiments are performed with energetic pulsed lasers. In addition to this, there are other practical difficulties such as removing stray light, electrical noise and thermal background radiation.

1.11.5   Langmuir Probe

Langmuir probe is a cylindrical wire, generally made from tungsten, inserted into the plasma to collect the current from the plasma species at various applied voltages (Auciello and Flamm, 2013). It is possible to determine electron temperature, electron density, plasma potential, electron and ion beam energy using Langmuir probe. The advantages of this diagnostic is its simplicity and it works over a wide range of plasma densities and plasma temperatures. The main drawback of Langmuir probe is, since the probe perturbs its local surroundings, it is necessary to calibrate probe with some other diagnostic technique. The conventional langmuir probe theory is not applicable for high pressure plasmas because the mean free path of electrons becomes shorter compared to probe dimension.

1.11.6   Magnetic Diagnostics

Electric and magnetic fields and currents inside and outside the plasma are important parameters for magnetized as well as unmagnetized plasmas. Following are some of the methods to measure the magnetic field.
Magnetic Coil: This method can only be used to measure a time-varying magnetic field. The voltage induced in a coil due to a variation of a magnetic field is a function of the rate of change of the magnetic field. By using an analog integrated circuit,

one can obtain the voltage which is proportional to magnetic field, by using the relation (Hutchinson, 2005)

$$V_0 = \frac{N \, A \, B}{RC}$$ (1.44)

here V_0 is the voltage induced in the coil, A is the area of the coil, N_c is the number of turns in the coil, and RC is the time constant.

Hall Probe: When a current flows through a semi-conductor placed in a magnetic field, the electrons and holes experience Lorentz force and deviate in a direction perpendicular to current density **J** and magnetic field **B**. The electric field produced in this process cancels the magnetic force on the charge carriers. The drawbacks of Hall probes are as follows. They are sensitive to electrical noise and become non-linear at high magnetic fields.

1.12   Instabilities in Plasma

In the relaxation process into an equilibrium state, a plasma may develop an instability. Commonly observed instabilities in laser produced plasma are

1. Classical Rayleigh-Taylor Instability

2. Large Larmor Radius Rayleigh-Taylor Instability

3. Kelvin-Helmholtz Instability

4. Large Larmor Radius Kelvin-Helmholtz Instability

An instability produced in a plasma can be characterized by different parameters such as morphology of the instability, growth time and other conditions for existence of such instability. Each of the above instabilities is discussed in detail in the following section.

1.12.1   Classical Rayleigh-Taylor Instability

When the density gradient and acceleration of a hydrodynamic system are opposite to each other, such a system can be R-T unstable (Taylor, 1950). This instability usually has a morphology of spikes or bubbles. R-T instability can occur in laser produced plasmas in two different situations. One of the cases is when the

laser plasma expands in the presence of an ambient gas (Betti et al., 1998), and the other situation is when the laser plasma expands in the presence of a magnetic field.

When a laser produced plasma is expanding in the presence of an ambient gas, the growth rate of this instability is written as (Betti et al., 1998)

$$\eta^2 = -ka\left(\frac{\rho_p - \rho_g}{\rho_p + \rho_g}\right) \qquad (1.45)$$

where k is the wave number, g is the acceleration of the interface between the plasma and ambient gas and ρ_p and ρ_b are density of ablated material and ambient gas respectively. When $\eta^2 > 0$, the boundary is R-T stable, and if $\eta^2 < 0$, it is unstable (Cirisan et al., 2011; Kumar et al., 2006). The initial perturbations in laser plasma may arise due to the spatial laser beam distribution. So, the wavelength of the perturbations can be taken as the diameter of the laser spot. It is observed that the R-T instability can induce magnetic fields in the laser produced plasmas (Manuel et al., 2012).

This instability can also occur in a laser produced plasma expanding in presence of an external magnetic field. In laser produced plasma, density gradient already exists as a part of formation and expansion of the laser plasma. And a laser plasma is decelerated when it expands in presence of a magnetic field. So a laser plasma expanding in presence of external magnetic field can have classical R-T instability. Another condition which should be satisfied for the existence of classical R-T instability in presence of magnetic field is that the ions should be magnetized (Haverkamp et al., 2008). This instability has been observed by (Ripin et al., 1987). The growth time of the instability can be estimated by (Peyser et al., 1992)

$$\lambda_{RT} = (g_{eff}/L_n)^{-1/2} \qquad (1.46)$$

where g_{eff} is the effective deceleration due to magnetic field and L_n is the density scale length. The growth rate $\gamma_{RT} = 1/\lambda_{RT}$.

1.12.2 Large Larmor Radius R-T Instability

This is similar to classical R-T instability except that it requires the Larmor radius of ions to be greater than the density scale length of the plasma. The growth time of the LLR R-T instability is greater than that of classical R-T instability. The onset criterion for this instability is $\gamma_{RT} > \omega_{ci}$ where γ_{RT} is the growth rate of classical R-T instability and ω_{ci} is ion cyclotron frequency.

1.12.3 Classical Kelvin-Helmholtz Instability

This instability occurs when a fluid or plasma is stratified so that different layers are in relative motion. Similar to R-T instability, this instability can also occur in fluid as well as in plasma. When a plasma is expanding in an external magnetic field, this instability occurs due to electron velocity shear formed because of self-generated spontaneous magnetic field and external magnetic field. The Kelvin-Helmholtz instability depends on the free energy on the velocity shear layer. This does not require a transverse deccelaration of the plasma. The dispersion relation for the Kelvin-Helmholtz instability can be written as (Peyser et al., 1992)

$$\left(\frac{d^2}{dx^2} - k_y^2 + \frac{k_y V_E''(x)}{\omega - k_y V_E(x)} \right) \Phi = 0 \qquad (1.47)$$

The growth time can be obtained from

$$\tau_{KH} = \frac{2\pi}{\gamma_{KH}} = \frac{2\pi}{0.16(V_E/L_v)} \qquad (1.48)$$

Here V_E is the edge velocity, L_v is the shear scale length.

1.12.4 Large Larmor Radius Kelvin-Helmholtz Instability

This arises when the larmor radius of the ions is large compared to the scale length of the plasma. This is also called as Electron-Ion lower hybrid shear instability. By assuming unmagnetized ions and magnetized electrons, the dispersion

relation of K-H instability can be written as (Ganguli et al., 1988)

$$\left(\frac{d^2}{dx^2} - k_y^2 + F(\omega)\frac{k_y V_E''(x)}{\omega - k_y V_E(x)} \right) \Phi = 0 \tag{1.49}$$

where

$$F(\omega) = \frac{\delta^2}{(\delta^2 + 1)(1 - (\omega_{LH}/\omega)^2)} \tag{1.50}$$

and

$$\omega_{LH} = \frac{\omega_{pi}\Omega_e}{(\omega_{pe}^2 + \Omega_e^2)^{1/2}} \tag{1.51}$$

Here ω_{pe} is electron plasma frequency, ω_{pi} is ion plasma frequency, Ω_e is the electron cyclotron frequency and ω_{LH} is called as lower hybrid frequency. The maximum growth rate of this instability is given by

$$\tau = \frac{2\pi}{0.05\,\omega_{LH}} \tag{1.52}$$

This instability is observed in various works such as (Peyser et al., 1992), (Ganguli et al., 1988), etc.

1.13   Applications of Laser Produced Plasma

There are several applications of laser produced plasma. Some are discussed below.

Pulsed Laser Deposition

Pulsed laser deposition is an experimental technique to grow multi-layered thin films and nano-structures using high power lasers (Chrisey and Hubler, 1994; Park et al., 2012). In this technique, a high power laser beam falls on the material which is to be deposited, vaporizes it and converts into plasma state and deposits on the substrate. The quality of the thin film prepared depends on various parameters of the laser such as laser wavelength, pulse width, fluence, ambient gas pressure, substrate temperature, etc. The advantages of this method over traditional thin film deposition techniques includes preservation of stoichiometry, reduced thermal bud-

get (Park et al., 2012) while the disadvantages are non-uniformity of the film and limitation on area of the thin film (Kawasaki et al., 2000).

The pulsed laser deposition method can be improved by using a magnetic field. In aurora pulsed laser deposition method, a magnetic field is used to reduce the splashing effect (Jordan et al., 1997; Minami et al., 2001). It has been reported that the deposition rate of PLD can be increased by using a magnetic field which was attributed to magnetic confinement (Shiraishi et al., 2010). Application of magnetic field during the deposition can also magnetization of the thin films (Wakiya et al., 2007).

Laser Plasma Thruster

Laser produced plasma can be used as a microthruster for satellites (Zheng et al., 2014; Luke et al., 2003; Moeller and Chang, 2007). The basic principle in this method of propulsion is, when a high power laser hits the solid propellent, it forms a crater on the surface of the propellent and material expands thermally to form the thrust (Moeller and Chang, 2007). Presently this technology is in testing and simulation level.

Experimental Simulation of Space Plasmas

Since the laser produced plasma is explosive like most of the astrophysical plasmas, this can be used as an experimental simulation of space plasmas (Zakharov, 2002). Study of collisionless interaction between expanding plasma and ambient magnetic field gives an insight into the dynamics of plasma clouds.

Laser Ion Source

In laser ion source, a dense plasma plume is produced by focussing a higher power pulsed laser beam on a solid target which expands perpendicular to the target surface. An ion optics which contains two grids is placed in front of the target. When the plasma crosses the first grid, a high positive voltage is applied which seperates the ions from the electrons and accelerate the ions towards a second grid

(Ping et al., 1994; Trinczek et al., 2006).

1.14   Motivation, Scope and Objective of the Work

Control of plasma using magnetic field has many applications such as propulsion of space vehicles (Deutsch and Tahir, 2006), exploring astrophysical plasmas (Kelley and Livingston, 2003), pulsed laser deposition (Wakiya et al., 2007), etc. Laser produced plasma is one of the best possibilities in laboratory to study the effect of magnetic field on the plasma dynamics. Since barium has low evaporation temperature, emission from barium cloud can be used to trace the movement of ionospheric plasma. Hence, barium is chosen as one of the target material for the present study. Whereas tungsten is used as a divertor material in ITER Tokomak due to its high melting point and high physical erosion threshold. To understand the properties of tungsten plasma, experiments are also performed with tungsten target in the present work. Study of the expansion dynamics and spectroscopy of laser produced plasmas from these targets can give more insight into these active areas of research.

The major objectives of the present thesis includes

- To study the effect of magnetic field on laser produced barium plasma and estimate various plasma parameters such as electron temperature, electron density, magnetic diffusion time, etc.

- To identify different neutral and ionic components in the expanding plasma and understand their origin using time-of-flight spectroscopy.

- To explore the effect of ambient Ar gas at various pressures on the expanding plasma plume and propose a model.

- To study the dynamics of plasma using imaging technique at various magnetic fields and ambient Ar gas.

1.15 Proposed Contents of the Thesis

An introduction to plasma physics and some of the basic parameters of a plasma are discussed in this Chapter (Chapter 1). Atomic processes, waves, instabilities of the plasma are briefly explained. It also includes a report of literature survey.

Experimental setup is presented in Chapter 2. Various equipment that are used in the experimental setup and their specifications are discussed here. The design and profile of the magnetic trap used for the experiments is also included in this chapter.

The results related to the time of flight spectroscopy as well as emission profiles of different neutral and ionic lines from barium plasma in the absence and presence of magnetic field are discussed in Chapter 3. We have explained different components of plasma using Shifted Maxwell Boltzmann distribution and proposed possible mechanisms of formation of these components.

The effect of magnetic field and ambient gas on the time of flight of barium plasma is reported in Chapter 4. The diamagnetic cavity model proposed explains the observed pressure independent behaviour of the temporal profiles of ionic lines.

Chapter 5 narrates imaging studies of tungsten and barium plasmas. Here we report the instabilities of barium and tungsten plasmas due to magnetic field as well as ambient gas. Instability observed at 10^{-5} Torr in presence of magnetic field, is attributed to electron-ion hybrid instability. We also report irregularities of the plume at higher pressures of Ar (1 Torr, 3 Torr) and attribute it to R-T instability.

Conclusions and future scope of the work are discussed in Chapter 6.

CHAPTER 2

EXPERIMENTAL DETAILS

Various experimental techniques used in the thesis are discussed in this chapter. A brief discussion of different instruments used in the experimental setup is also given. The development of magnetic trap for the experiments, results of simulated as well as experimentally measured profiles of magnetic field are also discussed in detail.

2.1 Introduction

When a high power laser pulse is incident on a target material, a luminous plasma is formed (Radziemski and Cremers, 1989; Singh and Thakur, 2007). The laser produced plasma can be diagnosed using various techniques such as optical emission line profiles (Rothenberg et al., 1985), time resolved spectroscopy (Kwok et al., 1997), laser induced flourscence (Dreyfus, 1991), mass spectroscopy (Davanloo et al., 1990), fast imaging (Peyser et al., 1992; Harilal et al., 2003), electric (Pappas et al., 1992) and magnetic probes (Stamper, 1991), etc. The experimental study in this thesis use mainly three diagnostic techniques, namely, recording of emission lines, time-of-flight studies and fast imaging. The details of various equipments and diagnostic tools used are described below.

2.2 Equipments Used

2.2.1 Laser System

A Q-switched Nd:YAG laser Continuum Powerlite 9030 (Instruction Manual, Continuum Powerlite 9030) having fundamental wavelength of 1064 nm, pulse width of 8 ns and maximum energy of 1.6 J is used for producing plasma. The laser can be operated at 30 Hz and also in single pulse mode. For the present experiments,

the laser was operated only in the single pulse mode. This laser is having top hat intensity profile with a beam divergence of less than 6 mrad.

2.2.2 Vacuum System

The vacuum system comprises of a vacuum chamber having 28 view ports fitted with CF100 as shown in Fig. 2.1. A Rotary (Hind High Vacuum, ED30)
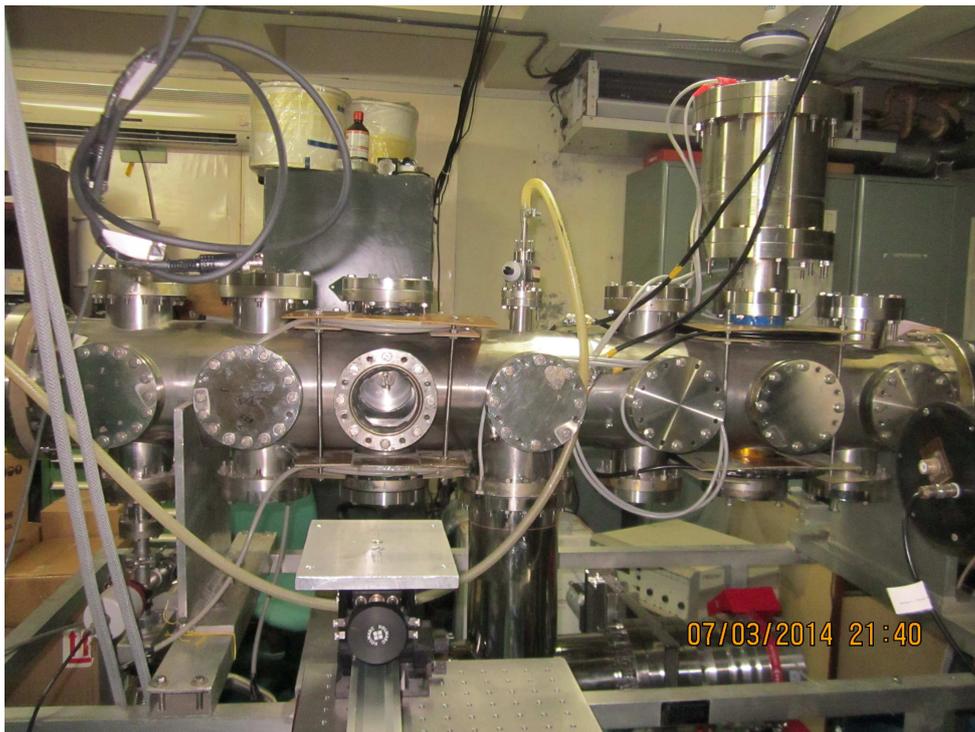
Figure 2.1 Photograph of the Vacuum chamber

and a Turbo Molecular Pump (Pfeiffer Vacuum, TC 400) were used to evacuate the chamber to a base pressure of 2×10^{-5} Torr. The rotary pump had a maximum pumping speed of 500 l/min (Instruction Manual, Hind High Vacuum, ED30) while the turbo had a maximum speed of 355 l/s (Instruction Manual, Pfeiffer Vacuum, TC 400). A gas cylinder provided with a fine needle valve was coupled to the chamber to fill required gas into the chamber. Two pressure gauges were connected to the vacuum chamber, one is pirani gauge and the other one is penning gauge. The pirani gauge was used to monitor pressure from 10^{-4} Torr to atmospheric pressure while the penning gauge was used for monitoring comparatively low pressures.

The experiments in this thesis were carried out by using two target materials, barium and tungsten. Barium (99% purity) (Instruction Manual, Goodfellow Inc.,) was taken in the form of a cylinder of diameter 18 mm. It was stored in an organic oil before and after experiments to prevent oxidization. Tungsten (Instruction Manual, Plansee Inc.,) was taken as a plate of 1 mm thickness. Few laser pulses were fired to ablate the surface layer on the target material before taking the actual data to remove oxidization or any other surface impurities. The target was mounted inside the chamber by using a Wilson feed-through so that the position of the target can be changed during the experiment.

2.2.3   Magnetic Trap

A magnetic trap was designed by using COMSOL Multiphysics code (COMSOL Multiphysics Simulation Software (ver. 4.2), 2011). It comprises of two rare earth magnets made of an alloy of Neodymium, Iron and Boron (NdFeB). The dimensions of the magnets are 76 mm length, 76 mm width and 38 mm height and magnetized in the direction of height (y-direction). The two magnets are kept in a holder made up of stainless steel shown in the Fig. 2.2 in a configuration that north pole of one magnet is facing south pole of the other. The separation between the magnets can be changed continuously using screws provided in the holder. By separating the magnets at three different distances 30, 40 and 50 mm, magnetic fields of 0.3, 0.45 and 0.52 Tesla could be achieved.

The simulated results of direction and magnitude of magnetic field when the magnets are separated by a distance of 40 mm are shown in Fig. 2.3. The coordinate system used to describe the field is also shown in the same figure with origin being at the midpoint of the line joining the centres of the two magnets. Simulation results showed that a field of 0.44 Tesla can be produced at the centre of the two magnets in y-direction. From the figure, it is clear that the magnitude as well as direction of the field is almost uniform in a volume of 50 x 50 x 30 mm^3 between the two magnets. The target was placed 25 mm off centred so that plasma expands in a uniform magnetic field.
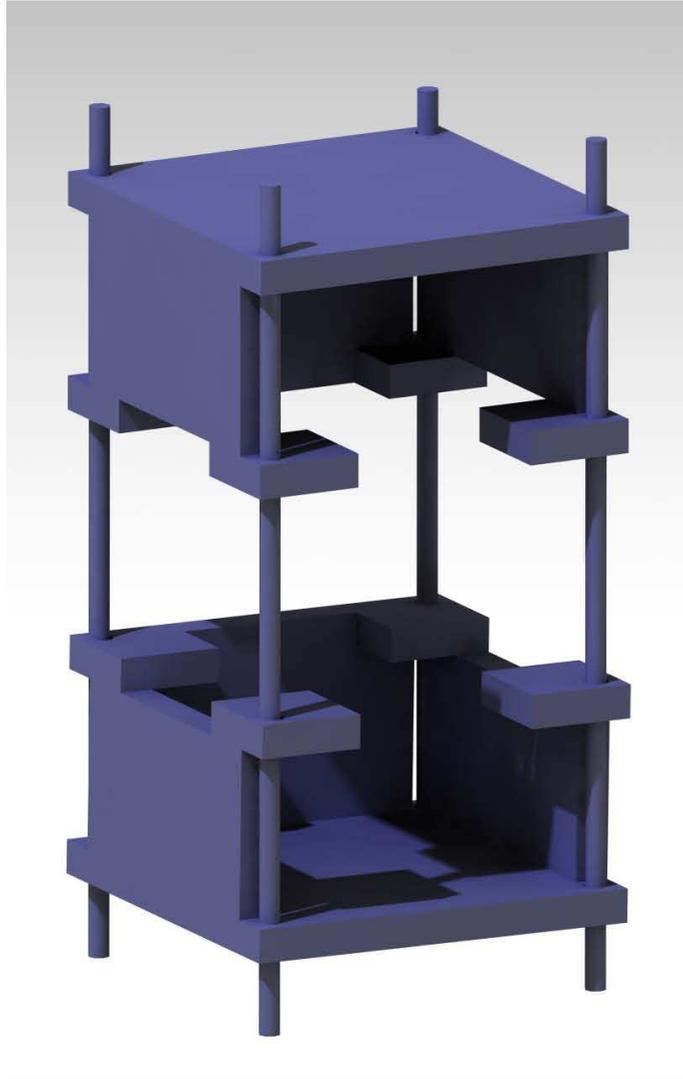
Figure 2.2 Schematic of the holder for the magnets

The field was measured experimentally by using a Gauss meter and is shown in Fig. 2.4. as a function of distance along the plume expansion axis (z-axis) as well as perpendicular to it (x- axis). Magnetic field has a value of 0.45 Tesla at the centre of the magnetic trap. Two more magnetic fields of 0.3, 0.52 Tesla were obtained by adjusting the distance between the magnets to 50 mm and 30 mm respectively. The field is almost uniform in these two cases also. The minimum distance between the two magnets was chosen as 30 mm so that there is no physical interaction of plasma plume with the surface of the magnets.
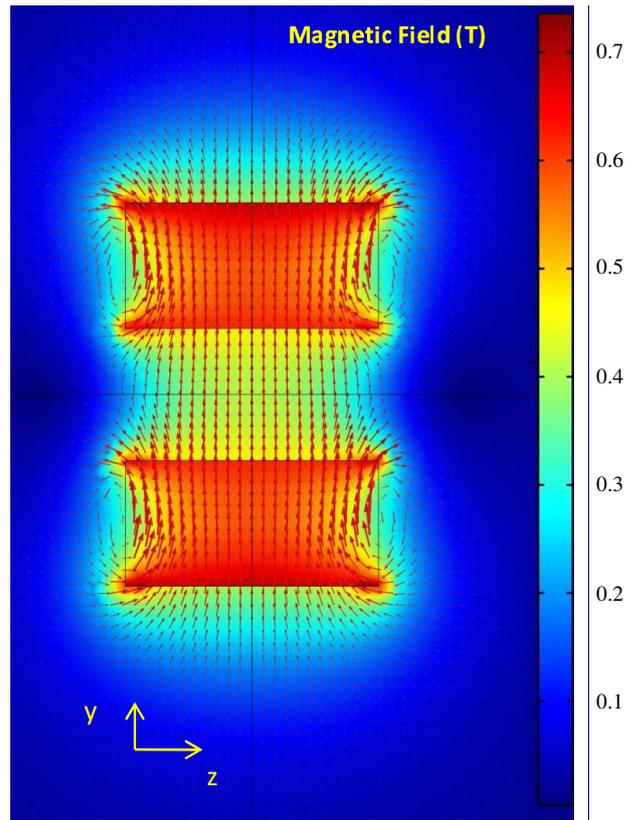
Figure 2.3 Profile of the magnetic field modelled using COMSOL
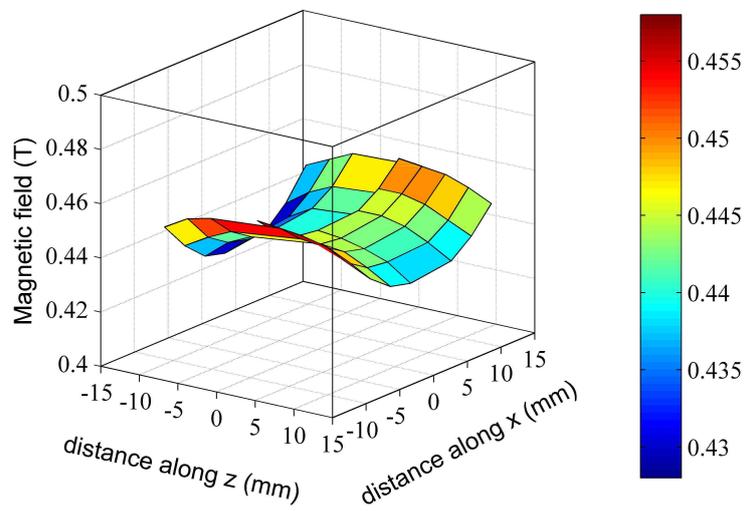
Figure 2.4 Magnetic profile measured experimentally

2.2.4 Monochromator and Spectrograph

Monochromator and spectrograph are optical instruments to disperse the light and measure the relative intensities of radiation at different wavelengths. When light falls on the entrance slit of a monochromator or spectrograph, it forms an image at the exit of the wavelengths present in the source. Difference between a monochromator and a spectrograph is, spectrograph has wider slits and produces relatively broad band of light (Bowley et al., 2012). The output of monochromator has a very narrow band width and considered as monochromatic. To record the broad spectrum of light, the spectrograph is connected to a multi-channel detector such as ICCD while the monochromator is fitted with a single channel detector such as PMT. There are different types of configurations for this instruments. Some of them are:

- **Fastie-Ebert Configuration** In this configuration, the light from the entrance slit falls on the large spherical mirror and is collimated (Signorell and Reid, 2010). The collimated light falls on the plane grating so that it is dispersed. The dispersed light again falls on the other part of the same spherical mirror and forms image at the exit slit. Even though it is a simple design, this configuration has many drawbacks such as spherical aberration, astigmatism, coma, etc.

- **Czerny-Turner Configuration** Here the single mirror in Fastie-Ebert Configuration is replaced by two spherical mirrors. The first mirror is for collimating the input light while the second one is for collimating the dispersed light. This is more flexible compared to the previous configuration and possible to correct coma at a particular wavelength. Drawbacks of this configuration are spherical aberration and astigmatism.

There are different types of spectrographs depending on dispersion element such as grating, prism, etc. Using a holographic grating, it is possible to correct all aberrations present in a spherical mirror at a particular wavelength.

In our experiments, we have used a monochromator (Horiba HR320), and a spectrograph (Acton Advanced SP2500A). HR320 is a 0.32 m coma corrected monochromator in Czerny-Turner configuration (Instruction Manual, Horiba HR320). It uses a holographic grating of 1200 g/mm with a resolution of 0.4 Å at wavelength 546.0 nm. This monochromator is having a scan range of 0-1200 nm. Acton SP2500A is a spectrograph of 500 mm focal length with a resolution of 0.05 nm with a 1200 gr/mm grating at wavelength 435.8 nm. This can have a scan range of 0-1400 nm (Instruction Manual, Acton Advanced Spectrograph SP2500A).

2.2.5   Photomultiplier Tube (PMT)

A photomultiplier tube takes light as input and converts it into corresponding electrical signal. It is a vacuum tube which comprises a photocathode, focussing electrodes, an electron multiplier and an anode. The process of conversion of light into to electrical signal using PMT is as follows:

- Input light falls on the photocathode and releases electrons by means of photo-electric effect. The spectral response of any PMT mainly depends on photocathode.

- Emitted photoelectrons are accelerated and focussed by the focussing electrodes onto the first dynode of the electron multiplier.

- The electron multiplier contains different dynodes where the electrons are multiplied at each dynode by means of secondary emission.

- The secondary electrons from the last dynode are collected by the anode.

The electrical signal from the anode is given to a storage device such as Digital Storage Oscilloscope (DSO) or Digital Phosphor Oscilloscope (DPO) for recording. The PMT (Model R943-02, Hamamatsu) used in the present experiments is having a wide spectral response from 160 nm to 930 nm (Instruction Manual, Hamamatsu PMT R943-02). The photocathode material used in this PMT is

GaAs(Cs). It has a rise time of 3 ns and has almost flat response in the spectral range 400 to 650 nm.

2.2.6 Intensified Charge Coupled Device

An ICCD contains two major parts, one is an intensifier and the other one is a Charge Coupled Device (CCD). The image intensifier comprises photocathode, microchannel plate (MCP), and Phosphor screen. The incident light falls on the photocathode and emits photoelectrons. This photocathode determines the spectral response of the ICCD. A high voltage is applied to MCP such that the photoelectrons emitted by photocathode are accelerated towards MCP and collide with the glass channels of MCP to emit secondary electrons. The electron avalanche leave MCP with a number gain up to 10,000. Electrons from MCP fall on phosphor screen and emits photons. Thus the output of intensifier is also a light, magnified up to 10,000 times compared to the incident light.

A CCD alone without intensifier can also be used for recording an image if sufficient light is available. CCD is an array of silicon-diode photosensor (a pixel). The light falling on a pixel will generate number of electrons proportional to the incident light. The charge collected is sequentially transferred to the read-out amplifier. The amplifier converts charge into voltage where it is stored. The sequence of voltages in all these pixels represents the digital image of the object.

In our experiments, we have used two ICCDs, Andore iStar and Stanford Computer Optics 4 Picos. Andore iStar ICCD is having an optical gating speed of 2 ns (Instruction Manual, Andor ICCD iStar). ICCD 4 Picos is used to capture high resolution images and can operate with a gate time down to 200 ps (Instruction Manual, Stanford Computer Optics ICCD 4 Picos).

2.2.7 Digital Phosphor Oscilloscope (DPO)

This is an electronic device which acquire and store an electronic signal digitally. A DPO uses parallel processing architecture rather than serial technology.

The DPO used in the present experiments, Tektronix DPO 4104, is having an analog bandwidth of 1GHz and sample rate of 5 GS/s (Instruction Manual, Tektronix DPO 4104). It can have a maximum record length of 20 M points with four analog channels.

2.3   Experimental Setup

Schematic of the experimental setup is shown in Fig. 2.5. Plasma plume was generated inside a multiport stainless steel chamber which was evacuated to a base pressure of 5×10^{-5} Torr using a rotary pump (Hind High Vacuum, ED30) and turbo molecular pump (Pfeiffer, TC400). A laser pulse from 1.6 J Nd:YAG laser (Continuum Powerlite 9030) having 8 ns pulse width is focussed on the target inside the chamber by using a lens system. Barium (99 % purity, Good Fellow Inc.,) cylindrical rod of 18 mm diameter and tungsten (99 % purity, Plansee Inc.,) rectangular plate of 1 mm thickness were used as target materials. The laser was focussed to a spot of diameter nearly 1 mm. Most of the experiments were carried out at a laser fluence of 18 J/cm^2. Various fluences of 12, 18, 24, 31 J/cm^2 were used to study the effect of fluence on the plasma dynamics. During the experiment, chamber was filled with argon gas at different pressures 10^{-2}, 10^{-1}, 1 and 3 Torr. All the experiments were carried out in the absence of magnetic field and repeated in presence of magnetic field by keeping the magnetic trap inside the chamber. We have used three experimental techniques viz optical emission spectroscopy, time-of-flight spectroscopy and fast imaging for the study of the plasma and are discussed below.

2.3.1   Optical Emission Spectroscopy

The irradiation of a material with a high power laser produced plasma emits characteristic radiation of the target material. The intensity and broadening of these emission lines can be used to calculate the electron temperature and electron density of the plasma. In this diagnostic, the emission from the plasma is focussed on the entrance slit of the spectrographs using an optical fibre through the view port
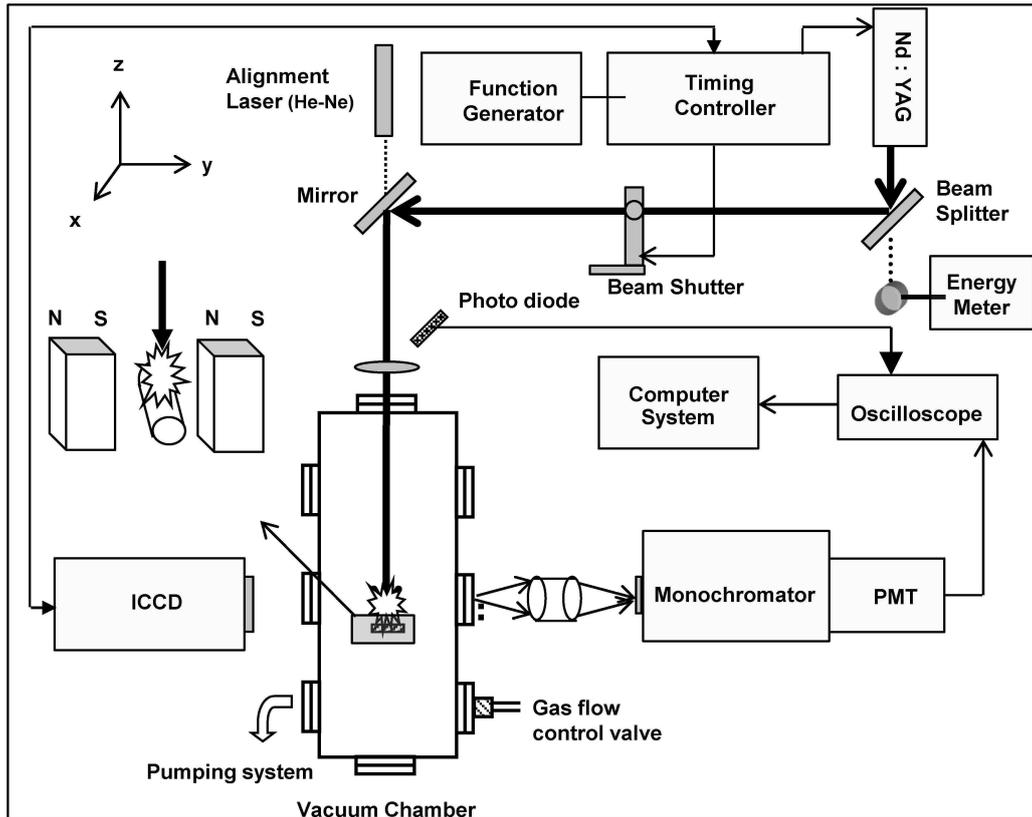
Figure 2.5 Schematic of the experimental setup

onto the entrance slit of the spectrograph (Acton SP2500A). This spectrograph is interfaced with an ICCD (Andore iStar). The spectrum is recorded and data is acquired by a personal computer interfaced to the ICCD. A typical line profile of 455.4 nm line is shown in Fig. 2.6.

2.3.2   Time of Flight Spectroscopy

The velocity distribution of individual constituents of the plasma can be estimated by measuring the delay times of the emission from those constituents at a particular distance from the target surface. In this diagnostic, the plasma is 1:1 imaged on the entrance slit of the monochromator (HR 320) using a lens system. The wavelength of the spectral line to be monitored can be set in the monochromator which is calibrated against the standard spectral lines. The PMT (Model R943-02, Hamamatsu) is coupled to the exit slit of the monochromator so that the optical signal from the monochromator is converted to electrical signal by PMT. This elec-
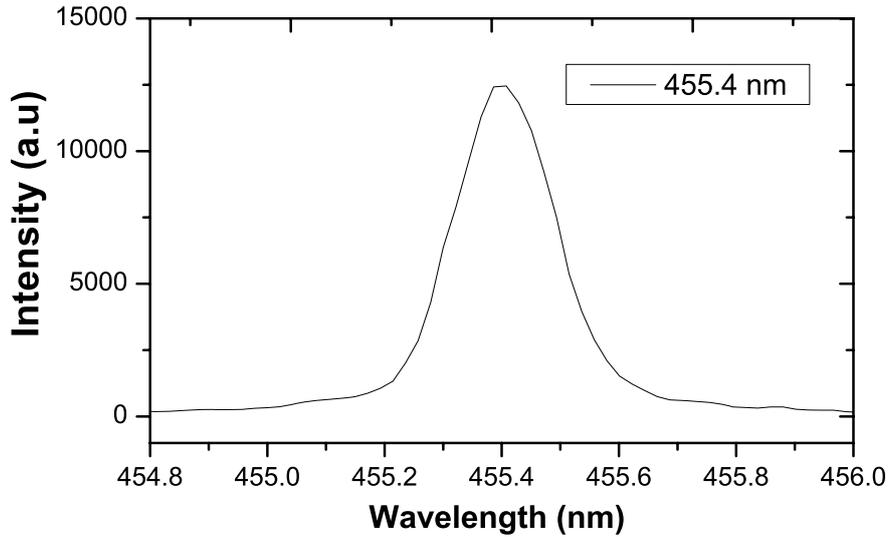
Figure 2.6 Line profile of Ba II 455.4 nm

trical signal is stored in a DPO (Tektronix DPO 4104) which is coupled to the PMT by a 50 Ω termination. The recorded profile is called as time-of-flight or temporal profiles. By moving the monochromator and lens arrangement in the direction perpendicular to the target surface, we can record the temporal profiles at different distances from the target surface. Temporal profiles of two spectral lines barium neutral Ba I 553.5 nm (6s6p $^1P_1 \rightarrow 6s^2$ $^1S_0$), Ba I 577.7 nm (6s6d $^3D_3 \rightarrow$ 6s6p $^3P_2$) and two ionic lines Ba II 413.0 nm (6d $^2D_{5/2} \rightarrow$ 6p $^2P_{3/2}$), Ba II 455.4 nm (6p $^2P_{3/2}$ $\rightarrow$ 6s $^2S_{1/2}$) were recorded at various distances 2 mm, 4 mm, upto 12 mm from the target surface in the present experiments. The DPO is synchronized to the laser system by using a photodiode. The sample rate and record length of the DPO can be changed to record the time of flight profiles upto a required time. A typical temporal profile of Ba I 553.5 nm line at 6 mm distance from the target is shown in Fig. 2.7. Using this temporal profiles, we can estimate the velocity, acceleration of the plume at different time delays.

2.3.3   Fast Imaging

Fast imaging is recording of an ultra-fast phenomena using an ICCD with a gate width of nano-second or pico-second regime. This diagnostic technique is

43
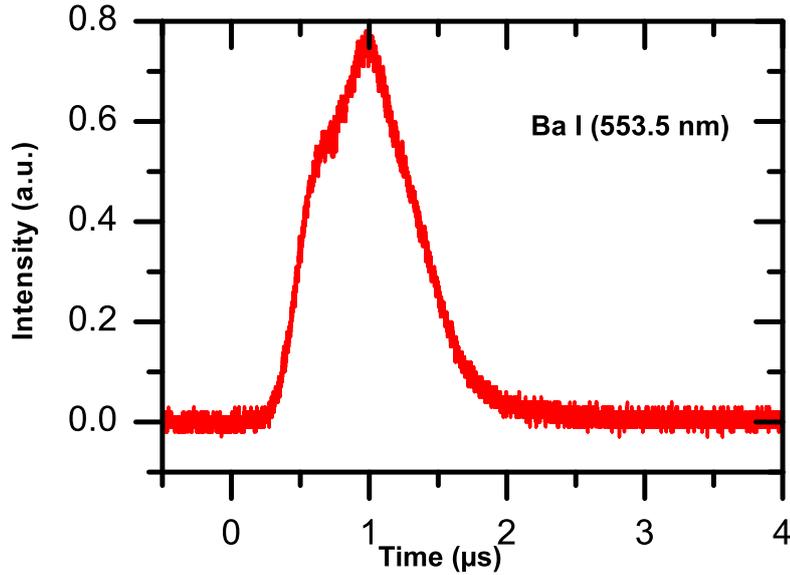
Figure 2.7 Temporal Profile of Ba I 553.5 nm line at 6 mm distance from
the target

used in our experiments for the study of expansion dynamics of barium and tungsten plasmas in the absence and presence of magnetic field. As shown in Fig. 2.5, the ICCD (Stanford Computer Optics 4 Picos) is placed in front of one of the view ports of the vacuum chamber. The ICCD is triggered from the 'SYNC OUT' pulse provided with the Q-switch of the laser. When the laser pulse ablates the target, the ICCD is triggered simultaneously and image of the plasma is recorded at particular delay time specified by 'gate delay' with specified time interval of integrated emission 'gate width'. In the present experiments, the gate width is fixed as 5 ns and the images are recorded at different gate delays 100 ns, 200 ns, etc., upto the disappearance of plasma.

A typical image of the barium plasma at 10^{-5} Torr pressure is shown in Fig. 2.8a. The corresponding processed false-coloured image is shown in Fig. 2.8b where the colour represents the intensity of the emission from the plasma. Using the ICCD imaging, different parameters of the plasma such as plume velocity and acceleration can be estimated. From the plume images, it is possible to observe plume splitting and instabilities of the laser plasma. By using appropriate filters,

44
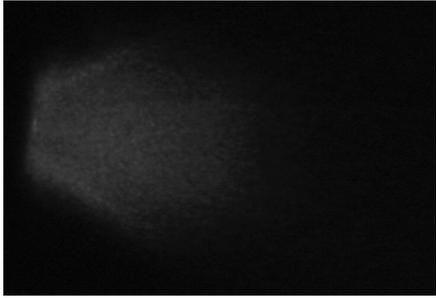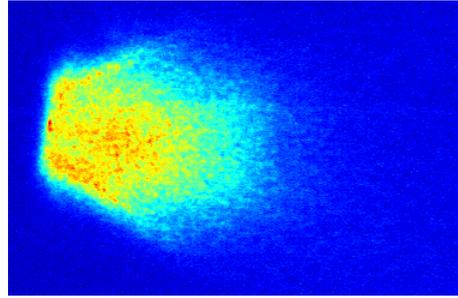
(a) Grey scale image   (b) False-coloured image

Figure 2.8 Images of plsama using ICCD

dynamics of different constituents of plasma can also be studied.

CHAPTER 3

SPECTROSCOPIC AND DYNAMIC STUDY OF BARIUM PLASMA

Expansion dynamics and spectral behaviour of expanding barium plasma in 0.45 T magnetic field in vacuum (10^{-5} Torr pressure) are investigated using time-of-flight spectroscopy and emission profiles. It is observed that the temporal profiles of neutrals are broadened while that of ions showed strong confinement. Various components of the temporal profiles are analysed by fitting with Shifted Maxwell Boltzmann (SMB) distribution. Temporal profiles of neutral line 553.5 nm are well fitted with two SMB components in the absence of magnetic field while the profiles could only be fitted with three components in presence of magnetic field. Ionic profiles are best fitted with two SMB components in the absence as well as presence of magnetic field. Possible mechanisms of various SMB components are explained on the basis of collisions among plume species and correlated to electron temperature, electron density, magnetic diffusion time, etc. The ionic profiles showed efficient confinement in the presence of the magnetic field at higher fluences.

3.1   Introduction

Optical emission spectroscopy is a useful diagnostic to find space and time resolved measurements of electron temperature and electron density of a laser produced plasma which are fundamental for the analysis of a plume evolution (Amoruso et al., 1999). Two spectroscopic diagnostics are used in the present experiments, namely, time-of-flight spectroscopy (Kumar et al., 2009; Singh et al., 2007) and emission line profiles (Amoruso et al., 2004). Line profile of neutral and ionic spectral lines can be used for determining the plasma parameters (Griem, 2012) while the time-of-flight spectroscopy can be used to identify different components in a plasma, to understand the origin of those components (Bulgakova et al.,

2000), and to estimate the velocity of neutral and ionic species in plasma (Harilal et al., 2004), etc. Effect of magnetic field on the emission from the plasma can be studied using optical emission spectroscopy (Pagano et al., 2009; Dirnberger et al., 1994; Kumar et al., 2010b; Li et al., 2009).

This chapter presents the investigation of the expansion dynamics and spectral behaviour of laser produced barium plasma expanding in 0.45 T transverse magnetic field in vacuum (10^{-5} Torr pressure) using time-of-flight optical emission spectroscopy. The experiments are carried out in the absence and presence of magnetic field to understand the effect of magnetic field. The time of flight profiles are used to find the dynamics of neutral and ionic species in ground state and excited states. The emission intensity of different transitions in laser produced plasma gives an insight into their respective densities of states as well as atomic processes inside the plasma. The electron temperature and electron density of barium plasma are estimated from the optical emission spectroscopy.

To elucidate different components in neutral and ionic species, respective temporal profiles are fitted with Shifted Maxwell Boltzmann (SMB) distribution. This study results in understanding the dynamics and origin of different components of a particular species. The results are explained on the basis of collisions among different species as well as metastable and Rydberg states in the barium plasma. Effect of fluence on the barium plasma is also studied in the absence and presence of magnetic field.

3.2   Experimental Setup

The details of the experimental setup are discussed in Chapter 2. An 18 mm diameter solid barium rod (purity better than 99 %) was used as the target. The target was mounted on a movable target holder through vacuum compatible feed-through, for the fresh positioning of the target after exposure to the laser beam. An Nd:YAG (Wavelength of 1064 nm) laser having 8 ns pulse width was used in the present study. Spot size of the laser beam was $\approx$ 1 mm diameter at the target. By

adjusting the operating parameters of the laser, fluence was varied from 12 - 31 J/cm^2 at the target surface. For time and space-resolved spectroscopy, the plasma plume was viewed, using 1:1 imaging optics, normal to the direction of expansion and was imaged at the entrance slit of a 0.35 meter monochromator. By translating the imaging optics along the direction normal to the target surface, time of flight profiles were recorded at different distances from the target surface. In order to record the line profiles of emitting species, an emission signal was imaged on the entrance slit of a spectrograph (Acton Advanced SP2500A).

A magnetic trap was fabricated using two rectangular Nd-Fe-B permanent magnets fixed in a mount made of stainless steel as described in chapter 2. The dimensions of each magnet were 38 mm height, 76 mm length and 76 mm width and the magnetization of each magnet was in the direction of height. The distance between the magnets was fixed as 40 mm. The magnetic flux was measured by a Gauss Meter and the distribution of magnetic field is discussed in detail in Chapter 2. The magnetic mapping results showed that if the above two magnets are placed with north and south poles facing each other, a nearly uniform field can be obtained in the direction perpendicular to the plasma expansion at the centre of the two magnets. Special care has been taken to maintain similar experimental conditions (e.g., laser energy, spectrometer positions etc.) for acquiring the data in the presence and absence of the magnetic field.

In the present study, two spectral lines from neutral barium Ba I 553.5 nm ($6s6p\ ^1P_1 \rightarrow 6s^2\ ^1S_0$), Ba I 577.7 nm ($6s6d\ ^3D_3 \rightarrow 6s6p\ ^3P_2$) and two ionic lines Ba II 413.0 nm ($6d\ ^2D_{5/2} \rightarrow 6p\ ^2P_{3/2}$), Ba II 455.4 nm ($6p\ ^2P_{3/2} \rightarrow 6s\ ^2S_{1/2}$) are chosen for investigating the effect of magnetic field on the characteristic evolution of laser produced barium plasma plume. Temporal profiles of these lines were recorded at various distances from 2 mm to 12 mm from the target surface while the emission profiles are recorded at 6 mm distance from the target surface at different time delays from 100 ns till the plasma disappeared. Experiments were also carried out at various fluences from 12 to 31 J/cm^2. The standard spectroscopic data such as energy levels, transition probabilities, and multiplicities

Table 3.1 Characteristics of Emission Lines Studied

Wavelength λ (nm)	Emitting Species	Transition $(k{\rightarrow}i)$	Transition Probability A_{ki} (s^{-1})	Statistical Weight		Energy (eV)	
				g_k	g_i	E_k	E_i
553.5	Ba I	6s6p ^{1}P$_1$ $\rightarrow$ 6s^2 ^{1}S$_0$	1.19 $\times 10^8$	3	1	2.2391	0
577.7	Ba I	6s6d ^{3}D$_3$ $\rightarrow$ 6s6p ^{3}P$_2$	8.0 $\times 10^7$	7	5	3.8209	1.6756
413.0	Ba II	6d ^{2}D$_{5/2}$ $\rightarrow$ 6p ^{2}P$_{3/2}$	2.18 $\times 10^8$	6	4	5.722	2.7217
455.4	Ba II	6p ^{2}P$_{3/2}$ $\rightarrow$ 6s ^{2}S$_{1/2}$	1.11 $\times 10^8$	4	2	2.7217	0

are taken from the NIST database (Kramida et al., 2014) and are summarized in Table 3.1.

3.3   Results and Discussion

3.3.1   Temporal Profiles of Neutral and Ionic Lines

Temporal profiles of neutral line Ba I 553.5 nm and ionic line Ba II 455.4 nm at different distances both in the absence and presence of 0.45 T magnetic field are shown in Figure 3.1. The temporal profiles were recorded at distances 2 to 12 mm away from the target surface with the laser fluence set as 18 J/cm^2. It is very evident that there is a remarkable difference in the temporal profiles of neutral as well as ionic lines in the presence of the magnetic field compared to those of field free case. At z = 2 mm, a sharp increase of intensity of the temporal profile in the early stage of the plasma is attributed to the contribution from Bremsstrahlung emission.
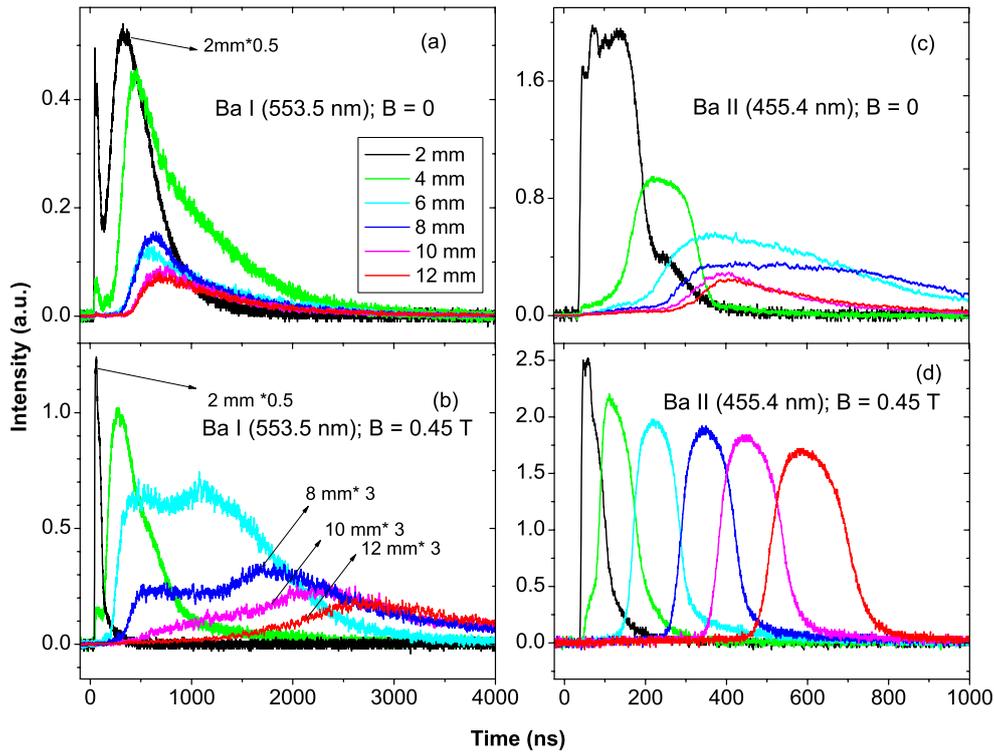
Figure 3.1 Temporal profiles of Ba I 553.5nm line (a) without field, (b) with field; Ba II 455.4nm line (c) without field, (d) with field at fluence 18 J/cm^2.

In the field free case, the temporal profile of 553.5 nm line showed a well defined single component structure at distance z = 2 mm. As the distance is increased, an elongated tail appeared in temporal profiles from $z \geq$ 4 mm which clearly indicate the appearance of another component. Intensity of peak as well as elongated slow components gradually decrease with increasing distance from the target. On the other hand temporal profiles of neutral lines were completely modified in presence of magnetic field. The effect of magnetic field is more prominent at $z \geq$ 6 mm where the emission intensity is increased drastically, especially in the region of delayed broad shoulder of the profile. At far away from the target ($z >$ 8 mm), the intensity of the initial emission is reduced considerably. However field induced enhanced emission at the delayed part of the plume persist up to 5000 ns in the presence of magnetic field.

51

Scenario is completely different in the case of ionic emission profile (Ba II 455.4 nm). The ionic profiles are much faster and narrower in comparison to the temporal profile of neutral species in the absence of magnetic field. However, significant contribution of the slow components in the ionic emissions are observed for the distance $z > 4$ mm as slower portion of the plume extended up to longer flight times. In contrast to the Ba I emission, strong confinement of the temporal extent of Ba II lines is observed by introduction of magnetic field and the overall profile becomes narrower, particularly for the distance $z > 4$ mm. Interestingly, overall emission intensity of 455.4 nm emission is increased with distance in presence of magnetic field. This shows that all emitting ionic species are confined in a small volume which resulted in sharp increase in peak intensity in presence of magnetic field.

3.3.2 Effect of magnetic field on emission intensity of neutral and ionic species

In order to understand the effect of magnetic field on emission yield from neutral and ionic Ba species, we have presented the total emission intensity as a function of distance from the target and is shown in Figure 3.2. The total intensity was obtained by taking the area under the temporal profile which is roughly proportional to the number density of excited species present at distance z. Here the maximum uncertainty in the measurement of total emission intensity was estimated as 5 %. Figure 3.2 shows the spatial variation of emission intensity for the Ba I 553.5 nm, Ba I 577.7 nm, Ba II 413.0 nm and Ba II 455.4 nm as a function of distance and in the absence and presence of 0.45 T magnetic field. Due to the significant contribution of Bremsstrahlung radiation at $z = 2$ mm, this distance is not considered in Figure 3.2. In the case of Ba I 553.5 nm, conventional decreasing trend of emission intensity is observed with distance from the target both in the presence and absence of magnetic field. However, in the presence of magnetic field, a significant enhancement in emission intensity is observed throughout the considered spatial range. On the other hand, Ba I 577.7 nm line showed a different
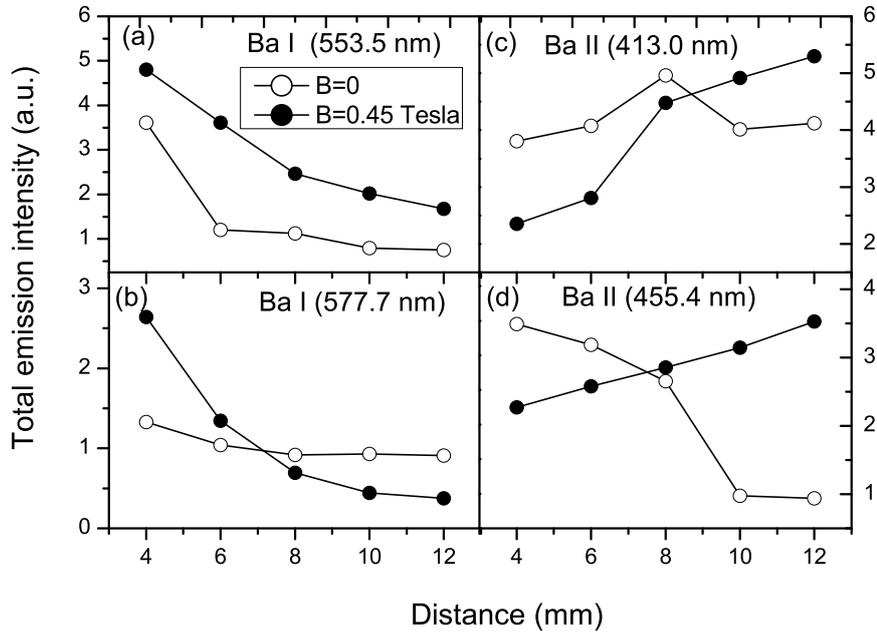
Figure 3.2 The variation of intensity with distance from the target in the presence and absence of field (a) Ba I 553.5 nm (b) Ba I 577.7 nm (c) Ba II 413.0 nm (d) Ba II 455.4 nm at fluence 18 J/cm^2.

behaviour when compared to the Ba I 553.5 nm line. In presence of magnetic field and at $z > 6$ mm, integrated intensities of 577.7 nm line are less than the intensity observed in the field free case.

Peculiar behaviour of barium plasma is clearly observed in spatial variation of emission intensity of ionic species. In case of high lying Ba II 413.0 nm line, the emission intensities are almost the same at various distances in the absence of magnetic field within a statistical error of 5% (except at $z = 8$ mm). In contrast to Ba II 413.0 nm line, the integrated intensity of Ba II 455.4 nm resonance line decreases in field free case. In presence of magnetic field, enhancement in intensity is observed for both the ionic lines at distances 10 mm and 12 mm. At $z = 12$ mm, enhancement factor with respect to field free case is more ($\sim$3.5 times) in the case of 455.4 nm line compared to that of 413.0 nm line ($\sim$ 1.3 times). This observation reveals that different electronic transitions respond differently to magnetic

53

field which may be due to the excitation/ionization mechanisms of different states in expanding barium plasma (Kumar et al., 2010a).

3.3.3 Estimation of Electron Temperature and Electron Density

In the present work, electron temperature is estimated from the ratio of intensities of the two spectral lines of Ba I 553.5 nm and 577.7 nm at 350 ns delay time using the following relation (Shen et al., 2007)

$$\frac{I_1}{I_2} = \frac{g_1}{g_2} \frac{A_1}{A_2} \frac{\lambda_2}{\lambda_1} e^{-\frac{(E_1 - E_2)}{KT_e}} \tag{3.1}$$

Here I_1, I_2 are the intensities of the spectral lines of wavelengths λ_1 and λ_2; g_1, g_2 are the statistical weight factors, A_1, A_2 are the transition probabilities, E_1, E_2 are the energies of the excited states of the two spectral lines, k is the Boltzmann's constant and T_e is the electron temperature.

The spatial variation of electron temperature is shown in Figure 3.3. It is
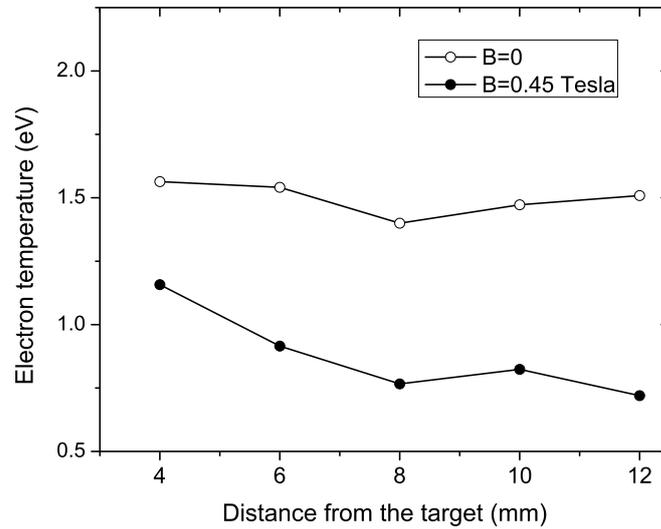
Figure 3.3 Variation of electron temperature as a function of distance from the target in the absence and presence of the field at fluence 18 J/cm^2.

important to note here that this variation is different from the earlier reported results in laser produced plasma. It is observed that the Ba plasma plume does not cool rapidly as in the case of a conventional laser plasma. In the absence of the magnetic field, the electron temperature is almost constant (within the statistical error) with the spatial position up to z = 12 mm. This observation suggests the heating of plume during the expansion. The electron temperature is found to be lower in the presence of the magnetic field at all the distances compared to that in the absence of magnetic field and it decreases with distance. This may be because of increased collisions due to the confinement of plasma in the magnetic field which causes more energy dissipation and hence lowers the electron temperature (Singha et al., 2001).

The electron density n_e in the present experiments is deduced by the relation (Harilal et al., 2005c)

$$\Delta\lambda_{1/2} \;=\; \frac{2Wn_e}{10^{16}} \tag{3.2}$$

where $\Delta\lambda_{1/2}$ is the FWHM of of Stark profile fitted with Lorentzian and W is the electron impact parameter of the Stark broadened line. The contribution of Doppler broadening and pressure broadening are found to be very small and hence neglected in the present experiments. The variation of electron density at different time delays at 5 mm distance from the target is deduced from the Stark broadened profiles of barium 455.4 nm line which is having an electron impact half width of 0.2983 Å (Duan, B. et al., 2013). A typical Stark broadened profile of 455.4 nm at 2000 ns time delay in the presence of the magnetic field is shown in Figure 3.4 (a) and the deduced temporal variation of electron density is shown in Figure 3.4 (b). Here, the maximum uncertainty in density is estimated to be $\approx 14\%$. It is observed that, in the absence of magnetic field, the electron density increases with time delay up to 400 ns, reaches peak value and then decreases. In this case, we are unable to calculate the electron density beyond 1500 ns because of the reduction in the emission intensity. However, in the presence of the magnetic field, a significant emission intensity persists up to 5 μs. It is observed that the electron density is is almost constant upto 5 μs which indicates the ionization of barium atoms during the plasma expansion.
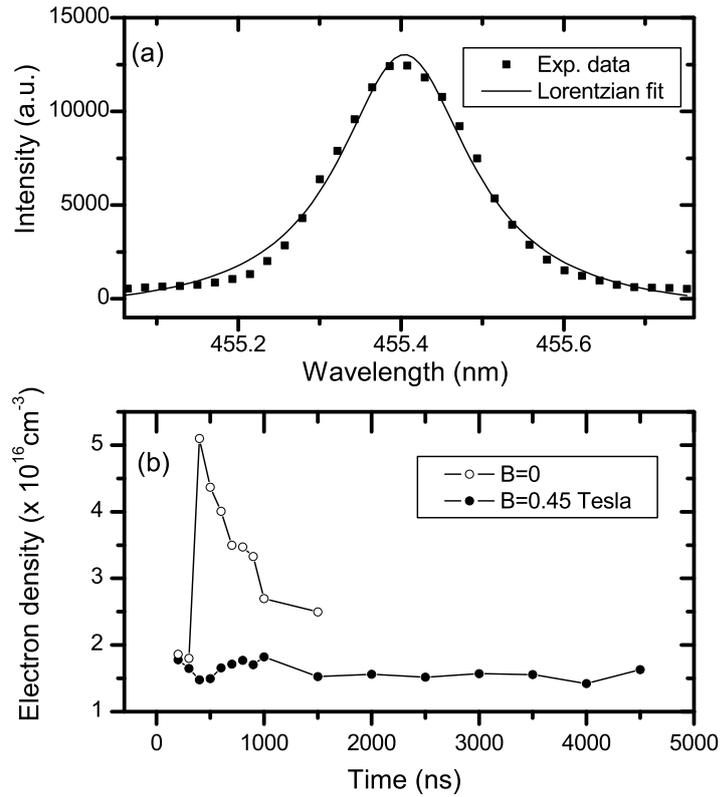
Figure 3.4 Typical Stark broadened profile of Ba II 455.4 nm line at 2000 ns time delay in presence of magnetic field and corresponding Lorentzian fit (b) Temporal variation of electron density in the absence and presence of the magnetic field at fluence 18 J/cm^2.

3.3.4   Local Thermodynamic Equilibrium (LTE) of Plasma

Thermodynamic equilibrium of a plasma requires a spatially, temporally homogeneous and unbounded plasma which is not possible in laboratory plasmas. Instead, we assume that thermal equilibrium relations such as population and velocity distributions are valid in plasma at high electron densities where collisional rates exceed radiative rates by at least one order of magnitude. Such a plasma is said to be in Local Thermodynamic Equilibrium (LTE) (Griem, 2005). It is important to note the Equation 3.1 that we have used for the calculation of electron

temperature is valid only when plasma is in LTE condition. So, we check the validity of the McWhirter criterion for the present plasma conditions which state that the minimum density for LTE is given by (Harilal et al., 2005c)

$$n_e \geq 1.4 \times 10^{14} \, T_e^{1/2} \, (\Delta E)^3 \, cm^{-3} \tag{3.3}$$

where T_e (eV) is the electron temperature and ΔE (eV) is the energy difference between the upper and lower energy levels. In our experiments, for the maximum electron temperature of 1.5 eV and for the largest energy gap of the selected lines of 2.23 eV, this criterion predicts a lower limit for n_e of 1.9×10^{15} cm^{-3}. Our observed values of n_e are always greater than this lower bound, implying that the LTE approximation is valid for our analysis. Here it is also important to check the validity of optically thin plasma to show that the effect of re-absorption of emission is very less since the spectral lines used for determination of electron temperature and electron density of plasma are resonance lines. For the plasma in LTE, the dimensionless quantity optical depth is given by (Aragon et al., 2001)

$$\tau(\lambda) = k_t \, N \, l \, L_s(\lambda) \tag{3.4}$$

where

$$k_t = \frac{e^2 \lambda_0^2}{4\epsilon_0 m_e c^2} f_{ij} \frac{g_i e^{-\frac{E_i}{KT_e}}}{Z(T_e)} \left(1 - e^{-\frac{E_i - E_j}{KT_e}} \right) \tag{3.5}$$

Here $k_t(\lambda)$ is the absorption coefficient, which takes into account the absorption and induced emission processes, l is the length of the emitting region, c is the speed of light, ϵ_0 is the permittivity of free space, m_e is the mass of electron, λ_0 is the center wavelength of the emission line, f_{ij} is the transition oscillator strength, N is the number density of emitting species, T_e is the electron temperature, $Z(T_e)$ is the partition function which depends on the charge state, $L_s(\lambda)$ is the line shape function, and E_i and E_j are the energies of the lower and upper levels respectively. The length of the emitting region was estimated as 10 mm by using fast imaging. The partition functions are determined as 92.19 for Ba neutral and 11.65 for Ba$^+$ and the oscilla-

tor strengths of the lines 553.5 nm and 455.4 nm are taken as 1.64 and 6.9×10^{-1}, respectively, from the NIST database (Kramida et al., 2014). Since these lines are Stark broadened, $L(\lambda)$ is calculated by assuming the Lorentzian lineshape function (Amamou et al., 2002). Optical depth values are estimated as 2×10^{-3} for 455.4 nm line and 5×10^{-4} for 553.5 nm line which concludes that the intensity variation due to self-absorption is almost negligible. Electron temperature is taken as 1.5 eV and electron density is taken as 5×10^{16} cm^{-3} in these calculations. Generally in laser produced plasma, the number density of atoms in different ionization states is slightly less compared to the electron density. Since we have calculated the optical depth assuming the electron density, the resulting optical depth is overestimated. Considering the uncertainty in shot to shot variation in the integrated area of line profiles as $\approx 5\%$, the maximum uncertainty in electron temperature measurement is estimated as $\approx 10\%$.

3.3.5 Distance-time Plots

We have plotted the plasma expansion time t as a function of distance z to understand the interaction of magnetic field with the expanding plasma. Figure 3.5 shows the distance versus time $(z - t)$ plot for ionic as well as neutral emission lines in the absence and presence of magnetic field. Here, the time corresponds to the maximum emission intensity of the respective temporal profiles. In the absence of magnetic field, $z - t$ plot is linear which suggests that the plasma follows free expansion as predicted in the earlier reports (McKenna et al., 2014; Harilal et al., 2004; George et al., 2010). With the help of $z - t$ plot, estimated velocity of barium neutral was $\sim 1 \times 10^6$ cm s^{-1}. Due to the large broadening and nearly flat top profile of Ba II 455.4 nm line (especially at $z = 8$ mm), it is very difficult to measure the peak position. This gave large uncertainty (40 %) in estimating the average velocity of ions with $z - t$ plot. Therefore ion velocity in field free case is estimated by taking the flight time at a desired location which is $\sim 1.9 \times 10^6$ cm s^{-1} at $z = 6$ mm. When magnetic field is introduced, plume experience the resistive force due to the magnetic pressure and therefore expansion velocity reduces with increasing distance. This effect is more pronounced in case of neutrals and at $z \geq 6$ mm
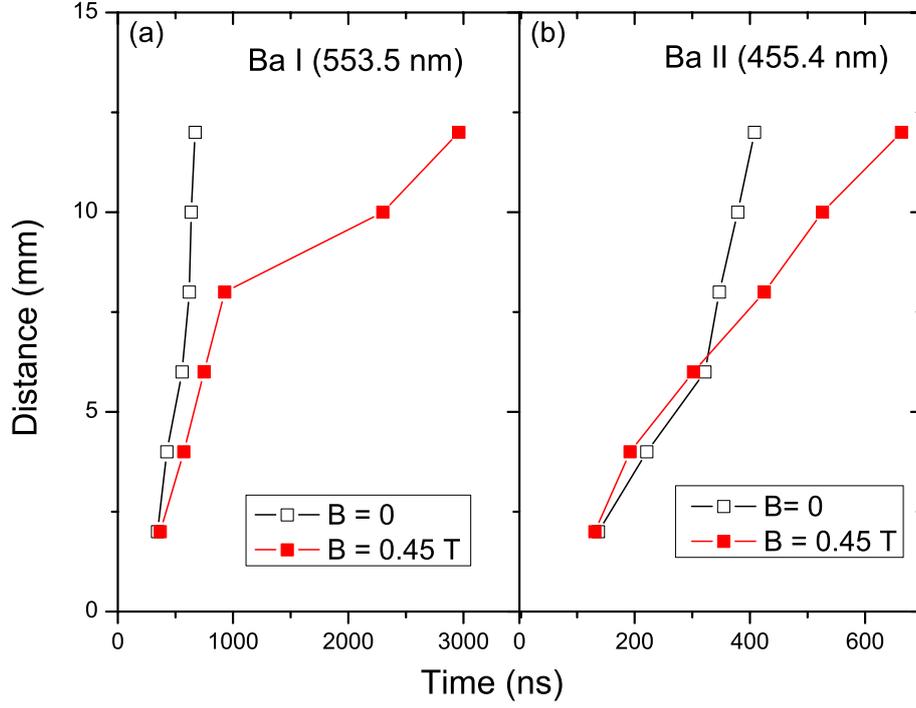
Figure 3.5 Position-time ($z - t$) plots obtained from the temporal profiles.

(a) Ba I 553.5 nm line (b) Ba II 455.4 nm at fluence $18 \mathrm{J/cm}^2$.

where strong deceleration of the plasma plume is observed, as evident in Figure 3.5. The delayed response of the magnetic field on the expanding plasma plume can be correlated with the magnetic diffusion time. The magnetic diffusion time is defined by (Huba, 2004) as

$$t_d = \frac{4\pi\sigma R_b^2}{c^2} \tag{3.6}$$

where σ is the plasma conductivity which can be obtained using the relation (VanZeeland and Gekelman, 2004)

$$\sigma = \frac{50\pi^{1/2}\epsilon_0^2(KT_e)^{3/2}}{m_e^{1/2}e^2 z \ln \Lambda} \tag{3.7}$$

where T_e is the electron temperature, $\ln\Lambda$ is the coulomb logarithm (Pathak and Chandy, 2009).The stopping distance R_b is given by (VanZeeland et al., 2003)

$$R_b = \left(\frac{3\mu_0 E_{lpp}}{\pi B^2} \right)^{1/3}$$

(3.8)

Here E_{lpp} is the kinetic energy of the laser plasma which is approximated as half of the initial laser beam energy and B is the applied magnetic field.

3.3.6 Plasma beta

Using our experimental parameters laser energy of 150 mJ, magnetic field B = 0.45 T, electron temperature 1 eV and electron density 1.5×10^{16} cm^{-3}, the estimated value of t_d is $\sim$ 300 ns. The estimated value of t_d is nearly equal to the arrival time of the ionic species at z = 6 mm. So, the influence of magnetic field effectively starts at 6 mm distance from the target surface which is in agreement with the magnetic diffusion time evaluated. In laser produced plasma, because of high directed velocity, plasma plume is not completely stopped under the influence of magnetic pressure. When the plasma plume expands across magnetic field, the plume behaviour is controlled by different parameters namely, magnetic pressure $(P_B = B^2/2\mu_0)$, plasma thermal pressure $(n_e K T_e)$ and directed pressure $(n_e m_e v^2/2)$ where n_e is the electron density and T_e is the electron temperature. For the present experiments, the magnetic pressure is 8.06×10^4 N/m^2, for electron temperature of 1 eV (at z = 6 mm) and electron density of 1.5×10^{16} cm^{-3}, the plasma thermal pressure is 2.4×10^3 N/m^2, and the directed pressure is 6.5×10^5 N/m^2. The plasma thermal beta is a dimensionless parameter which is defined as the ratio of plasma thermal pressure to the magnetic pressure (Harilal et al., 2004)

$$\beta = \frac{n_e K T_e}{B^2/2\mu_0}$$

(3.9)

In the initial stage of the plasma, the thermal pressure dominates the magnetic pressure. As the plasma expands, plasma pressure decreases and expansion comes to stop when the plasma pressure is balanced by the magnetic pressure and β becomes

unity. After initial conversion of thermal energy into directed energy, the directed beta or β_d becomes an important parameter and is defined as (Harilal et al., 2004)

$$\beta_d = \frac{n_e m v^2}{B^2/8\pi} \tag{3.10}$$

where v is the velocity of the plume. With the above experimental parameters, we have evaluated β_d which is equal to 8 at 6 mm distance from the target surface for the present case. This value of β_d indicates that plasma expands beyond 6 mm but with significant retardation as observed from the $z - t$ plots shown in Figure 3.5.

3.3.7 SMB Analysis of Neutral Species

It has been observed that most of the temporal profiles of both Ba I and Ba II lines showed multi-peak structures and each component interacts differently with magnetic field. Therefore these observations can be more quantitatively understood with the knowledge of distribution of individual components in expanding plume. Since the particle distribution in laser produced plasma can be described by a one-dimensional Shifted Maxwell-Boltzmann (SMB) distribution function and therefore, a multi-component SMB distribution was adopted to resolve the individual components. Figure 3.6 shows the temporal profiles of 553.5 nm neutral line in the absence and presence of magnetic field along with the multi-SMB fit of the data. As evident from Figure 3.6, in the absence of magnetic field each profile of the neutral line is well fitted with two SMB distribution functions and the superposition of these two components exactly reproduce the observed profile of the neutral line. Individual components are hereafter referred to as C1 and C2 etc., with increasing time delay. It is observed that, despite of the decrease of overall intensity with distance from the target, the relative fraction of both the components is nearly same within the statistical error (see Table. 3.2). The above velocity distribution can be understood by the primary ablation mechanism of Ba target with IR laser irradiation. The incident laser beam rapidly heats the localized portion of Ba target and raises its temperature near to its critical temperature. This initiates the phase explosion (Vertes et al., 1993) and therefore material in the form of vapor is ejected
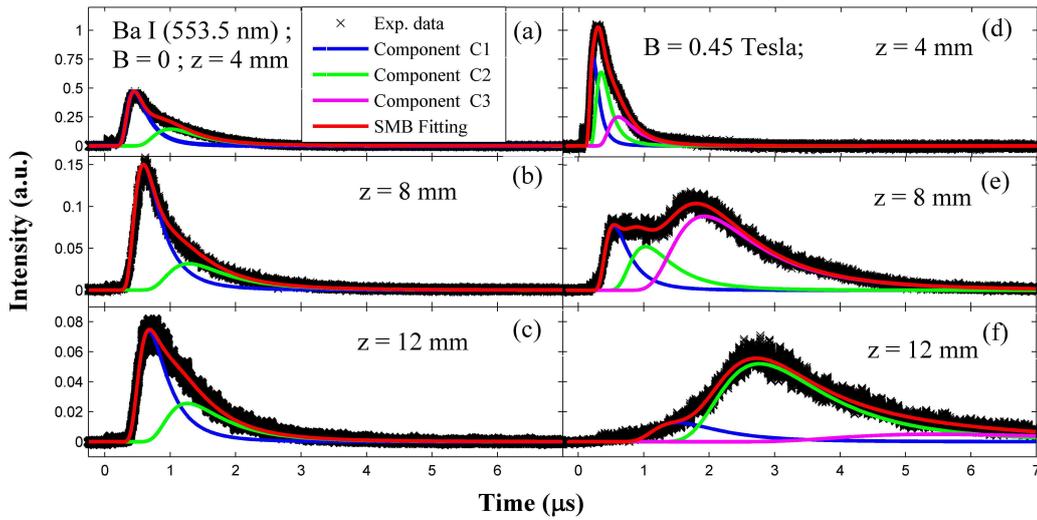
Figure 3.6 TOF profiles obtained and corresponding fits with multiple SMB for Ba I 553.5 nm line in the absence of the field at (a) 4 mm (b) 8 mm (c) 12 mm ; and in presence of 0.45 T magnetic field at (d) 4 mm (e) 8 mm (f) 12 mm with laser fluence 18 J/cm^2

out from the surface with significant translational energy. The incident laser beam having pulse width 8 ns is still on and interacts with dense vapor via free electrons which are ejected from the target surface. The free electrons absorb the laser energy through the inverse Bremsstrahlung process. These heated electrons interact and transfer the energy to the dense plume species and hence the energy is redistributed in ejected species. In this scenario, temperature gradient inside the plume can raise the atoms to excited states and charge states of the ablated species. The plume front is supposed to have maximum interaction with the incident laser beam and high lying excited states or multiple charge states are expected to be in this region.

Rossa et al. (2009) reported that even neutral species of barium can have different velocity distribution for different excited states. The radiative $6s6p\ ^1P_1$ states have maximum velocity followed by metastable $6s5d\ D$ state and slowest one is $^1S_0$ state. At a laser fluence of 10.8 J/cm^2, they estimated population of $^1D_2$ metastable states as 0.6 % and population of ^3D_J metastable states as 10 %

Table 3.2 Percentage fractions of different components of the TOF distributions for Ba I 553.5 nm line

Distance 'z'(mm)	B=0		B=0.45 Tesla		
	Component I	Component II	Component I	Component II	Component III
4	59.06	40.94	30.45	39.53	30.02
8	66.04	33.96	15.74	18.97	65.29
12	58.88	41.12	11.01	72.48	16.51

which are normalized to the ground state and the relative contributions from other excited states are not considered. Also, Matsuo et al. (1999) found that 0.01% of atoms are in the 6s5d metastable states even after 50 μs time delay of laser ablation. In the present study, due to the experimental limitation we are unable to measure the internal state population, especially for the ground and metastable states. Even though, our experimental parameters are different from the above reports, we expect that considerable fraction of atoms exists in $6s^2\ ^1S_0$ state and 6s5d metastable states ($^1D_2$, ^3D_j). In view of above, we propose the possible mechanism for the appearance of different structures in the temporal profile of neutral emission as follows. The first component C1 is attributed to the radiative cascade from the highly excited states which populate low lying radiative states and the second component C2 can be attributed to the collissional excitation, mainly the electron impact excitation from $^1S_0$ state and other low lying states, e.g. 5d D states to 6p $^1P_1$ states. At this stage it is difficult to say which state contribute more to populate $^1P_1$ state. The above argument is supported by the observed results with different values of laser fluence. Figure 3.7 shows the effect of laser fluence on the temporal profile of Ba I 553.5 nm. The large enhancement in emission intensity of 553.5 nm line particularly in the delayed component of the temporal profile is observed with increase of laser fluence around two times. The increase of population of high lying states as well as increase of electron energy (and hence increase of electron impact excitation) with laser fluence by inverse Bremsstrahlung process explains the above
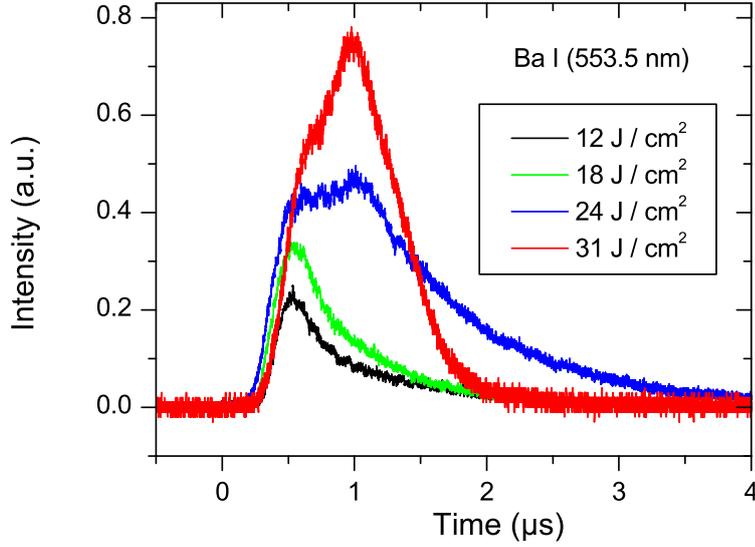
Figure 3.7 Effect of laser fluence on the TOF profiles of Ba I 553.5 nm line
in the absence of magnetic field at $z = 6$ mm.

observations. Here the dominant depopulation channel of $^1D_2$ and ^3D_j metastable
states to ground state is the back transfer to the radiative $^1P_1$ states by the collisional
processes (Vadla et al., 1995), that is

$$^1D_2 \ (^3D_j) \rightarrow \ ^1P_1 \ \rightarrow \ ^1S_0 \tag{3.11}$$
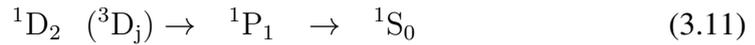
The large cross sections for $^1D_2$ to $^1P_1$ and ^3D_j to $^1D_2$ is also in line with the
above argument (Johnson et al., 1999). Large broadening of the second component
could be correlated with large velocity distribution of slow moving ground state
neutral atoms and presence of significant number of atoms in metastable states hav-
ing lifetime much larger than the time scale of the present experiment (McCavert
and Trefftz, 1974).

In presence of magnetic field, not much difference is observed up to $z =$
4 mm, of course, even though profile is sharper than the observed profile in the
absence of field at 4 mm. This is due to the confinement of the plume in presence
of magnetic field. Enhancement of emission intensity of Ba I lines in the form

of additional third component is observed at $z \geq 6$ mm as shown in Figure 3.1 and Figure 3.6. Comparing the temporal profiles of 553.5 nm emission line both in presence and absence of magnetic field at $z = 8$ mm, shows that the peak positions of the first two components (C1 and C2) are unaffected by the introduction of magnetic field. Only the peak intensities are found to be increased with the magnetic field. Since the velocity distribution of neutral atom is not directly affected by magnetic field (neutral atom does not experience the Lorentz force or gyromotion), it can be inferred that either these components are formed by direct ejection of neutral atoms or neutralized well before the appearance of magnetic field effect. Further the magnetic field cannot influence the initial processes of plasma formation and therefore appearance as additional third component (C3) is purely field induced population of $^1P_1$ states. Moreover, at larger distance, that is at $z = 12$ mm, first component and third components are suppressed considerably. However, in the present data, it is not clear that the observed profile is whether the individual second or third component or the combination of these two components. The above behavior can be understood as follows.

At spatial distance of few mm away from the target (in present case, ≥ 6 mm), confinement of plume occurs due to the presence of magnetic field. The presence of magnetic field also affects the dynamics of electrons and ions. The Larmor radii of ions and electrons in presence of 0.45 T magnetic field are estimated approximately as 6.3 cm and 0.0003 mm respectively, for ion velocity $\sim 2 \times 10^6$ cm/sec. Here we have assumed that electrons and ions are moving with the same velocity. Since the Larmor radius for ions is greater than plume dimension and therefore the ions are not effectively affected by the magnetic field. However, small Larmor radius of electron effectively increases the frequency of electron-atom collisions. Therefore both confinement and Larmor motion of electrons increase the collision processes in the plasma plume. In highly collisional region, collisionally induced electron-ion recombination enriches the population of long-lived Rydberg states (Rossa et al., 2009). Therefore the comparatively broader third component in the presence of magnetic field is attributed to collisional or radiative cascading

from the long lived Rydberg states which populate the $6p\ ^1P_1$ states. The depletion of first component in presence of magnetic field at large distance ($z = 12$ mm) can be explained on the basis of energy pooling between the excited states. Due to the gyro-motion of electrons, and confinement of the plume, apart from the electron-ion collisions, the collisions between the plume species also increase. One of the strongest energy pooling reaction between $Ba^*\ 6s5d\ ^1D_2$ and $Ba^*\ 6s6p\ ^1P_1$ is proposed by (Cubaynes et al., 1987) et. al., and is written as

$$\text{Ba}^*\ (5\text{d}\ ^1\text{D}_2) + \text{Ba}^*\ (6\text{p}\ ^1\text{P}_1) \rightarrow \text{Ba}^{**}\ (7\text{p}\ ^3\text{P}) + \text{Ba}\ (6\text{s}\ ^1\text{S}_0) + 2KT_e \quad (3.12)$$

$$\text{Ba}^{**}\ (7\text{p}\ ^3\text{P}) + \text{Ba}^*\ (5\text{d}\ ^1\text{D}_2) \rightarrow \text{Ba}\ (6\text{s}\ ^1\text{S}_0) + \text{Ba}^+ + \text{e}^- \quad (0.01 \text{ to } 0.04 \text{ eV})$$
$$(3.13)$$
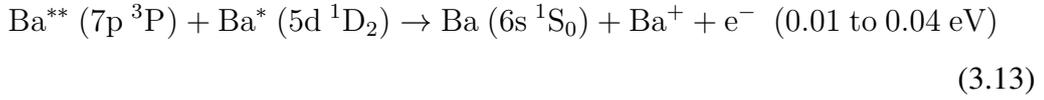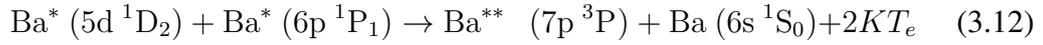
Similar energy pooling collisions are also possible among ^3D_J states to produce excited neutrals and higher charge states (Pneuman, 1983) and the corresponding equation for energy pooling can be written as

$$\text{Ba}^*\ (5\text{d}\ ^3\text{D}_\text{J}) + \text{Ba}^*\ (5\text{d}\ ^3\text{D}_\text{J}) \rightarrow \text{Ba}^{**}\ (\text{n}^{2\text{S}+1}\ \text{L}) + \text{Ba}\ (6\text{s}\ ^1\text{S}_0) \pm \Delta E \quad (3.14)$$
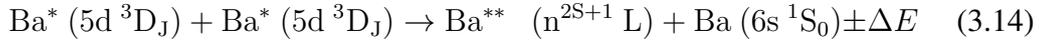
Similar results were also observed by (Bachor and Kock, 1981) where they have reported the depletion in integrated population densities of $^1P_1$ states and an increase in the density of Ba II $^2S_{1/2}$ state with increasing time delay. The presence of a highly collisional region due to the magnetic field induced plume confinement enriches the population of low lying long lived metastable states with the time delay through different routes of collisional de-excitation. Therefore, an increase of energy pooling collisions might be the reason for the observed behaviour of the temporal profile of Ba I at $z = 12$ mm in the presence of the magnetic field. The estimated electron temperature is more in presence of magnetic field, which indicates the increased collisions as explained earlier.

3.3.8 SMB Analysis of Ionic Species

In the case of Ba II 455.4 nm line, it is observed that the shape of the temporal profile is strikingly different from that of Ba I 553.5 nm line as shown in Figure 3.8. In the absence of the magnetic field, snow-plough type of structure
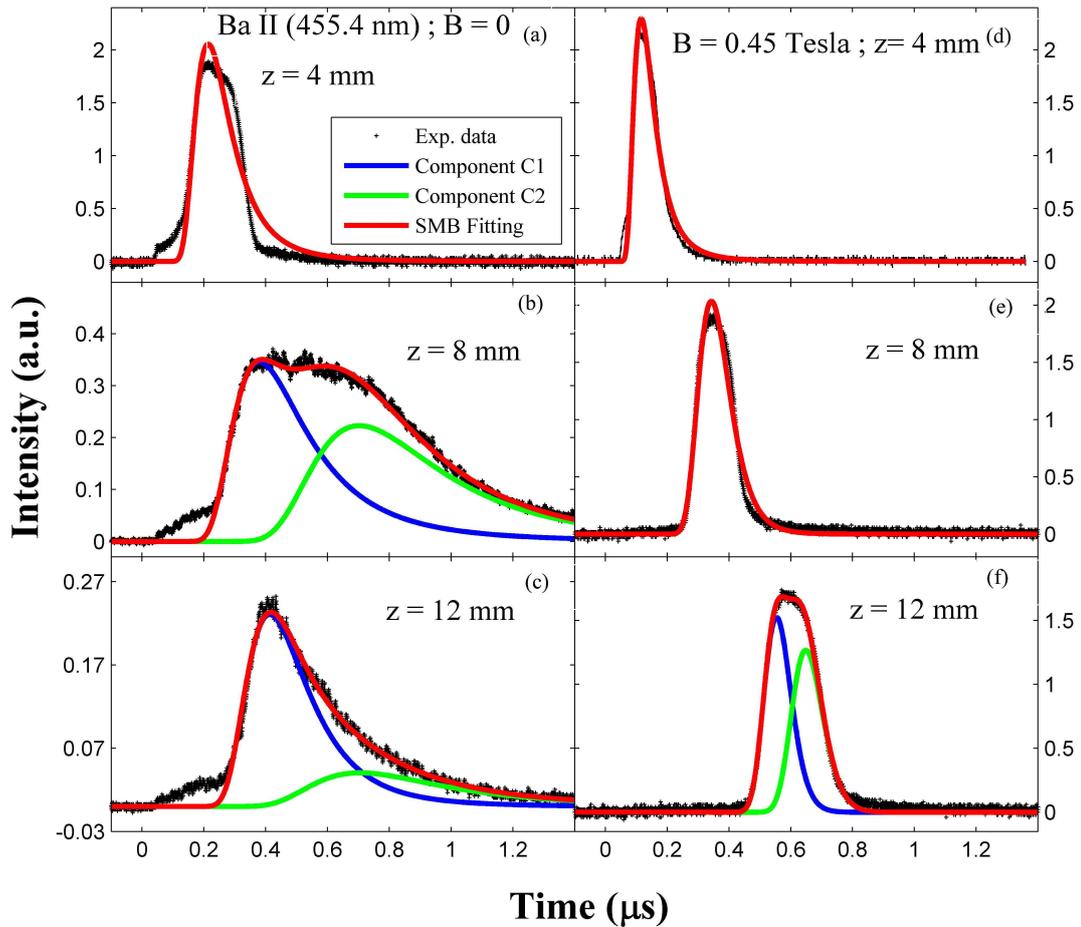
Figure 3.8 TOF profiles obtained and corresponding fits with multi peak
SMB for Ba II 455.4 nm line in the absence of the field at
(a) 4 mm (b) 8 mm (c) 12 mm ; and in presence of 0.45 T field
at (d) 4 mm (e) 8 mm (f) 12 mm at fluence 18 J/cm^2.

appears in the temporal profiles at the distances close to the target ($z \leq 4$ mm). This profile could not be fitted well with two SMB distributions. However, nearly 80 % of the profile can be represented by a single SMB distribution. This struc-

ture was well-explained by (Bulgakova et al., 2000) on the basis of double layer formation. At higher laser fluences as in the present case, energetic electrons are formed due to the absorption of laser energy by the primary electrons through the inverse Bremsstrahlung process. These energetic electrons are well ahead from plume species and ambipolar electric field is developed at plume boundary. This electric field accelerates the ionic species. As time evolves, the excess ions accumulate behind the electrons, shield the ambipolar electric field so that the rest of the ions are not affected by the electric field and get delayed giving rise to the snow-plough structure of the temporal profile. Thus at the early stage of plasma expansion, even though all the emitting ions are formed by the primary ablation process, a fraction of ions is delayed due to the shielding of ambipolar field by accelerating ions.

Apart from the evolution of ionic species formed by the primary ablation process, a well defined second delayed component is observed at distances $z > 6$ mm. At larger time delay, the collisional and radiative de-excitation by high lying states populate the low lying metastable states as well as radiative states. Therefore, the second component can be treated as the additional formation of ions during expansion and might be due to secondary processes such as super elastic collisions between the excited species.

In contrast to the temporal development of Ba I emission in the presence of the magnetic field, strong confinement in Ba II emission is observed as shown in Figure 3.1 and Fig. 3.8. The temporal profile is significantly narrowed and therefore peak intensity is increased as compared to the field free case. Ba II profile is fitted well ($\approx 95\%$) with a single SMB distribution up to $z = 8$ mm (See Table. 3.3). However, at larger distance $z = 12$ mm, two component SMB distribution represent the temporal profile. The quenching of delayed components of ionic species in the presence of the magnetic field could be understood as follows. In the presence of the magnetic field, large collisions between the plume species occur due to the plume confinement. The highly charge states as well as highly excited states rapidly depopulate via collisional and radiative de-excitation. This is reflected in our results, where the large enhancement is observed in the narrow region of time scale in the

presence of the magnetic field.

Table 3.3 Percentage fractions of different components of the TOF distributions for Ba II 455.4 nm line

Distance 'z'(mm)	B=0		B=0.45 Tesla	
	Component I	Component II	Component I	Component II
4	83*	...	94*	...
8	48.12	51.88	93*	...
12	72.25	27.75	50.91	72.48

*is the percentage fraction of area under the profile fitted with the single SMB distribution.

3.3.9 Effect of Fluence on Ionic Species

The effect of the magnetic field on ionic species can be further understood by observing their temporal behaviour as a function of laser fluence. Figure 3.9 shows the time resolved emission features of 455.4 nm line with laser fluence varying from 12 to 31 J/cm^2. These profiles are recorded at z = 6 mm from the target. In case of lower laser fluences, in the absence of the magnetic field, the temporal profiles are relatively broad with an elongated tail which corresponds to the slow moving ions. The temporal profile shrinks sharply, and overall profile becomes narrower with increasing laser fluence. At laser fluence $\geq$ 24 J/cm^2, the trailing portion of the profile almost disappears and an additional fast component appears at the leading edge of the plume. This additional component is probably formed by recombination of Ba^{2+}. Since the Ba^{2+} ions are more influenced by ambipolar acceleration, their velocity is higher than the directly formed Ba^+ ions. This is obvious because with the increase of laser fluence, more laser photons are absorbed by the plasma plume via inverse Bremsstrahlung process and therefore change in relative population of different charge states is expected with varying laser fluence.

69
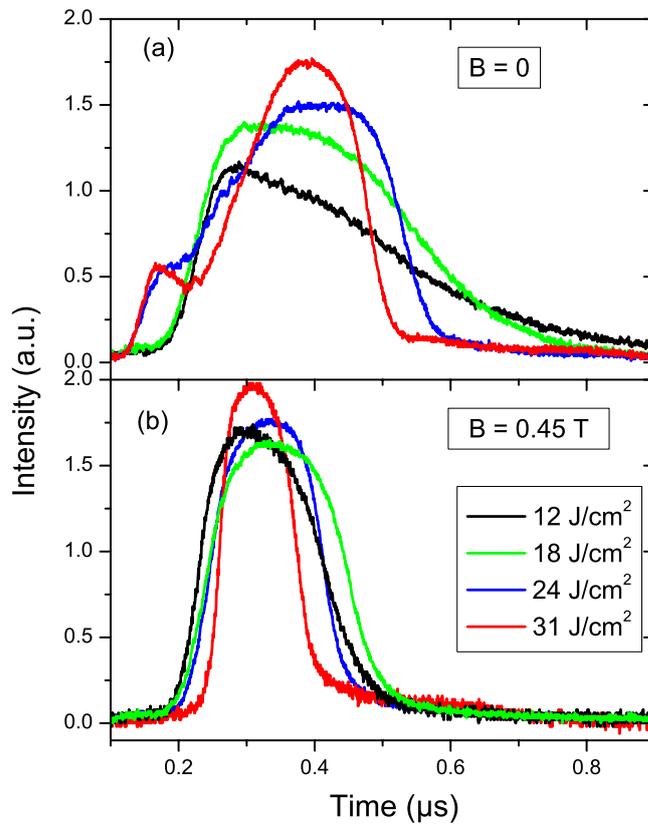
Figure 3.9 Effect of laser fluence on the TOF profiles of Ba II 455.4 nm line
in the absence and presence of magnetic field at $z = 6$ mm.

This argument is supported by spectroscopic data where we observe the emission of Ba III at 637.7 nm and 638.3 nm at 300 ns time delay. Even though, the increase in charge states is observed with an increase in the laser fluence we could not observe any significant change in emission intensity of the 455.4 nm line as shown in Figure 3.9. The relative number densities of the different emitting states are obtained by dividing the integrated intensity under the temporal profiles with the transition probability and statistical weight and is shown in Figure 3.10. However increase of charge states with further increase of laser fluence results in depletion of singly ionized species. This is reflected in our results where the emission intensity of most of the ionic species shows decreasing trend at the higher laser fluences as shown in
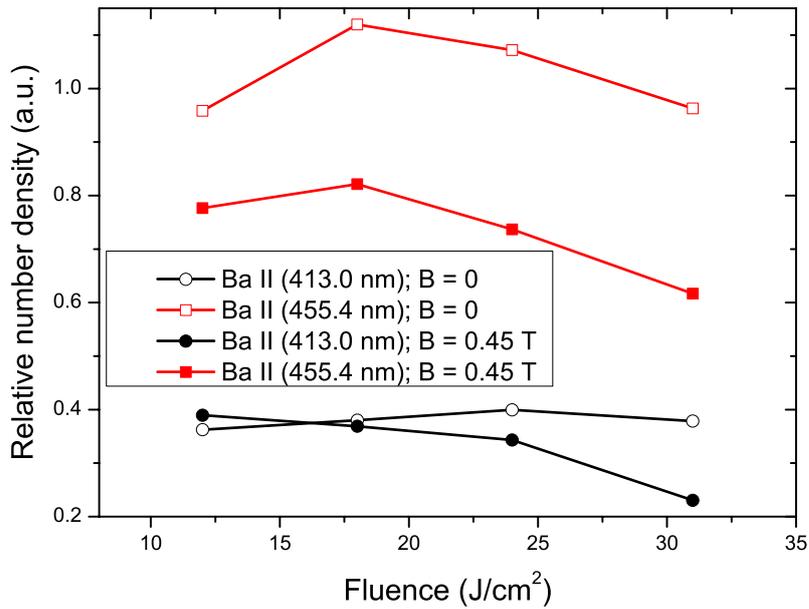
Figure 3.10 Relative intensity of Ba II 413.0 nm and 455.3 nm lines in the absence and presence of magnetic field at different laser fluences.

Figure 3.10. The above discussion is supported by the fact that at least up to $z = 6$ mm, the ionic states are mainly populated by single process, that is radiative or collisional cascade from the high-lying levels. Here population due to electron impact excitation is ruled out. If electron impact excitation was responsible for emission, the emission intensity would have increased with fluence, as the electron density and temperature are expected to be high at higher laser fluences. But, this is not observed in the present case.

The efficient confinement of the plume at higher laser fluence in the presence of the magnetic field also indicates the increase of charge states of ablated barium with laser fluence as shown in Figure 3.10. Since an increase in the charge states of the plasma can result in increase of magnetic pressure and decrease in field diffusion time, it causes efficient confinement of the plume. This again supports our argument that charge states increase with laser fluence.

3.3.10 Temporal variation of line profiles in the absence and presence of magnetic field

As discussed previously, our spectroscopic study showed the presence of Ba and Ba^+ in the plasma produced. Time resolved spectrum of 455.4 nm line in the absence of magnetic field at different time delays is shown in the Figure 3.11. It
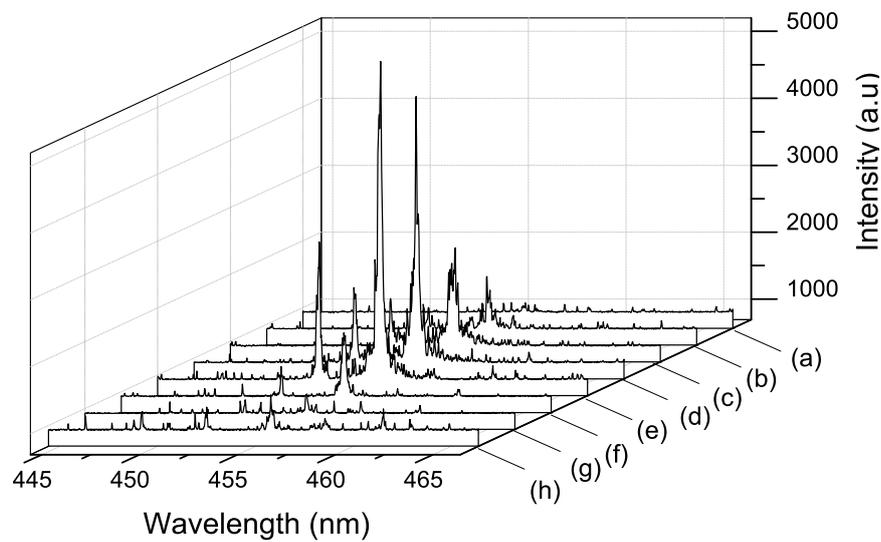
Figure 3.11 Line spectrum of Ba II 455.4 nm in the absence of magnetic field at different time delays. (a) 100 ns (b) 300 ns (c) 600 ns (d) 600 ns (e) 800 ns (f) 1000 ns (g) 1500 ns (h) 2000 ns

is observed from this figure that, the emission intensity increases, reaches maximum at 700 ns time delay and then decreases. Emission intensity is strongly reduced after 1500 ns time delay due to recombination of electrons and ions.

Emission intensity of 455.4 nm line in the presence of magnetic field at different time delays is shown in the Figure 3.12. It is observed from this figure that, the emission intensity increases, reaches maximum at 900 ns time delay and then decreases, almost similar to the case without magnetic field. But, in contrast to

72
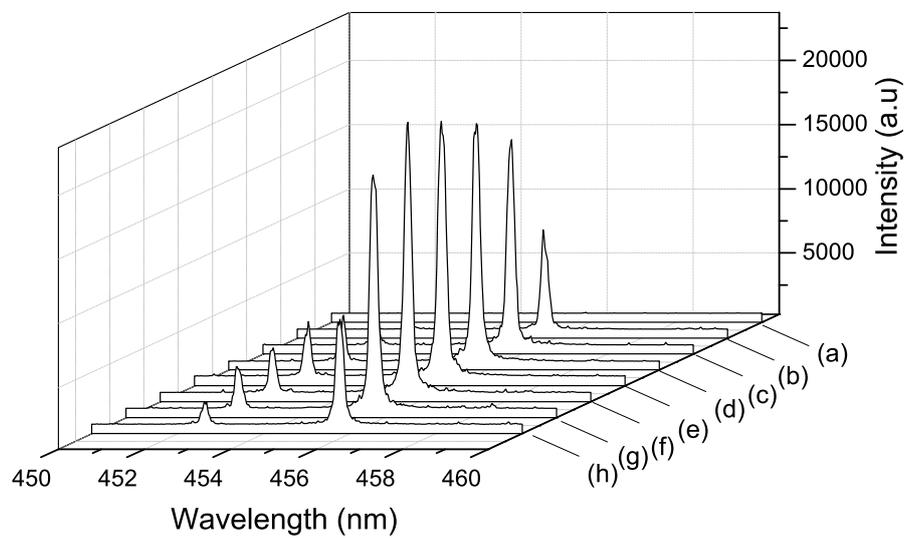
Figure 3.12 Line spectrum of Ba II 455.4 nm in the presence of magnetic
field at different time delays. (a) 100 ns (b) 300 ns (c) 500 ns
(d) 700 ns (e) 800 ns (f) 1000 ns (g) 3000 ns (h) 5000 ns

the case of absence of field, the emission intensity persists up to 5000 ns in presence
of magnetic field. This can be attributed to magnetic confinement. Due to magnetic
confinement, the plume is stopped by the magnetic field and stays for more time,
compared to the case of absence of the field.

3.4   Conclusions

In summary, the effect of 0.45 Tesla magnetic field on the dynamics and spectral behavior of barium plasma has been studied with direct comparison of plume expansion in the absence and presence of the magnetic field. Different plasma parameters such as electron density, electron temperature, magnetic diffusion time are evaluated and correlated to the dynamics of the plume species. The peculiar behaviour shown by the barium plasma in the variation of electron temperature and electron density is attributed to the presence of super elastic collisions. Temporal profiles of neutral and ionic species are fitted with Shifted Maxwell Boltzmann distribution to distinguish the different components present in the profiles. In the presence of the magnetic field, the temporal profiles of neutral lines show three distinct features and became broader and extended up to 5 μs. Based on our experimental observations and available atomic data, we proposed the possible mechanisms for the structured temporal profiles. The observed components in neutral profile are correlated with the populations of the ground state, meta-stable states and long-lived Rydberg states present in the barium plasma. In the case of 455.4 nm ionic line, the profile could be fitted with two SMB components in the absence of field and at large distances from the target surface. The fast component is attributed to the primary ablation process while the slow component corresponds to the formation of ions due to secondary ionization processes during the expansion. Due to the strong confinement of ionic profile in the presence of the magnetic field, ionic profile appears as a single peak structure up to $z = 8$ mm. At higher fluences, the ionic profiles also show efficient confinement in the presence of the magnetic field due to increase of charge states.

CHAPTER 4

EFFECT OF MAGNETIC FIELD ON BARIUM PLASMA EXPANDING IN ARGON AMBIENT

Influence of uniform transverse magnetic field and ambient Ar pressure on the plasma plume produced by Nd:YAG laser ablation of barium has been investigated by using time-of-flight optical emission spectroscopy. The time-of-flight profiles of ions showed ambient pressure independent behaviour at 6 mm distance from the target which is attributed to diamagnetic behavior of laser plasma. A theoretical model is proposed to explain the compression of temporal profiles of the ionic lines. The neutral lines showed a fast peak which is attributed to recombination of singly ionized atoms. The intensity of fast peak is observed to be decreasing with pressure in the absence of field while it is increasing with pressure in the presence of field.

4.1   Introduction

Laser produced plasma in magnetic field has been investigated using various techniques such as optical emission spectroscopy, fast imaging, Langmuir probe, etc. (Harilal et al., 2004; Patel et al., 2013; VanZeeland and Gekelman, 2004). Optical emission spectroscopy and fast imaging were employed to study the dynamics and confinement of laser produced aluminum plasma in 0.64 Tesla magnetic field and found that the plume is not completely stopped at bubble radius and diffused across the magnetic field (Harilal et al., 2004). The expansion dynamics and optical emission characteristics of the laser ablated brass plasma in a non-uniform magnetic field were correlated to the expulsion of the magnetic field by the laser plasma diamagnetic cavity (Patel et al., 2013). Recent studies have also shown that explosive plasma flow can be converted into a converging flow in presence of magnetic field (Plechaty et al., 2013).

There are several reports on expanding laser produced plasma in vacuum, ambient gas (Geohegan, 1992; Sharma and Thareja, 2004), magnetic field (Shen et al., 2006; Harilal et al., 2006b), as well as magnetic field and ambient gas (Kumar et al., 2011b) using optical emission spectroscopy. Dynamics of laser produced silver plasma expanding in ambient gas was studied using time-of-flight spectroscopy (Issac et al., 1998c). Ambient pressure of oxygen gas has been identified as one of the key parameters in the deposition of ZnO thin films (Thareja et al., 2005). Double peak structure was exhibited by the temporal profiles of different species of plasma expanding in ambient gas (Lv et al., 2004). External magnetic field as well as ambient Ar gas can be used to control the debris mitigation in the laser produced Sn plasma (Harilal et al., 2006a, 2007; Bleiner and Lippert, 2009). Different components in the temporal profiles of neutral and ionic species in the expanding plasma in presence of ambient gas and magnetic field are analyzed by fitting Shifted Maxwell Boltzmann (SMB) distribution (Bulgakova et al., 2000). The present study helps to understand the dynamics of ionic as well as neutral species in the expanding plasma plume in the presence of magnetic field and its response to various ambient pressures. In the present study, we report the compression and pressure independent behaviour of ionic species in presence of magnetic field and ambient gas using the time-of-flight spectroscopy.

4.2 Experimental Setup

Experimental setup for the present experiments is discussed in detail in Chapter 2. Some of the important features are discussed here. The plasma plume was generated inside a multi-port stainless steel chamber which was evacuated to a base pressure better than 5×10^{-5} Torr (Raju et al., 2014) using the fundamental wavelength of a 1.6 J Nd:YAG laser having 8 ns pulse width. An 18 mm diameter solid barium rod, purity better than 99 % was used as the target and was mounted on a movable target holder through vacuum compatible feed-through for fresh positioning of the target after exposure to the laser beam. The spot size of the laser beam was nearly 1 mm diameter at the target. Experiments were done at various

fluences 12, 18, 24 and $31\ \mathrm{J/cm^2}$ at the target surface by adjusting the laser pulse energy. During the experiment, the chamber was filled with argon gas at different pressures 10^{-2}, 10^{-1}, 1 and 3 Torr. For time and space-resolved spectroscopy, the plasma plume is viewed, using 1:1 imaging optics, normal to the direction of expansion and was imaged at the entrance slit of a 0.35 meter monochromator. By translating the optics system along the direction normal to the target surface, the time of flight profiles were recorded at various distances from the target surface. A uniform magnetic field of 0.45 Tesla in the direction perpendicular to laser plasma expansion was achieved by using a magnetic trap made of two NdFeB permanent magnets separated by 40 mm distance with dimension 76 mm x 76 mm x 38 mm and magnetized in the direction of height.

4.3 Dynamics of Ba II Species

Time of flight studies of two ionic lines in the expanding barium plasma were performed in the absence and presence of the magnetic field, in order to understand the dynamic behavior of the plasma plume across the magnetic field. Temporal profiles of two ionic lines Ba II 413.0 nm (6d $^2\mathrm{D}_{5/2} \rightarrow 6p^2\mathrm{P}_{3/2}$), Ba II 455.4 nm (6p $^2\mathrm{P}_{3/2} \rightarrow 6s\ ^2\mathrm{S}_{1/2}$) were recorded at axial distances of 2 mm, 4 mm, up to 12 mm from the target surface.

4.3.1 Pressure Independent Behaviour

The time of flight profiles of 455.4 nm ionic line in the presence and absence of magnetic field and at various Ar pressures of 10^{-5} to 3 Torr at different distances 4 mm, 6 mm, and 8 mm are shown in Fig. 4.1. At 10^{-5} Torr pressure , temporal profiles are found to have a single peak structure which is significantly broadened, with elongated tail at z = 6 mm and 8 mm from the target surface. The presence of ambient gas completely modified the velocity distributions of the ionic species in the plasma plume. At the intermediate Ar pressures of 10^{-2} and 10^{-1} Torr, the ionic profiles showed two components, designated as 'fast'and 'slow'as observed by several workers(Amoruso et al., 2007; Smijesh and Philip, 2013; Smi-

Figure 4.1 Temporal profiles of Ba II 455.4 nm line in the absence of magnetic field at distances (a) 4 mm (b) 6 mm (c) 8 mm and in the presence of magnetic field at (d) 4 mm (e) 6 mm (f) 8 mm

jesh et al., 2014). It is also observed that, the fast component in case of 10^{-2} and 10^{-1} Torr pressures arrive earlier than the ions recorded at 10^{-5} Torr. Therefore, the origin of fast species in the time-of-flight of ions can be attributed to the emission from recombined Ba^+ which are formed by the recombination of faster Ba^{++} ions with electrons. With an increase in the ambient gas pressure, the collisions between the ions and ambient gas increases, and large time delay is observed for the slow component, whereas the velocity of the fast component is unaffected. These results are in agreement with previous reports on the generation of LPP at larger irradiation fluences (Smijesh and Philip, 2013; Smijesh et al., 2014). With a further increase in

pressure ($> 10^{-1}$ Torr), the interpenetration of the plume species and background gas is very less and the plume species will compress the background gas. The compressed gas restricts expansion of the plume as observed at pressures of 1 and 3 Torr. Barium plasma gets ionized rapidly during the expansion due to super-elastic collisions (Raju et al., 2014) and the ionization attains saturation. Hence enhancement of intensity of ionic emission is not observed with increase in pressure.

On the other hand, overall temporal profiles of ionic lines are compressed significantly in the presence of magnetic field due to the resistive force by the magnetic pressure, in addition to ambient pressure. At 4 mm distance, the fast and slow components are not distinguishable in presence of magnetic field due to magnetic confinement. For distances z ≥ 6 mm, the two components are widely separated in the absence of magnetic field. Hence they are distinguishable even after compression in the presence of magnetic field. Although there is a clear dominance of magnetic confinement, the effect of pressure is also visible at z = 4 mm from the target, where the ionic profiles get delayed with an increase in the ambient pressure (see, Fig. 4.1(d)). Interestingly, the ionic profiles are almost independent of ambient pressure at z = 6 mm where major portion of the profiles are identical and appear at the same time delay for all the considered pressure ranges as shown in Fig. 4.1(e). With further increase of spatial position (z = 8 mm), the effect of pressure start dominating and the slow component experiences a resistive force with increase of ambient pressure as shown in Fig. 4.1(f). The above observations clearly indicate that the effect of magnetic field on the plasma plume increases with spatial position, attains a maximum and then reduces further.

A very similar behaviour is shown by the time of flight profiles of Ba II 413.0 nm line shown in Fig. 4.2. The intensity of fast component 413.0 nm line is less compared to that of 455.4 nm line. The profiles of 413.0 nm are also compressed in presence of magnetic field. At 6 mm distance, the temporal profiles have shown pressure independent behaviour similar to 455.4 nm line. The above observation could be explained on the basis of the diamagnetic behavior of plasma plume and the variation of diamagnetic strength with space and time. In the present
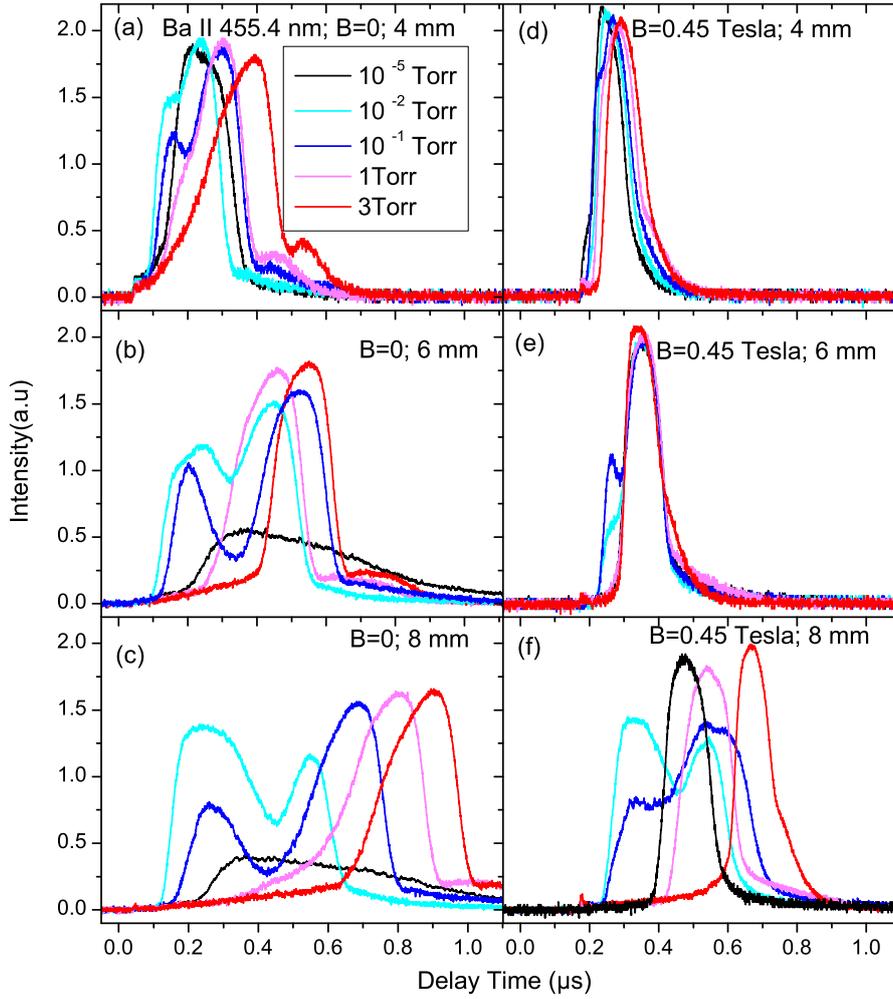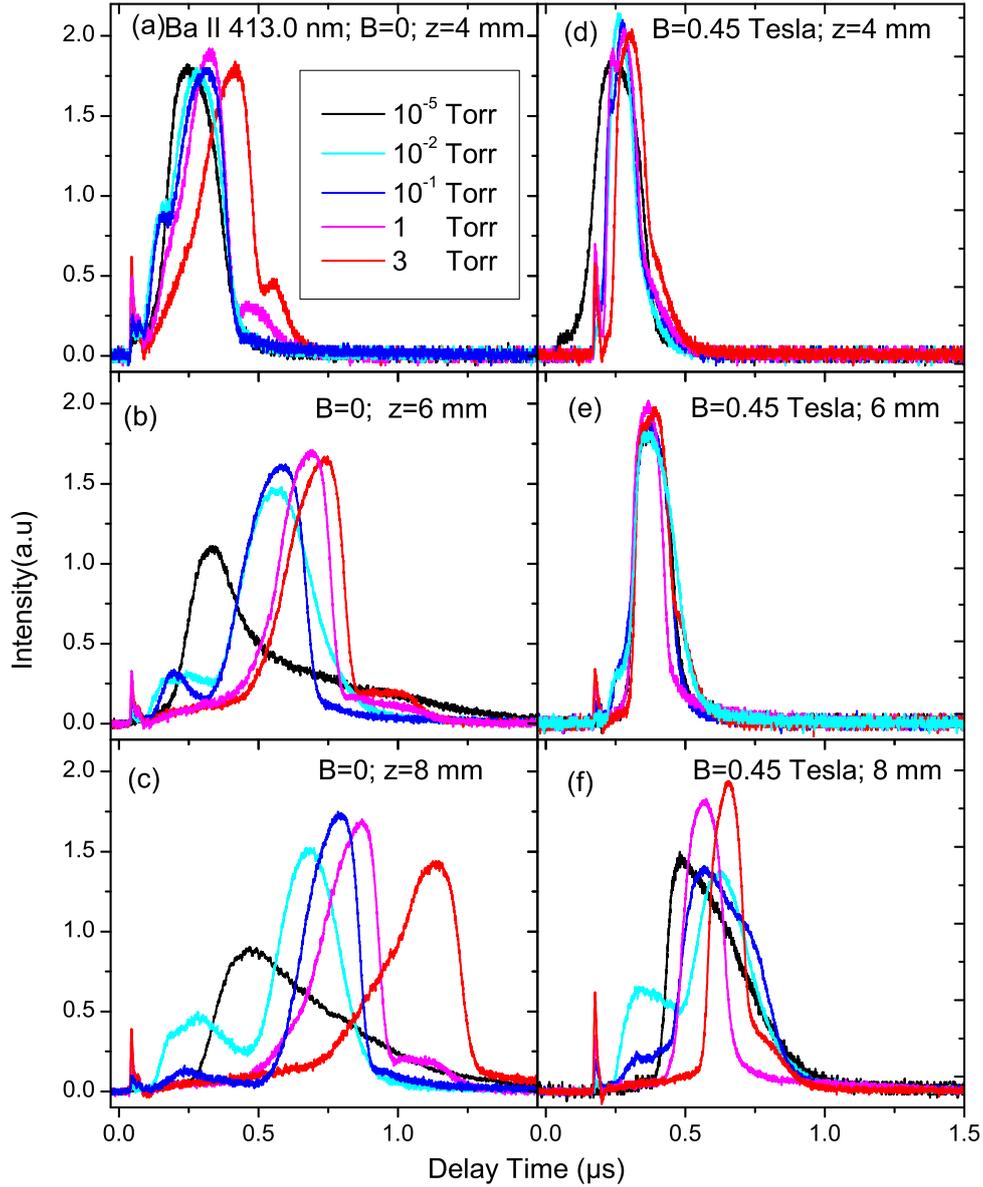
Figure 4.2 Temporal profiles of Ba II 413.0 nm line in the absence of magnetic field at distances (a) 4 mm (b) 6 mm (c) 8 mm and in the presence of magnetic field at (d) 4 mm (e) 6 mm (f) 8 mm

experimental conditions, the estimated Larmor radius and gyro period of ions are nearly 6 mm and 2×10^{-5} s and that of electrons are 0.0003 mm and 1.5×10^{-10} s, respectively. Therefore, the ions are treated as unmagnetized whereas electrons are magnetized (Ganguli et al., 1988). The ions move across the magnetic field while the electrons are captured by the magnetic field and hold the ions back. This generates an electric field pointing radially inward (VanZeeland and Gekelman, 2004)

80

and the $\mathbf{E} \times \mathbf{B}$ drift of electrons, gives rise to a diamagnetic current. Since the induced magnetic field due to the electron drift opposes the applied magnetic field, the plasma behaves as a diamagnetic cavity. The relation between the radius of the diamagnetic cavity and velocity of ions can be derived from the energy balance equation (Collette and Gekelman, 2011)

$$\frac{1}{2}Mv_{\perp}^2(t) + \frac{2\pi B_0^2}{3\mu_0}R^3(t) = U_0 \tag{4.1}$$

where M is the mass of the plasma, $v_{\perp}$ is the velocity of the ions in the direction perpendicular to the external magnetic field B_0, μ_0 is the permeability of free space, R is the cavity radius and U_0 is the initial energy. Previously reported experimental results suggest that the induced magnetic field increases with time, reaches to peak value and decreases after the bubble crossed the probe (Kacenjar et al., 1986). It has been reported that at the bubble radius R_b, where the total excluded magnetic energy becomes equal to the kinetic energy of the plasma, the diamagnetic current is maximum (VanZeeland and Gekelman, 2004). The bubble radius can be written as $R_b = (3\mu_0 E_{lpp}/\pi B_0^2)^{1/3}$ where E_{lpp} is approximated as 1/2 of the initial laser beam energy (Harilal et al., 2004). For laser energy of 150 mJ and a magnetic field of 0.45 T, the estimated bubble radius is nearly 7 mm. In our experiments, we observe that the temporal profiles are identical for all pressures at a distance of 6 mm from the target. This is attributed to the fact that the diamagnetic current reaches a maximum with maximum magnetic pressure, at the bubble radius. The magnetic pressure calculated is approximately 600 Torr for the present magnetic field which is large compared to the ambient pressure (Raju et al., 2014). Hence there is no significant effect of the ambient pressure on the temporal profiles at this distance from the target. Further, the classical magnetic diffusion time is estimated by (Harilal et al., 2004)

$$t_d = \frac{4\pi\sigma R_b^2}{c^2} \tag{4.2}$$

Here c is the speed of light and σ is the plasma conductivity obtained using the

relation (VanZeeland and Gekelman, 2004)

$$\sigma = \frac{50\pi^{1/2}\epsilon_0^2(KT_e)^{3/2}}{m_e^{1/2}e^2Z\ln\Lambda} \tag{4.3}$$

where T_e is the electron temperature, $\ln\Lambda$ is the coulomb logarithm, which can be estimated by (Spitzer, 2013)

$$\ln\Lambda = ln\left[\frac{3}{2}\sqrt{\frac{(KT_e)^3}{\pi n_e}}\frac{1}{Ze^3}\right] \tag{4.4}$$

For Z =1, electron density of 1.5×10^{16} cm^{-3}, and electron temperature of 1 eV, the estimated diffusion time t_d is nearly equal to 300 ns (Raju et al., 2014) which corresponds to a spatial position of 6 mm of ionic species. This means that, at z > 6 mm, diamagnetic property is decreased and magnetic field diffuses into the plasma plume. The significant reduction of retarding magnetic force due to collapse of the diamagnetic cavity in comparison to ambient pressure is clearly observed in Fig. 4.1(f), where the temporal profiles show the usual pressure dependence at z = 8 mm. Temporal delay of ionic profiles with pressure indicates the dominance of ambient pressure over the magnetic pressure. Based on the above analysis, we could say that plume expansion in the presence of magnetic field, both in vacuum as well as at higher ambient pressures clearly shows diamagnetism (Raju et al., 2015).

Further, in order to demonstrate the magnitude and direction of compression of ionic profiles in the presence of the magnetic field, overlapped temporal profiles of Ba II line in the presence and absence of magnetic field at 10^{-5} Torr pressure and at z = 6 mm are shown in Fig. 4.3. It is observed that, the leading portion of the ions experienced a resistive force, whereas the trailing portion gets accelerated in the presence of the field. This shows that the ionic species in the expanding plasma plume are compressed in both directions and confined in small volume in external magnetic field. In order to explain the narrowing down of ionic profile in both the directions, we propose a model similar to that of Kacenjar et al. (1986).This model is based on the distortion of applied magnetic field due to its interaction with the plasma plume. After expansion of a few mm from the target
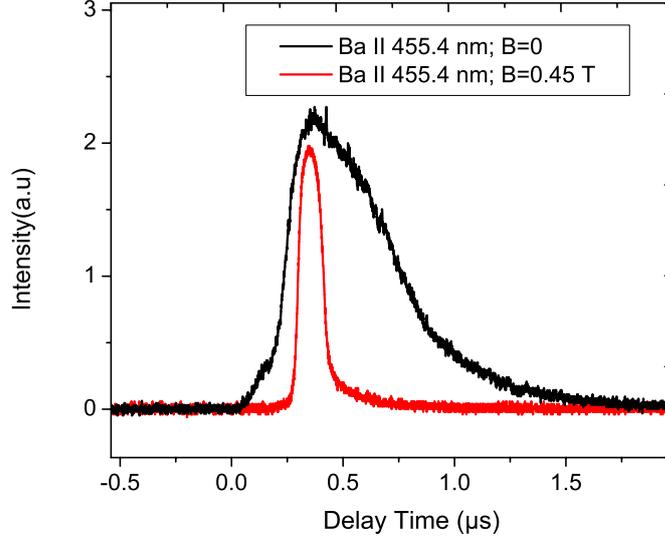
Figure 4.3 Temporal profiles of 455.4 nm line in the absence and presence of 0.45 Tesla magnetic field. For comparison, the intensity of the temporal profile in the absence of the magnetic field is multiplied by 4.

surface, a majority of the ionic species is at the leading edge of the plasma plume and is separated from the target surface. The trailing portion of the plume is mainly dominated by neutrals. This is supported by the temporal profiles of the ionic and neutral species shown in Fig. 4.4. The temporal profiles of Ba I (553.5 nm) and Ba II (455.4 nm) lines in the presence and absence of magnetic field at 10^{-5} Torr and at a distance of 6 mm from the target surface are shown in Fig. 4. It is clearly observed that a majority of fast moving ions are ahead of slow moving neutrals in the presence of magnetic field. Schematic of the distorted magnetic field at the leading portion of the plume is shown in Fig. 4.5. The $\mathbf{J} \times \mathbf{B}$ force due to the induced diamagnetic current on the plasma can be written as (Bellan, 2006),

$$\boldsymbol{J} \times \boldsymbol{B} = \frac{1}{\mu_0} \left[-\nabla_\perp \left(\frac{B^2}{2} \right) + B^2 \boldsymbol{\kappa} \right] \qquad (4.5)$$

where $\mathbf{B}$ is the total magnetic field and $\mathbf{J}$ is the current density due to $\mathbf{E} \times \mathbf{B}$ drift and $\boldsymbol{\kappa}$ is a measure of curvature of the magnetic field at a selected point on a field line which is given by $\boldsymbol{\kappa} = \hat{B}.\nabla\hat{B}$. Here the first term on the right hand side denotes

83
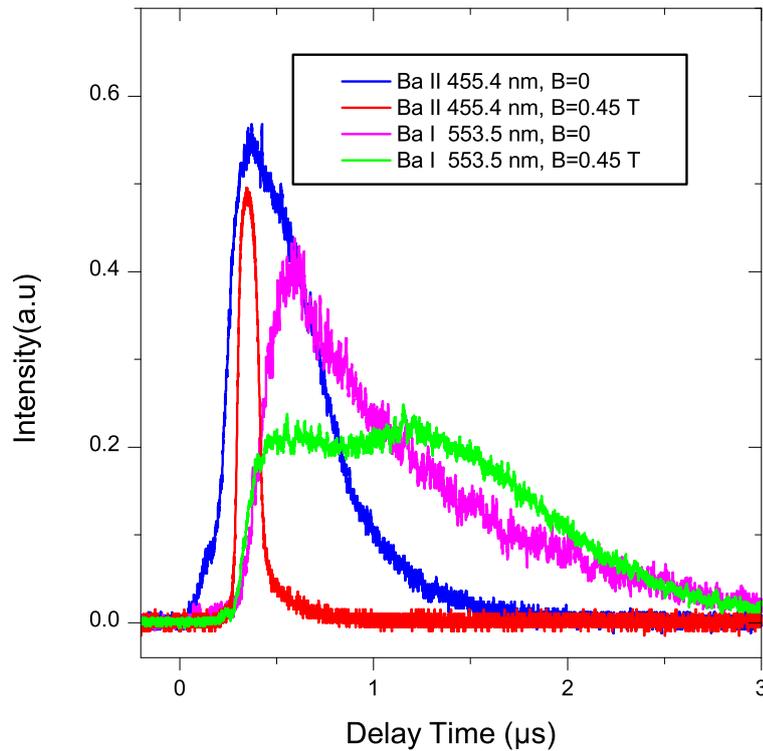
Figure 4.4 Temporal profiles of Ba I 553.5 nm and Ba II 455.4 nm lines at
z = 6 mm in 10^{-5} Torr pressure in the absence and presence of
magnetic field. For comparison, the intensity of the ionic line in
magnetic field is divided by 4.

the magnetic pressure, which is giving different acceleration and decelerations of
plasma while the second term describes a force that tends to straighten out magnetic curvature. As shown in Fig. 4.5, at the front of the plasma, the perpendicular
field gradient is in the direction of plasma expansion and magnetic force is in the
opposite direction which decelerates the ions. Whereas in the case of trailing ions,
the magnetic force is in the plasma expansion direction and it accelerates the ions.
Thus, the geometry of the self-generated magnetic field is giving rise to the acceleration and deceleration mechanisms of ions in the plasma. Due to the deceleration
of the leading ions and the acceleration of the trailing ions, the temporal profile gets
narrowed down. This effect is more pronounced at z = 6 mm where the diamag-
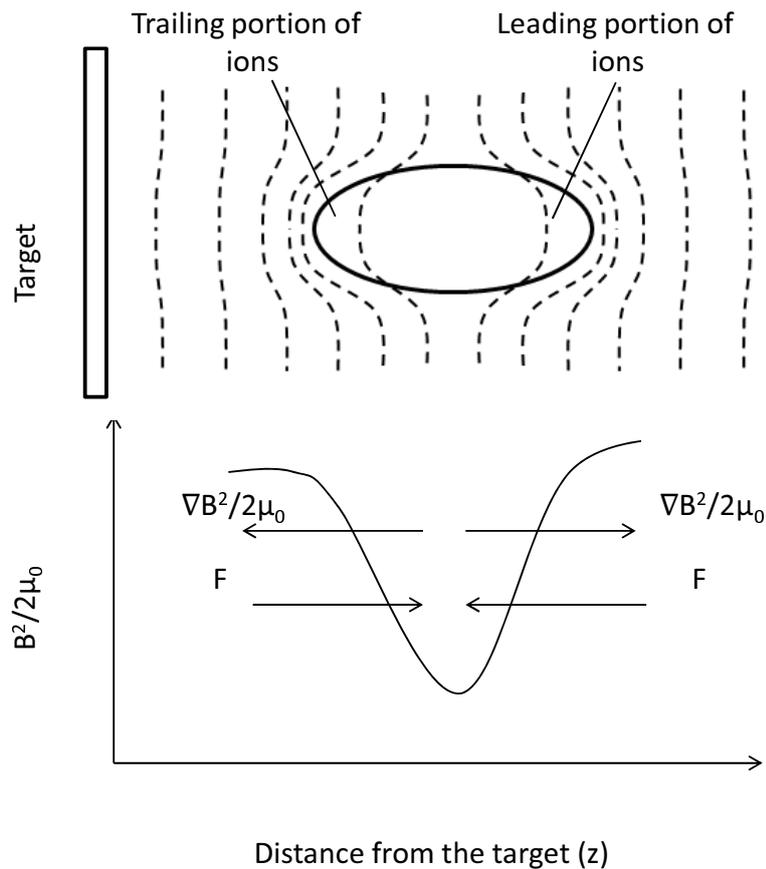
Figure 4.5 Schematic of the resultant magnetic field and magnetic force on
the laser plasma diamagnetic cavity

netic property reaches the maximum and the temporal profile is narrowed down as observed in Fig. 4.1(e).

4.3.2 Shifted Maxwell Boltzmann (SMB) Distribution of Fast and Slow Peaks

The temporal profiles of ionic line 455.4 nm at different pressures in the absence and presence of magnetic field are fitted with multi-SMB distribution and shown in Fig. 4.6. It is observed that at 10^{-5} Torr pressure, the temporal profiles could be fitted with single component in the absence as well as presence of magnetic field. As the pressure increases, at 10^{-1} Torr, the profile could only be fitted with two components as shown in the figure. Both the fast and slow components are
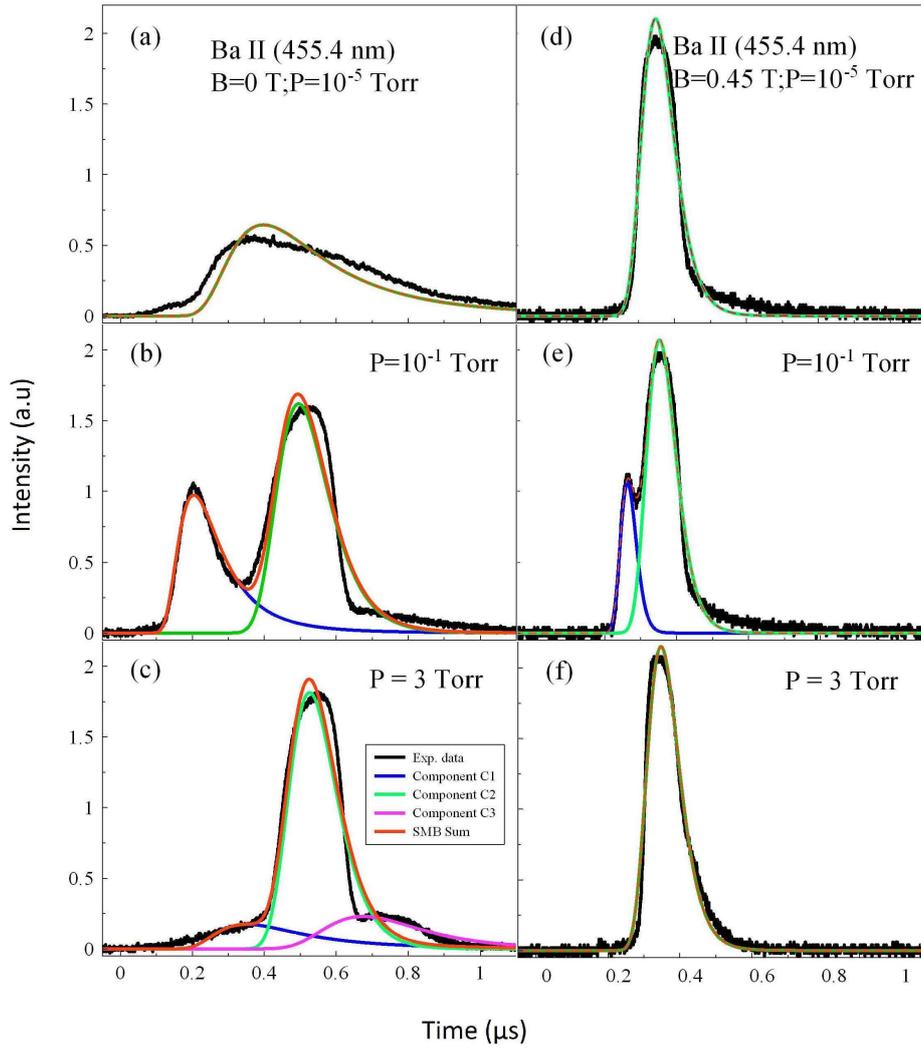
Figure 4.6 SMB fitting of different components of 455.4 nm ionic line at different pressures (a) 10^{-5} (b) 10^{-1} (c) 3 Torr in the absence of magnetic field; (d) 10^{-5} (e) 10^{-1} (f) 3 Torr in the presence of magnetic field

compressed considerably in presence of magnetic field. The fast component in this regime is attributed to recombination of Ba^{2+} with electrons as discussed in section 4.3.1. As the pressure is increased, at 3 Torr pressure, the interpenetration of the plume species and background gas is very less so that the intensity of the fast component is also reduced considerably. In presence of magnetic field, magnetic pressure also acts on the plasma plume in addition to the ambient pressure so that the fast component is absent at 3 Torr pressure. Also, one more delayed component

is observed in the temporal profile in the absence of magnetic field which may be due to increased collisions in the higher pressure regime.

4.3.3 Integrated Emission Intensity

Fig. 4.7 shows the variation of intensity of ionic lines at different pressures at 6 mm distance from the target surface. It is observed that in the absence of
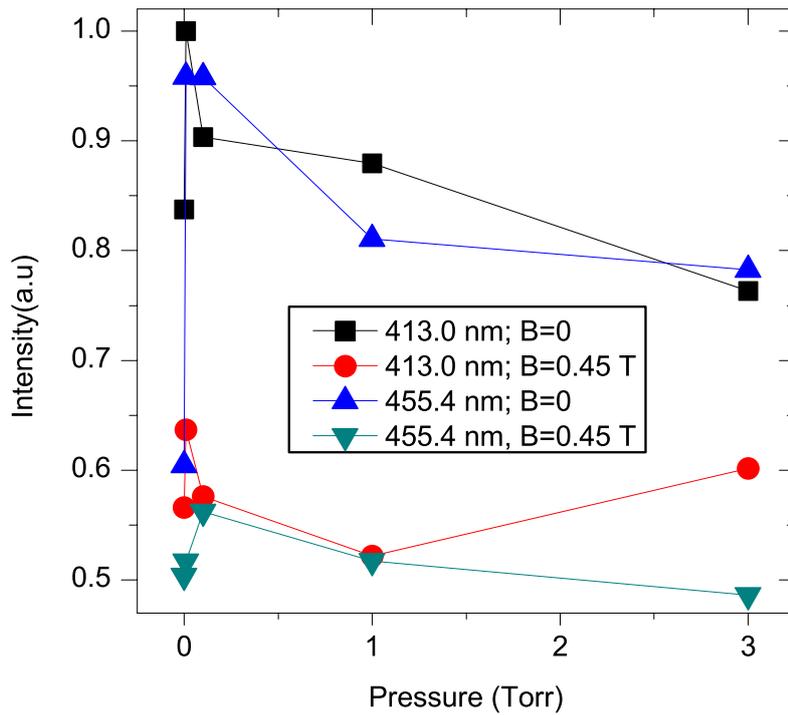
Figure 4.7 Integrated Intensity of ionic lines at 6 mm distance from the target at different pressures

magnetic field, the intensity is increasing upto 10^{-1} Torr and then decreases. But in presence of magnetic field, there is no appreaciable change in the intensity with pressure. This is because of the pressure independent behaviour of the ionic profiles. As explained in the Section. 4.3.1, the ionic profiles are compressed and identical in presence of magnetic field. The peak intensity of the profiles is also almost same for the considered pressures in the presence of magnetic field so that there is no much variation in the integrated intensity.

4.3.4 Effect of Fluence

Fig. 4.8 shows the time of flight profiles of Ba II 413.0 nm line at different laser fluences at a distance of 6 mm from the target surface at 10^{-1} Torr pressure. In
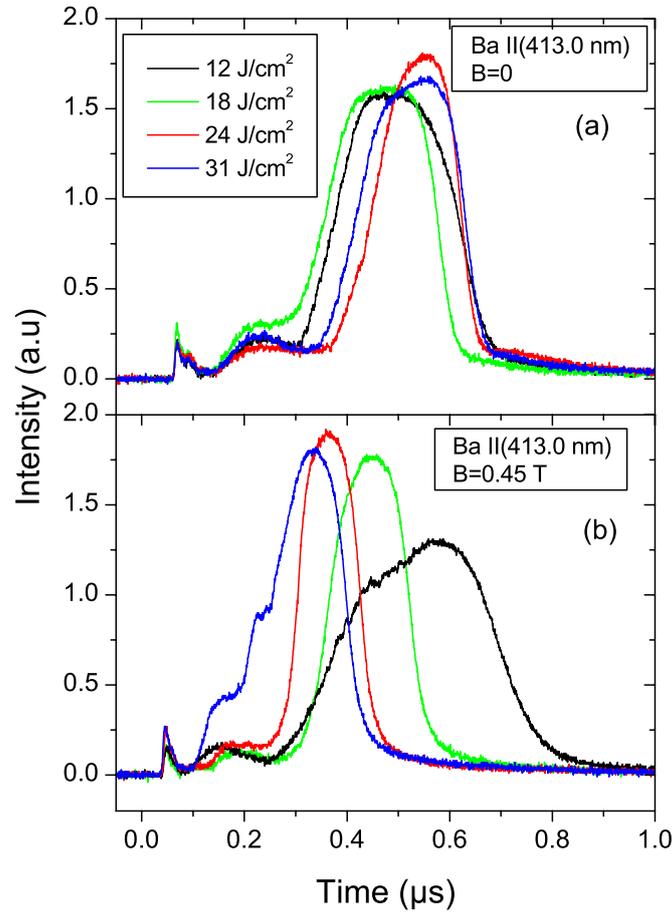
Figure 4.8 Time of flight profiles of Ba II (413.0 nm) line at different laser fluences for distance 6 mm from the target surface in the absence and presence of of 0.45 T magnetic field at 10^{-1} Torr pressure

the absence of magnetic field, the profiles showed two components apart from the structures appearing due to Bremsstrahlung. The fast component, as explained earlier, may be due the recombination of Ba III with electrons. It is worth to mention here that two of Ba III lines 637.7 nm and 638.3 nm appeared in the emission spectrum recorded from   the plasma at 300 ns time delay which is equal to the time of arrival of the fast component. It is observed that the peak velocity calculated

from the temporal profile is not changing and the profile shows confinement at higher fluence.

Similar to the case of absence of field, the profiles showed double peak structure in the presence of magnetic field. But in contrary, the arrival time of the slow component of the profile decreased with fluence which shows an increase in the velocity of the slow component of ionic species. There is no change in the velocity of the fast component. The temporal profiles narrowed down with increase in fluence which showed efficient confinement of ionic species at higher fluence in presence of magnetic field. It is also observed that at higher fluence, in presence of magnetic field, the fast component itself is divided into two components.

4.4 Dynamics of Ba I Species

4.4.1 Spatial Evolution of Temporal Profiles

Temporal profiles of two spectral lines from neutral barium Ba I 553.5 nm $(6s6p\,^1P_1 \rightarrow 6s^2\,^1S_0)$, Ba I 577.7 nm $(6s6d\,^3D_3 \rightarrow 6s6p\,^3P_2)$ were recorded at axial distances of 2 mm, 4 mm, up to 12 mm from the target surface in the absence and presence of magnetic field at various Ar pressures from 10^{-5} to 3 Torr and shown in Fig. 4.9. In the absence of magnetic field, it is observed that, at 4 mm distance which is nearer to the target, the profiles are showing a fast component that may be due to the recombination of Ba^+ ions with electrons as explained earlier. The intensity of fast component is very less compared to the slow component and it decreases with distance. The intensity of slow component increases with Ar pressure while the intensity of fast component decreases. At distances nearer to the target, the intensity does not change much with pressure, while at distances greater than 4 mm, the intensity is found to increase with pressure.

Even in the presence of magnetic field, the profiles have two components, fast and slow. The intensity of the slow component is increasing with
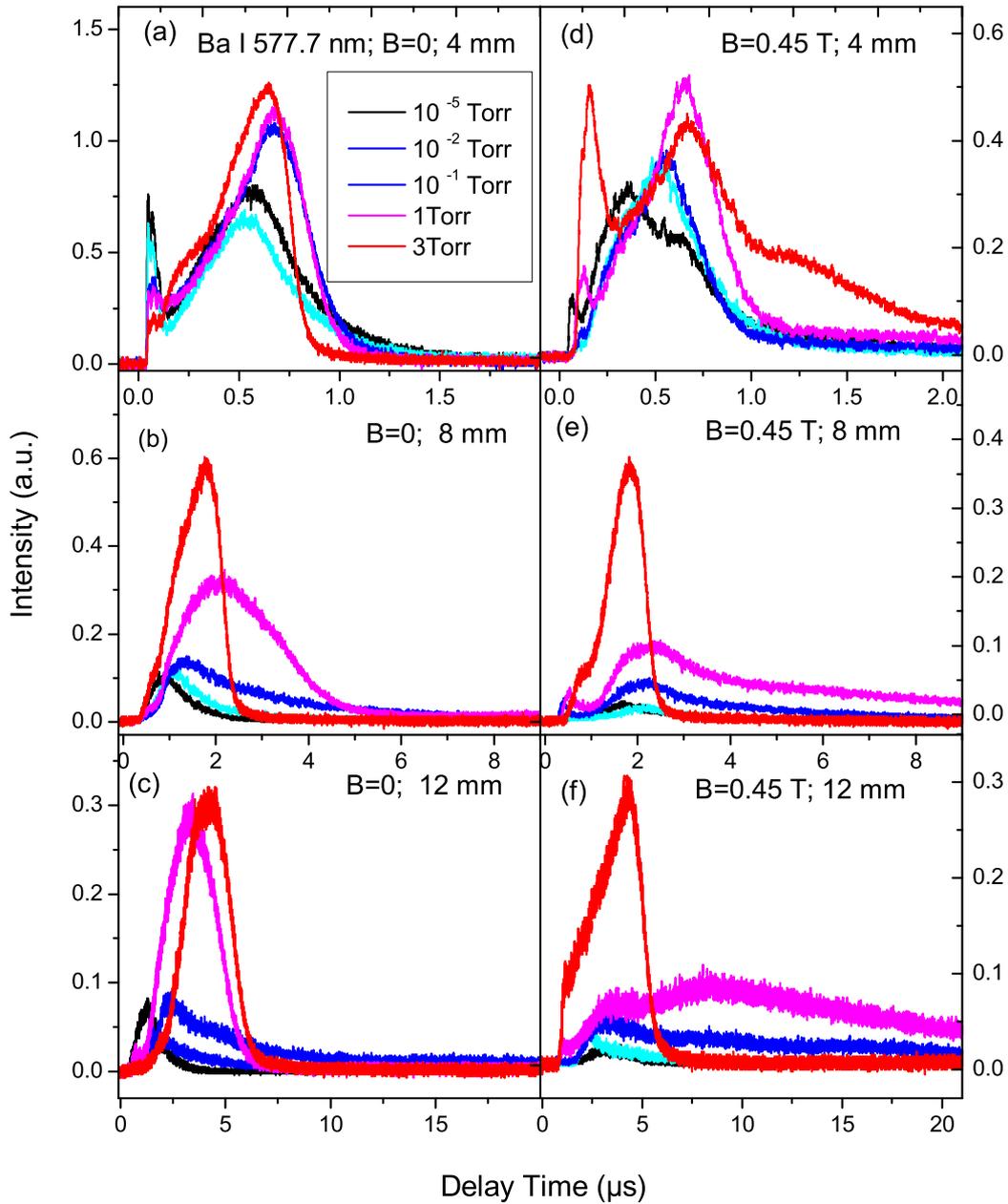
Figure 4.9 Temporal profiles of Ba I 577.7 nm line at various Ar pressures at (a) 4 mm (b) 8 mm (c) 12 mm in the absence of magnetic field and (d) 4 mm (e) 8 mm (c) 12 mm in the presence of magnetic field

pressure as in the case of absence of magnetic field. In contrast to the observation in the absence of magnetic field, the intensity of fast component is also increasing with pressure. In the presence of magnetic field, this neutral line is temporally broadened

up to 20 μs at 1 Torr pressure, which is large compared to that of absence of field. When the pressure is increased to 3 Torr, there is no change in the temporal width of the profile in the absence and presence of magnetic field.

4.4.2 Pressure Dependence of Temporal Profiles

Two neutral lines 553.5 nm and 577.7 nm in the absence and presence of the magnetic field are compared at three different pressures 10^{-5} Torr, 10^{-1} Torr and 3 Torr of Ar ambient and shown in the Fig.4.10. Here 553.5 nm (6s6p $^1P_1 \rightarrow$ $6s^2$ $^1S_0$) is a transition to the ground state while 577.7 nm (6s6d $^3D_3 \rightarrow 6s6p$ $^3P_2$) is a transition to an excited state. In vacuum, the neutral profile could be fitted with two SMB components as discussed in Chapter 3. The profiles are broadened in presence of magnetic field compared to the absence of magnetic field in vacuum due to magnetic confinement (Raju et al., 2014). The plasma plume experience a resistive force in presence of magnetic field and confined in a small volume. The magnetic confinement increases collisions among the plume species and transfers atoms to the metastable sates (Raju et al., 2014) and results in the broadening of the temporal profile. It is observed that the profiles are broadened at 10^{-1} Torr pressure compared to vacuum in the absence as well as presence of magnetic field. This may be due to the thermalization of neutral species because of the collisions with the ambient gas. The neutral profiles showed a broadening up to 4 μs at this pressure.

When the pressure is increased to 3 Torr, the temporal broadening of 553.5 nm line is decreased compared to 10^{-1} Torr pressure while there is no change in the broadening of 577.7 nm line which is a transition to an excited state. In the presence of magnetic field, there is no much difference between the temporal broadening of these lines. The difference in the broadenings of the temporal profiles of these lines can be understood better by fitting those profiles with multi-SMB distribution. Fig 4.11 shows the temporal profiles of these two lines at 3 Torr pressure in the absence of magnetic field. It is observed that both the profiles could be fitted with two SMB components. The origin of the fast component is due to the formation of neutrals due to direct ablation and radiative cascade. The slow component is due to
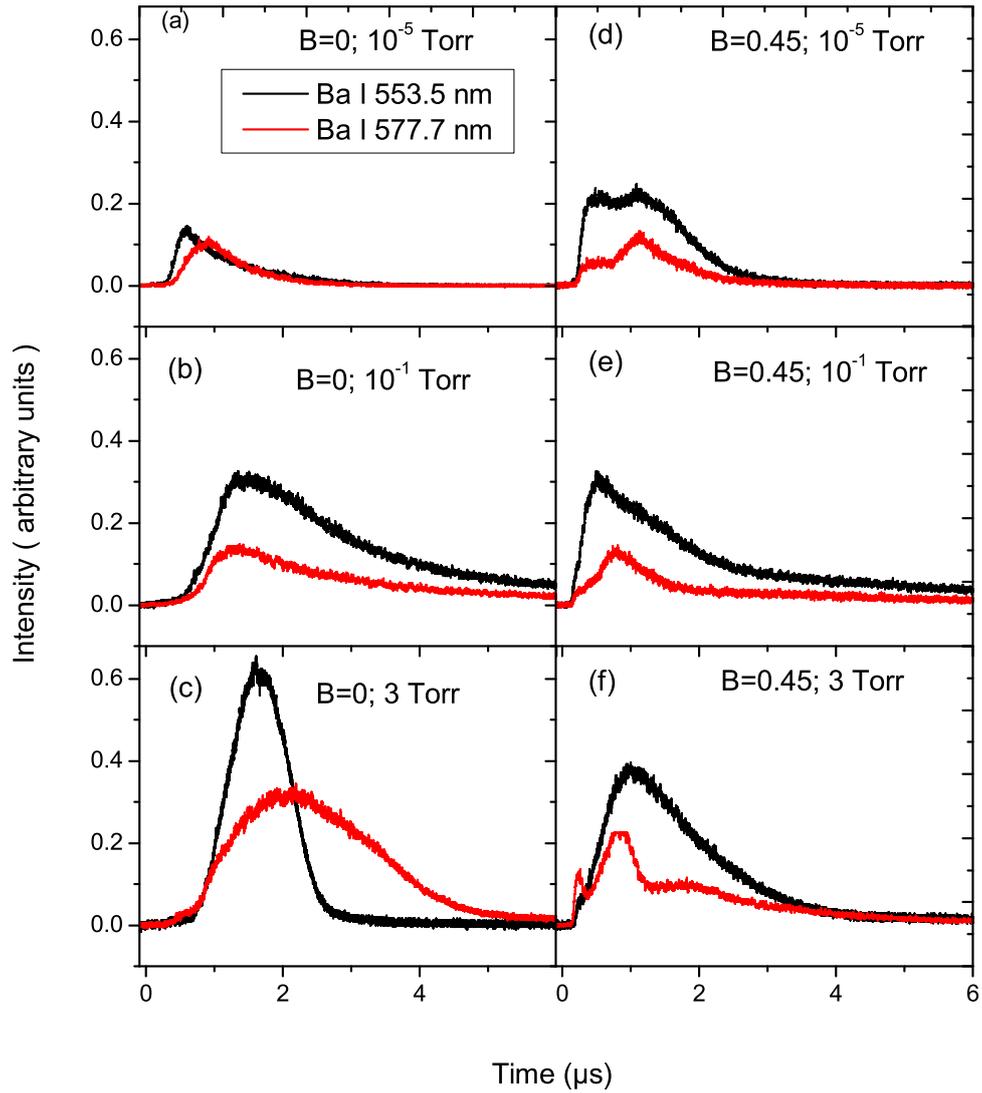
Figure 4.10 Time of flight profiles of 553.5 nm and 577.7 nm neutral lines in the absence and presence of magnetic field (a) 10^{-5} Torr (b) 10^{-1} Torr (c) 3 Torr and in the presence of magnetic field (d) 10^{-5} Torr (e) 10^{-1} Torr (f) 3 Torr

the collisional processes and metastable states. It is observed that the fast component of both the lines is having almost same broadening while the slow component is having larger temporal broadening for 577.7 nm line compared to 553.5 nm line. This indicates that the temperature of the species forming the slow component of 577.7 nm is more compared to that of 553.5 nm line. This may be because 553.5 nm line is a transition to ground state while 577.7 nm line is transition to an excited state. In the presence of magnetic field, the plasma gets thermalized due to increased
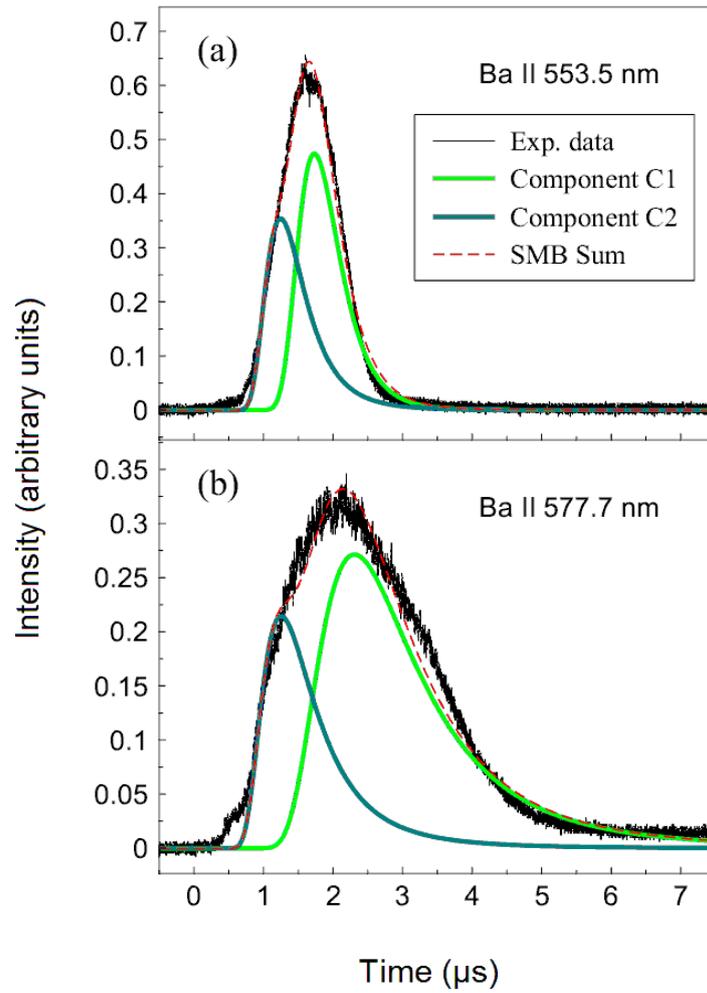
Figure 4.11 Time of flight profiles of (a) 553.5 nm and (b) 577.7 nm neutral
lines in the absence of magnetic field at 3 Torr pressure

collisions among the plume species. So, no difference in temporal broadenings is
observed (Kumar et al., 2008).

4.4.3 Effect of fluence

The effect of fluence has been studied on the temporal profiles of neutral
lines 553.5 nm and 577.7 nm at four different fluence values 12 to 31 J/cm^2. Fig.
4.12 shows the effect of fluence on the 553.5 nm neutral line. In the absence of
magnetic field, the velocity is increasing with fluence. It is observed that the emis-
sion intensity is increasing at the initial time delays while there is no much change
in the emission intensity in the delayed part of the temporal profile. The intensity

93
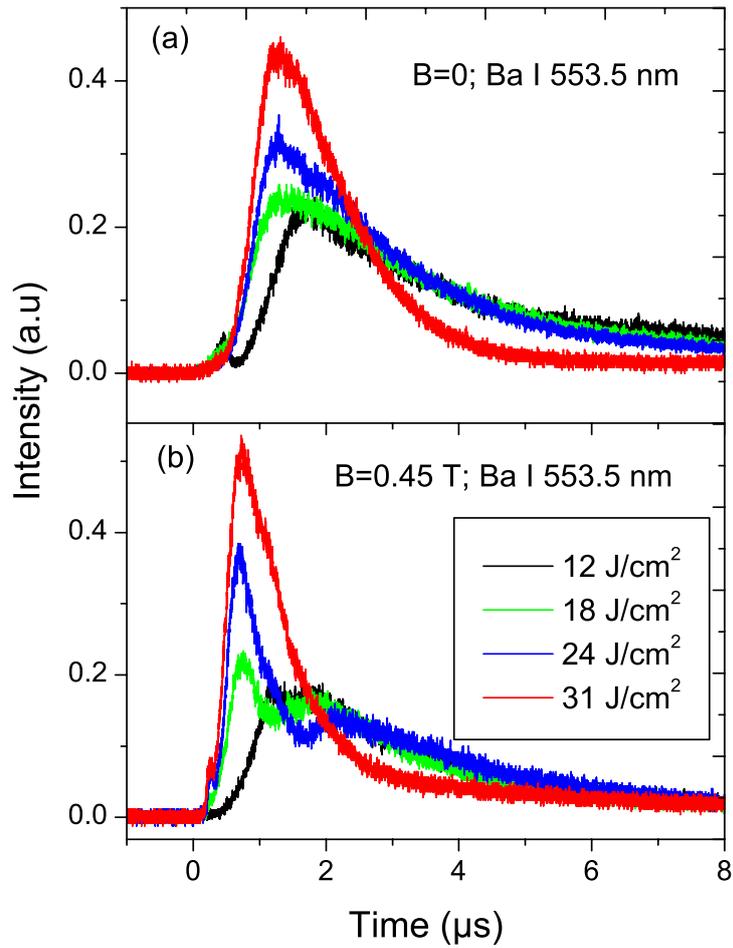
Figure 4.12 Time of flight profiles of Ba I (553.5 nm) line at different laser
fluences for distance 6 mm from the target surface in the ab-
sence and presence of 0.45 T magnetic field at 10^{-1} Torr pres-
sure

of delayed part of the profile is decreased at the fluence 31 $\mathrm{J/cm^2}$.

In the presence of magnetic field, temporal profiles have two peak struc-
ture shown in the Fig. 4.12 (b). There is no much change in the peak velocity of the
fast component while the velocity corresponding to slow peak is increased. It is ob-
served that, at 31 $\mathrm{J/cm^2}$ fluence, the intensity of delayed component is decreasing,
similar to absence of field case.

4.4.4 Integrated Emission Intensity

Fig. 4.13 shows the variation of intensity of neutral lines at different pressures. It is observed that in the absence and presence of magnetic field, the intensity
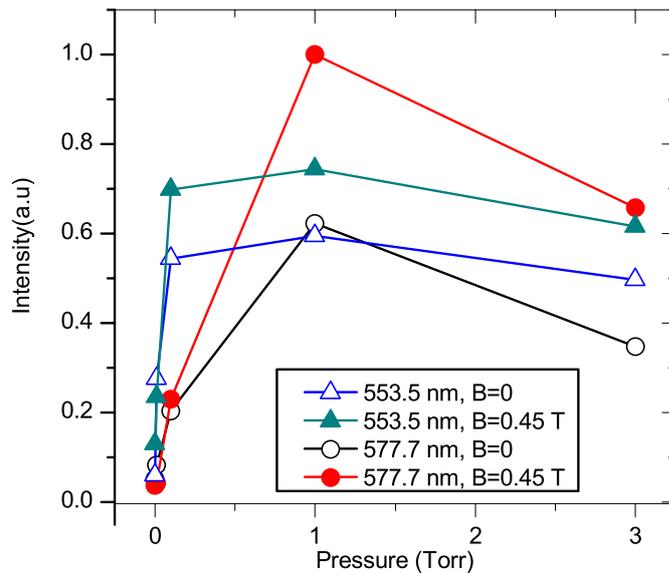
Figure 4.13 Intensity of neutral lines at 6 mm distance form the target at different pressures

of both the neutral lines increases upto 1 Torr pressure. The increase of ambient pressure enhances the collissions of plasma species with the ambient gas so that the intensity increases at the higher pressure. When the pressure is increased to 3 Torr, the integrated intensity is decreasing. This is because of confinement of the plume instead of penetration of the plasma plume into the ambient gas.

4.4.5 Comparison of Temporal Profiles of Ba I and B II

The profiles of neutral line 577.7 nm and ionic line 413.0 nm in the absence of magnetic field at 10^{-1} Torr pressure are shown in the Fig 4.14. Since the intensity of neutral line is very less compared to ionic line, the intensity of neutral line is multiplied by a factor of 45 for comparison. The temporal profiles of neutral and ionic profiles showed multiple peak structure as shown in the figure. A four
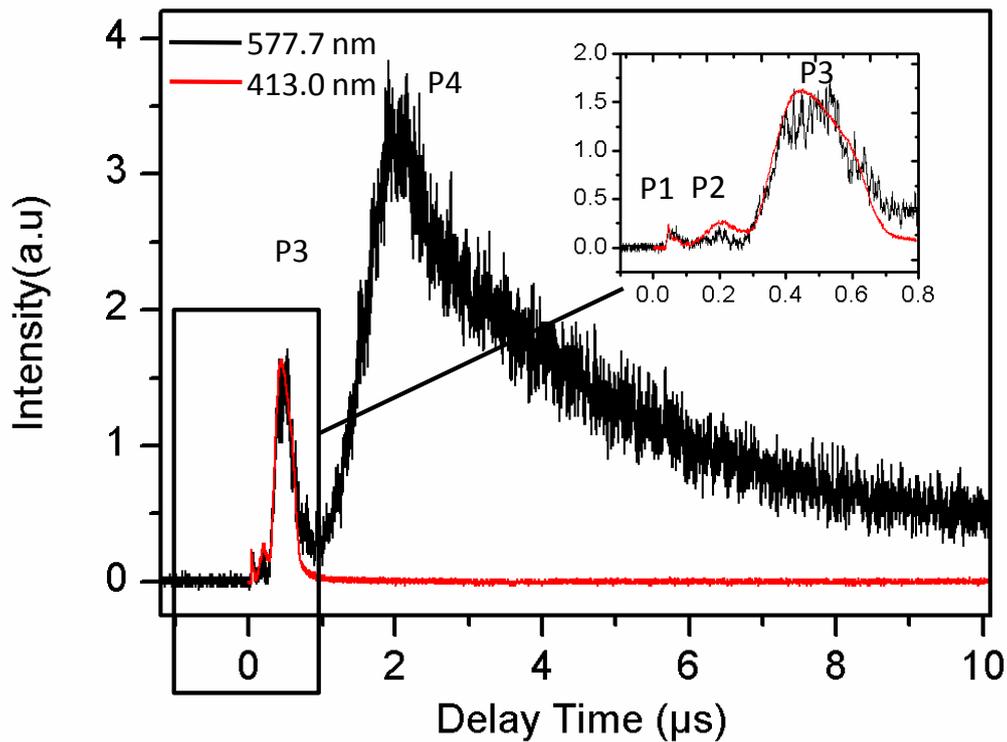
Figure 4.14 Comparision of neutral line Ba I 577.7 nm and ionic line Ba II 413.0 nm at 10^{-1} Torr pressure

peak structure is observed for neutrals and a three peak structure is observed for ions. These peaks are denoted by P1, P2, P3 and P4 where P1 denotes the fastest peak and P4 denotes the slowest one. The first three peaks of the neutrals and ions are appearing at the same time delay as shown in the figure. The first peak appeared immediately after the formation of the plasma and can be due to the prompt electrons (Issac et al., 1998a,b). The prompt electrons having high kinetic energies are generated by the interaction of the laser pulse with the target. The emission from the excited argon gas by the prompt electrons may be giving rise to the peak P1. The second peak of the ions can be attributed to recombination of Ba^{2+} with electrons. A fraction of these Ba^+ ions may again recombine with electrons to form the peak P2 of the neutrals. The component P3 in ionic profile denotes the directly formed ions due to laser ablation as well as other collissional processes. The peak P3 of the neutrals may be due to the recombination of directly formed Ba^+ ions with the electrons. The neutrals formed in the process of direct laser ablation may be appearing as the fourth peak P4.

96

4.5 Conclusions

In summary, the effect of magnetic field and Ar ambient gas on the expanding barium plasma has been investigated by using time-of-flight spectroscopy. It is observed that the ionic profiles are compressed in presence of magnetic field. The pressure independent behaviour shown by the ionic profiles at 6 mm distance from the target surface is attributed to plasma expansion as a diamagnetic cavity. Temporal profiles of ions are analysed by fitting with Shifted Maxwell Boltzmann (SMB) distribution. A fast peak is shown by neutral profiles whose intensity is decreasing with pressure in the absence of magnetic field where as its intensity is increasing in presence of magnetic field. The different temporal broadenings shown by the two neutral lines in higher pressure is attributed to the difference in their spectroscopic transitions to ground and excited states.

CHAPTER 5

FAST IMAGING OF TUNGSTEN AND BARIUM PLASMAS

Effect of uniform magnetic fields of different strengths on tungsten and barium plasmas has been investigated using fast-imaging. Field aligned striations are observed in the presence of magnetic field at very low pressure of 10^{-5} Torr. These striations are investigated at different magnetic fields. The plasma shows a sharpening feature at 10^{-1} Torr pressure which is attributed to Laser Supported Detonation (LSD) wave. At higher pressures of 1 Torr and 3 Torr, plasma shows hydrodynamic instability which is attributed to R-T instability.

5.1   Introduction

Fast imaging is an experimental technique of capturing integrated emission over a range of wavelengths from an expanding plasma plume using an ICCD with gate widths in nano-second and pico-second regime. This diagnostic can be used to study the effect of ambient pressure on laser produced plasma (George et al., 2009; Harilal et al., 2002; Amoruso et al., 2006; Geohegan and Puretzky, 1995), hydrodynamic expansion features like plume splitting and formation of lobes (Harilal et al., 2005b, 2012; Raju et al., 2011), study of colliding plasmas (Singh et al., 2013; Gambino et al., 2013), to find the effect of magnetic field on the laser produced plasma (Harilal et al., 2004; Kim et al., 2007), etc.

The expansion dynamics of laser produced plasmas are strongly influenced by the presence of magnetic field. There are several investigations on the classical phenomenon of laser produced plasma expansions such as plume splitting, oscillations of the plume, rotation of the plasmoids, etc. Study of the plasma in external magnetic field showed plasma expansion velocity is more in the direction of magnetic field, while expansion is impeded in the transverse direction; whereas in the

99

absence of magnetic field, plume showed linear expansion (Harilal et al., 2004). It has been observed that presence of non-uniform magnetic field can cause oscillations of the expanding plasma (Neogi and Thareja, 1999). Detailed investigation in presence of magnetic field showed that, the neutral species in the plasma formed two lobes near the magnetic poles while the ionic species showed splitting into slow and fast components (Kim et al., 2007). Copper plasmoid showed rotation in presence of non-uniform magnetic field which was attributed to torque acting on the plasmoid because of the $\mathbf{J} \times \mathbf{B}$ force (Pandey and Thareja, 2013).

Instabilities in laser produced plasma are also observed in the presence of magnetic field. Flute instability was observed in Al targets in presence of 1 Tesla magnetic field and was attributed to large larmor radius R-T instability (Ripin et al., 1987). Instability shown by barium plasma in presence of magnetic field was identified as electron-ion hybrid velocity-shear instability (Mostovych et al., 1989). Dynamics of plasma produced from glass target was studied in the presence of different magnetic fields and undulations were observed in the plasma due to large larmor radius Kevlin-Helmholtz instability (Peyser et al., 1992).

In this work, we have studied the dynamics of laser produced tungsten as well as barium plasmas in the absence and presence of magnetic field and Ar ambient. Tungsten is used as a wall material in International Thermonuclear Experimental Reactor (ITER) tokamak and can be used for the diagnostics of magnetically confined plasma (Matthews et al., 2007) while barium is an important element in the study of space plasmas (Kelley and Livingston, 2003; Zakharov, 2002). In the present study, we report the field aligned striations at a laser fluence of 10^9 W/cm^2 which is very nearer to the threshold for producing laser produced plasmas where as these kind of reports are limited to high fluence ($10^{12} - 10^{13}$ W/cm^2) in the literature (Peyser et al., 1992; Mostovych et al., 1989). Field aligned striations have been investigated in the presence of different magnetic fields.

5.2 Experimental Setup

Experimental setup for the present studies is discussed in detail in Chapter 2. The plasma plume was generated inside a multi-port stainless steel chamber, which was evacuated to a base pressure better than 5×10^{-5} Torr, using the fundamental wavelength of a 1.6 J Nd:YAG laser having 8 ns pulse width. Barium (99 % purity, Good Fellow) cylindrical rod of 18 mm diameter and tungsten (99 % purity, Plancee) plate of 1 mm thickness were used as target materials. The laser was focussed to a spot of diameter nearly 1 mm. Fluence was kept as 18 J/cm^2 at the target surface by adjusting operating parameters of the laser. During the experiment, the chamber was filled with argon gas at different pressures 10^{-5}, 10^{-1} and 3 Torr. Magnetic trap was made of two NdFeB magnets of size 76 x 76 x 38 mm^3 and uniform magnetic fields of different strengths 0.3, 0.45 and 0.52 Tesla were realized by a changing the separation between the two magnets.

5.3 Imaging of Expanding Tungsten Plasma

Expanding tungsten plasma is studied by using fast imaging in various magnetic fields (0.3, 0.45, 0.52 Tesla) and ambient pressures of Ar ($10^{-5}, 10^{-1}, 3$ Torr). Gate width of the ICCD was set to 5 ns while recording these images. Images are recorded at different time delays from 100 ns, upto a time delay when the plasma disappeared.

5.3.1 10^{-5} Torr Ambient Pressure

Two dimensional photographs of plasma expansion at different time delays from the laser pulse irradiation in the absence and presence of the 0.3 Tesla magnetic field at 10^{-5} Torr pressure are shown in Fig. 5.1. In the absence of magnetic field, the structure of the plume is hemispherical as expected (Singh and Narayan, 1990; Harilal et al., 2004). The plume dynamics are observed to be significantly different in the presence of magnetic field compared to that in the absence of magnetic field. The plume front of the plasma is observed to be sharp due to the magnetic pressure.

The expanding plasma in an external magnetic field experiences a deceleration due to the magnetic pressure and comes to a stop when the plasma pressure equals the magnetic pressure. In other words, plasma expansion ceases when $\beta = 1$, where β = plasma pressure/magnetic pressure (Kacenjar et al., 1986). The restriction of plasma expansion due to magnetic pressure is clearly observed in Fig. 5.1 where the plume front is flattened compared to that observed in the field free case. The emission intensity of plasma increases in the presence of magnetic field. At a time delay of 1000 ns, irregularities originate at the plume boundary and develop into field aligned striations within the plume at higher time delays. These striations have well defined intensity pattern along the field direction.

In order to carry out further investigation of these field aligned striations in presence of magnetic field, we have recorded the images of plasma in three different magnetic fields of 0.3, 0.45 and 0.52 Tesla and are shown in Fig. 5.2. The plume shape is not spherical in presence of magnetic field. In the case of lowest magnetic field of 0.3 Tesla, small irregularities appeared on the plasma boundary at 1000 ns time delay as shown in Fig. 5.2. The separation between two successive intensity patterns, known as wavelength of striations is observed to be 2 mm. At 1200 ns time delay, field aligned striations are clearly visible. The wavelength of striations is observed to increase with time delay and it becomes nearly 3 mm at 2000 ns.

When the magnetic field was increased to 0.45 Tesla, the onset time of the striations is observed to be same as that for 0.32 Tesla. But the wavelength of the striations is reduced to 1.5 mm. Spatial structures are observed to be more uniform with increase in magnetic field. The wavelength of striations increases more with time compared to that of 0.3 Tesla. At 1600 ns time delay, the distance between two successive undulations is found to be 5 mm while it becomes 10 mm at 2000 ns. When the magnetic field is set to 0.52 Tesla, the onset time of striations is decreased to 800 ns. It is observed that the uniformity of distance between successive striations is more in the case of higher magnetic field. Similar to the case of 0.45 Tesla, the distance between the striations increases more in this case also.
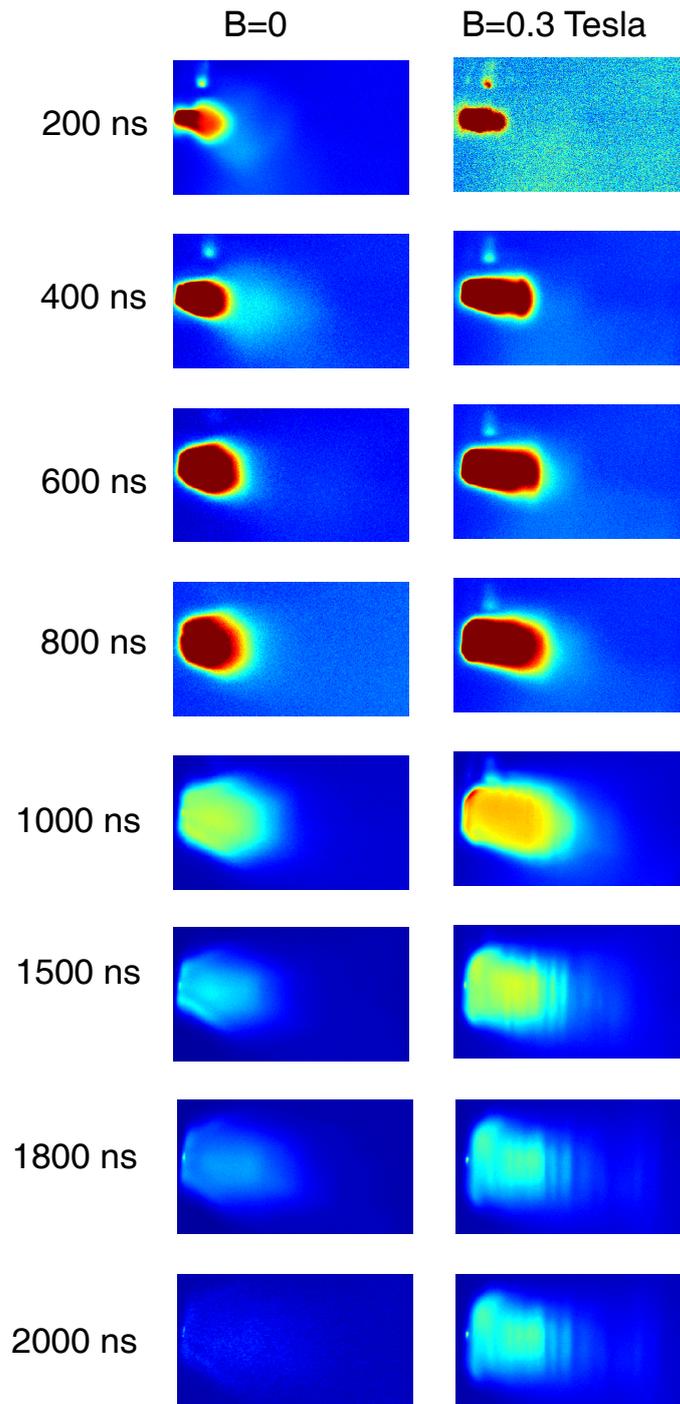
Figure 5.1 Images of plasma in the absence of magnetic field and presence of 0.3 Tesla magnetic field.

Images of plasma at different magnetic fields at a time delay of 1800 ns time delay are shown in Fig. 5.3 with corresponding intensity profiles. The intensity profiles are calculated using the Principal Component Analysis of the corresponding
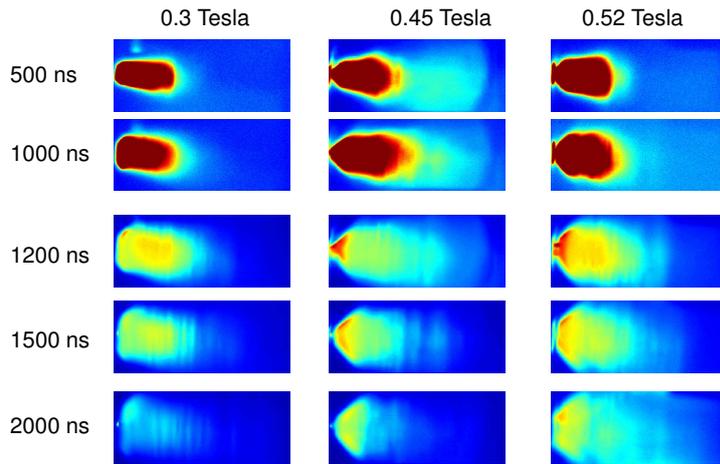
Figure 5.2 Images of tungsten plasma at different magnetic fields
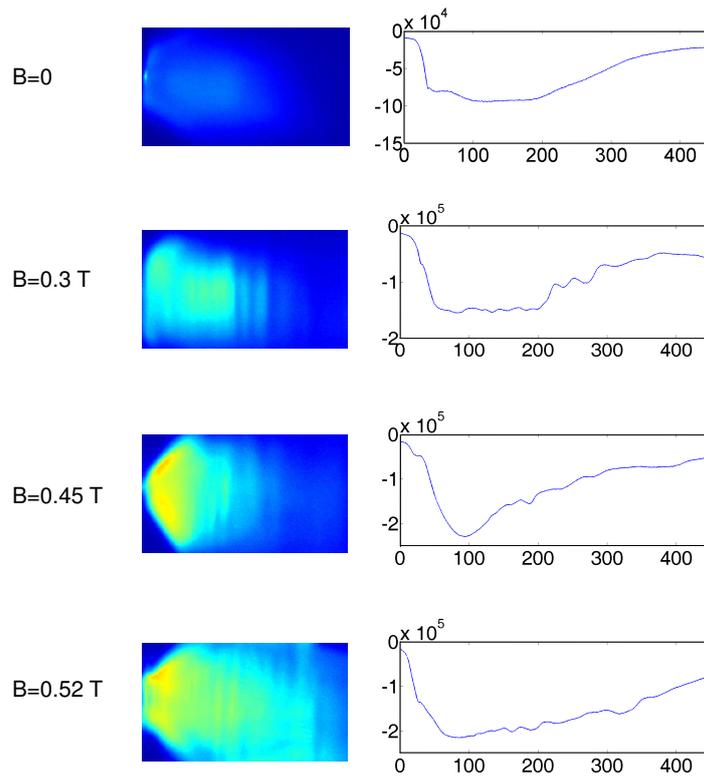
Figure 5.3 Intensity variation at different magnetic fields

images. Any image can be represented as a matrix and can be written as (Raju et al., 2011)

$$I_m = p_1 q_1 r_1^T + p_2 q_2 r_2^T + p_3 q_3 r_3^T + ... \tag{5.1}$$

where $p_1 q_1 r_1^T$, $p_2 q_2 r_2^T$ are called as first principal component, second principal component, etc., and give the variations in the intensity in the direction of maximum change in the intensity. Here p and r are unitary matrices while q is a diagonal matrix. Striations are clearly visible from this figure by means of variations in the intensity. From the figure, it is clear that the emission intensity increases in presence of magnetic field as observed in the earlier reports (Kumar et al., 2011a).

The field aligned striations observed above may be due to an instability in the plasma. Commonly possible instabilities in the laser produced plasmas includes Rayleigh-Taylor instability, large Larmor radius R-T instability, Kelvin-Helmholtz instability, electron-ion hybrid instability (Peyser et al., 1992), etc. Observed instability can be characterized by several factors such as condition for existance of such an instability, morphology, growth rate of the instability, etc. When the density gradient and acceleration of a hydrodynamic system are opposite to each other, such a system can be R-T unstable (Taylor, 1950). Laser plasma can also have R-T instability when it is expanding in an external magnetic field. In such a case, magnetic force due to the external magnetic field acts on the plasma with a density gradient. R-T instability is usually associated with a spike or a bubble morphology and its growth time is given by (Peyser et al., 1992)

$$\lambda_{RT} = (g_{eff}/L_n)^{-1/2} \tag{5.2}$$

where g_{eff} is the effective deceleration due to magnetic field and L_n is the density scale length. We have determined the effective deceleration due to magnetic field from the following relation

$$g_{eff}(t) = B^2 R^2(t)/2m_0 \tag{5.3}$$

where R is the radius of the plasma expansion and m_0 is the total mass ablated. Mass ablation rate $\dot{m}$ from a target depends on intensity (I_a), wavelength (λ) of the laser beam, atomic number of the target material (Z) and is given by (Dahmani,

1992)

$$\dot{m}_{exp}(\text{kg/s cm}^2) \simeq 65\Big(\frac{I_a(\text{W/cm}^2)}{10^{13}}\Big)^{5/9}\lambda^{-4/9}Z^{1/4} \qquad (5.4)$$

Estimated ablated mass using above relation in the present experiments is 0.11 μg. Corresponding to this ablated mass, the estimated effective deceleration is 5.75×10^{12} m/s^2. Density scale length of laser produced plasma is approximately equal to the product of the pulse width of the laser and the acoustic speed of the plasma (Max, 1982). In the present case, the speed of the plasma calculated from the images is 2×10^6 cm/s and gives a density scale length of 160 μm. So, the instability growth time, which is inverse of the growth rate turns out to be 5.37 ns. But, this is very small compared to the experimentally observed instability growth time of 1 μs (growth rate of 10^6 s^{-1}). In the present experimental conditions, estimated Larmor radii of electrons and ions are 0.0003 mm and 6 mm respectively. The gyro period of electrons is 1.5×10^{-10} s while that of ions is 2×10^{-5} s. So, the electrons are treated as magnetized and ions are treated as unmagnetized (Ganguli et al., 1988). Since the classical R-T instability requires magnetized ions (Haverkamp et al., 2008), this instability cannot occur in the present experiments. Thus, classical R-T instability is ruled out. The large Larmor radius R-T instability is possible only when the Larmor radius of ions is large compared to the density scale length of the plasma. The growth rate of this instability is more compared to that of classical R-T instability. In the present experiments, the Larmor radius of ions is around 81.7 mm, which is quite large compared to the density scale length. This instability is also restricted to the edges of the plasma while in our case, striations are extended almost upto the target. So, the observed instability may not be due to LLR R-T instability.

Instability of similar morphology as in the present experiments was observed by Peyser et al. (1992) and was attributed to electron-ion hybrid instability in laser produced plasma expansions across magnetic fields. The growth rate for this instability is given by

$$\tau_{LLR} = 2\pi/0.05\omega_{LH} \qquad (5.5)$$

where ω_{LH} is the lower hybrid frequency which is given by

$$\omega_{LH} = \frac{\omega_{pi}\Omega_e}{(\omega_{pe}^2 + \Omega_e^2)^{1/2}} \qquad (5.6)$$

where ω_{pe} is electron plasma frequency, ω_{pi} is ion plasma frequency and Ω_e is the electron cyclotron frequency. The estimated value of maximum growth time for the present experiments is 2 μs, which is very near to the observed value of 1 μs. Hence the observed instability in our case can be attributed to the electron-ion hybrid instability.

5.3.2 10^{-1} Torr Ambient pressure

Two-dimensional snapshots of the plasma expansion in the absence and presence of magnetic field at 10^{-1} Torr of ambient Ar pressure at different time delays are shown in Fig. 5.4. The field aligned striations observed in the case of 10^{-5} Torr pressure are not observed in this case. A fast narrow jet is observed at 400 ns time delay in the absence as well as presence of magnetic field. After 1500 ns, the trailing portion of the plume becomes thin while the leading narrow jet bulges to form an ellipsoid. Similar focussing effect in the intermediate pressure regime was also observed previously in Laser Blow Off (LBO) of LiF-C thin films in Ar ambient (George et al., 2010).

The focussing feature of the plasma at this pressure can be explained on the basis of secondary shock wave formation. When the expanding laser produced plasma interacts with the ambient gas via collisions, if the mass of the swept ambient gas is greater than the mass of the ablated plasma, it forms a classical Taylor-Sedov blast wave (Zeldovich et al., 2002). This external shock wave can be studied by using shadowgraphy (Harilal et al., 2012). The compressed gas layer behind the external shock wave gets highly ionized. The incoming laser pulse can be absorbed by this ionized gas layer to generate a Laser supported Detonation (LSD) Wave. Because of this, the electron temperature and electron density increases and the adjacent shock wave and vapor plume are heated non-uniformly.

B=0   B=0 .45 Tesla

200 ns

400 ns

600 ns

1000 ns

1500 ns

2000 ns

3000 ns

4000 ns

5000 ns
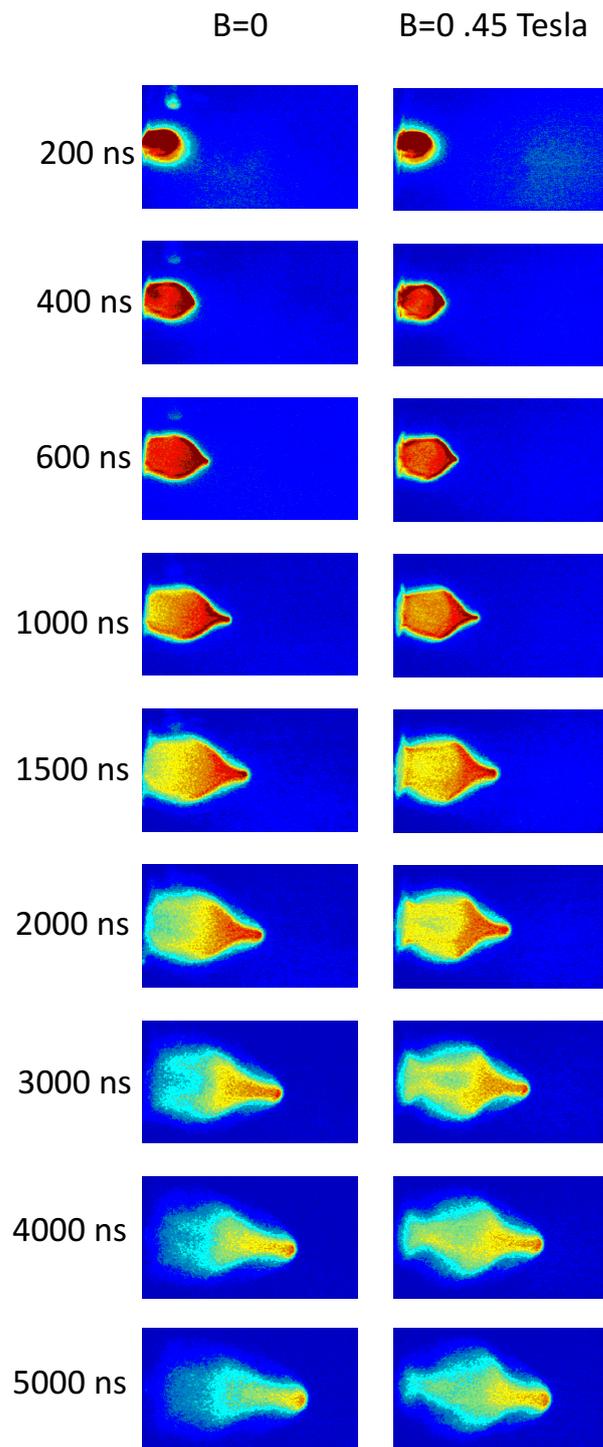
Figure 5.4 Images of plasma in the absence and presence of magnetic field at 10^{-1} Torr Ar pressure.

R-t Plots of the plasma plume front corresponding to the slow and fast components at 10^{-1} Torr Ar pressure are shown in Fig. 5.5. The propagation distance of the slow component is determined by assuming the plume front to be hemispherical. In the absence of magnetic field, the plasma follows a linear expansion.
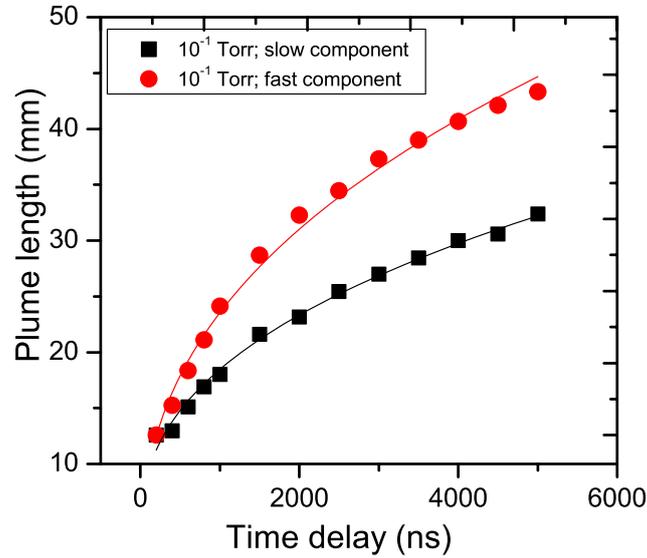
Figure 5.5 R-t plot of plasma plume in the absence of magnetic field

Velocity of the plasma in vacuum calculated from R-t plot is 2×10^6 cm/s. In the case of 10^{-1} Torr, it is observed that, the fast component which has a narrow jet shape is also effected by the ambient pressure. Both the slow and fast components are well fitted with the shock model (Zeldovich et al., 2002). Surprisingly, the effect of magnetic field appeared on the plasma at 10^{-1} Torr at very large time delay. In the absence of magnetic field, the trailing portion of the plume started to diminish after 3000 ns while in presence of field, it is narrowed down.

5.3.3   3 Torr Ambient pressure

The imaging results in the case of 3 Torr Ar pressure are shown in the Fig 5.6. At 200 ns, a disturbance is observed at the boundary of the plasma and it is extended to the interior of the plasma at later times. No significant difference is observed in the images in the absence and presence of magnetic field at this pressure. At this pressure, turbulence is observed in the plasma plume at 400 ns which may
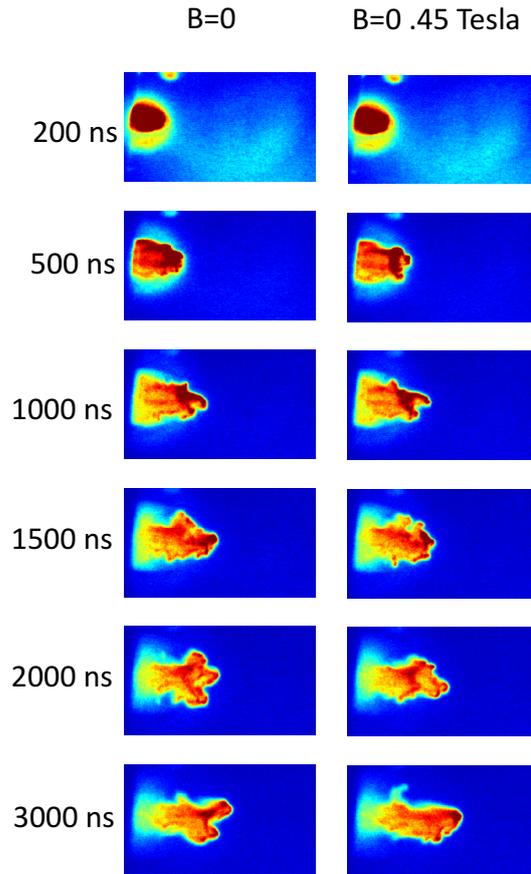
Figure 5.6 Images of plasma in the absence of magnetic field at 3 Torr Ar pressure.

be due to contact boundary instability such as Rayleigh-Taylor instability.

The growth rate for the R-T instability is given by

$$\eta^2 = -Ka\left(\frac{\rho_p - \rho_g}{\rho_p + \rho_g}\right) \tag{5.7}$$

where ρ_p and ρ_g are the densities of plasma and background gas respectively and a is the acceleration of the plume front. The plume is R-T unstable when the density of background gas is less than the plasma density (Sharma and Thareja, 2005). In our case, the perturbation occured on the plume boundary at 200 ns. The background gas density that can cause R-T instability is given by $\rho_b = 3m/4\pi R^3$ where R is

the plume length (George et al., 2009). The density estimated by this relation is $6.59 \times 10^{-4} \ kg/m^3$ which corresponds to a pressure of 3×10^{-1} Torr. Thus, the instability at a pressure higher than this may be due to R-T instability.

5.4 Imaging of Expanding Barium Plasma

Expanding barium plasma is studied by using fast imaging in presence of magnetic field 0.45 Tesla and various ambient pressures of Ar ($10^{-5}, 10^{-2}, 10^{-1}, 1$ and 3 Torr). The gate width of the ICCD was set to 5 ns while recording these images.

5.4.1 10^{-5} Torr Ambient Pressure

Two dimensional photographs of barium plasma expansion at different time delays from the laser pulse irradiation in the absence and presence of the 0.45 Tesla magnetic field at 10^{-5} Torr pressure are shown in Fig. 5.7. All these images are produced by single pulse of the laser. Each of these images represent spectrally integrated intensity emitted from different species in the wavelength region of 350-750 nm. These images may not represent the total flux because, a part of the plume is nonluminous. All the images in each of the given figures are normalized to the maximum intensity in that particular figure. The gate width or exposure time of the camera is kept as 5 ns in all these images to compare their relative intensity. In the absence of magnetic field, the structure of the plume is hemispherical similar to tungsten plasma. The emission intensity from barium plasma decreased with time, so images could not be recorded after a time delay of 2000 ns. The plume dynamics are observed to be entirely different in presence of magnetic field. The plume front of the plasma is flattened parallel to the magnetic field lines due to the magnetic pressure. The emission intensity of plasma increases in the presence of magnetic field. At a time delay of 1000 ns, irregularities originate at the plume boundary and develop into field aligned striations within the plume at higher time delays. These striations have well defined intensity pattern along the expansion direction. The striations are prominent after a distance of 14 mm from the target surface. So,
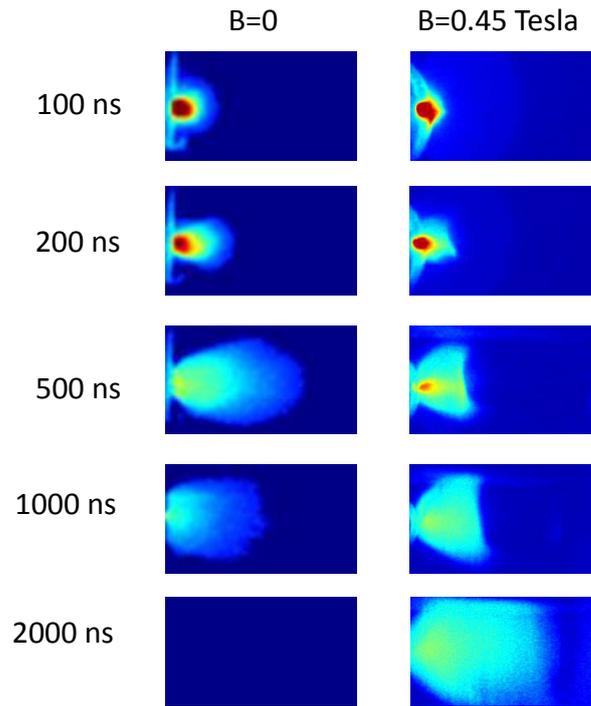
Figure 5.7 Images of barium plasma in the absence and presence of different magnetic fields.

these striations could not be observed through the time of flight profiles discussed in chapter 3.

Spatial and temporal evolution of barium plasma plume expanding in the presence of 0.45 Tesla magnetic field is shown in Fig. 5.8 using fast imaging. The effect of magnetic field can be observed after a time delay of 200 ns where the geometry of the plume is entirely different compared to the case of absence of field. Here it is worth to mention that the barium plasma did not show any fast component in presence of magnetic field where as the tungsten plasma showed a fast component around 400 ns in presence of magnetic field.

As the plasma expands, field aligned striations appeared in the plume similar to those discussed in tungsten plasma. The onset time of this instability is 1200 ns, which is slightly higher compared to that of tungsten plasma. At 1200 ns time delay, we can observe disturbance on the plasma boundary as shown in Fig.

50 ns			180 ns
100 ns			2000 ns
200 ns			2500 ns
500 ns			3000 ns
800 ns			3500 ns
1000 ns			4000 ns
1200 ns			4500 ns
1500 ns			5000 ns
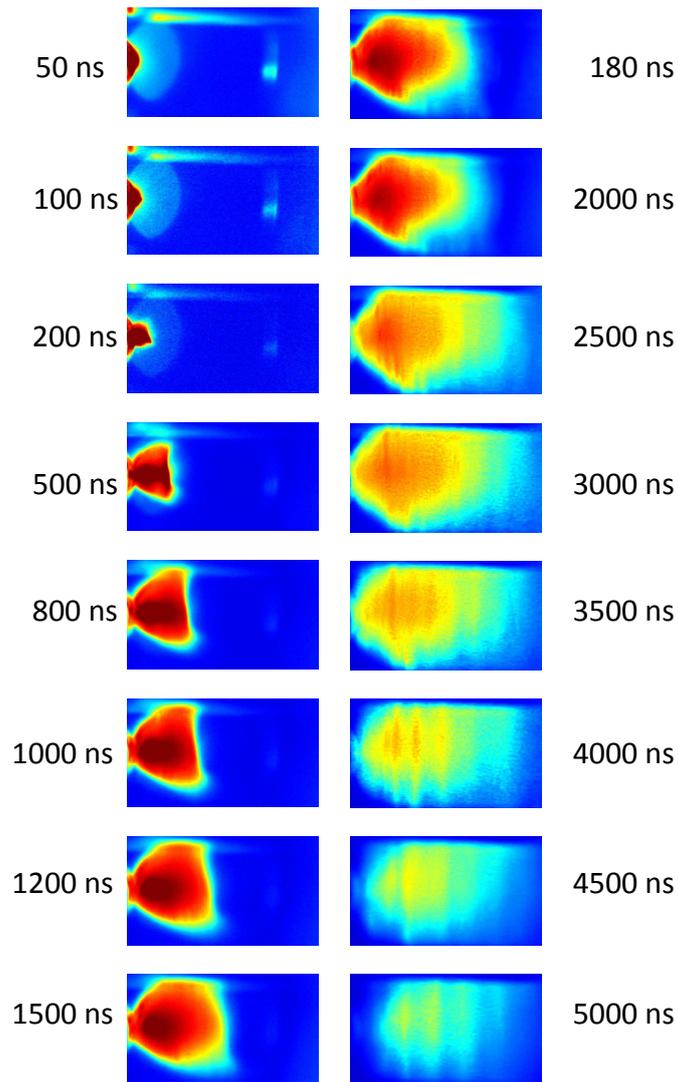
Figure 5.8 Images of barium plasma in the presence of 0.45 Tesla magnetic field in vacuum

5.8 while striations are very clearly visible at delays from 2500 ns.

5.4.2 10^{-2} Torr Ambient Pressure

Imaging results of expanding barium plasma in presence of 0.45 Tesla magnetic field at 10^{-2} Torr pressure are shown in Fig. 5.9. Even though the plume expansion is highly forward directed as in the case of 10^{-5} Torr pressure, the shape of the plume changes significantly at this pressure. Up to 1500 ns time delay, a distorted structure appeared in the front portion of the plasma. This may be due to

Figure 5.9 Images of barium plasma in the presence of 0.45 Tesla magnetic field in 10^{-2} Torr ambient Ar pressure

the Laser Supported Detonation (LSD) wave as discussed in the case of tungsten plasma. After 1500 ns, this front portion of the plume is merged with the bulk of the plume due to collisions with the ambient gas, and the shape of the plasma front becomes spherical as shown in the Fig. 5.9. It is also observed from the images that, unlike in the case of 10^{-5} Torr pressure, after a time delay of 1500 ns, the plasma plume is completely separated from the target in this pressure regime. The rear part of the barium plasma, which is nearer to the target, is also in spherical shape, where as tungsten showed planar shape. This may be because of the shape of the barium target which is cylindrical and plasma is produced on the curved surface while in the case of tungsten plate, the plasma is produced on the plane surface. Even though the

plasma expansion direction is perpendicular to the surface of the target, the shape of the rare part of the plasma plasma depends on the shape of the target.

5.4.3 10^{-1} Torr Ambient pressure

Imaging results of expanding barium plasma in presence of 0.45 Tesla magnetic field at 10^{-1} Torr pressure are shown in Fig. 5.10. In the barium plasma,
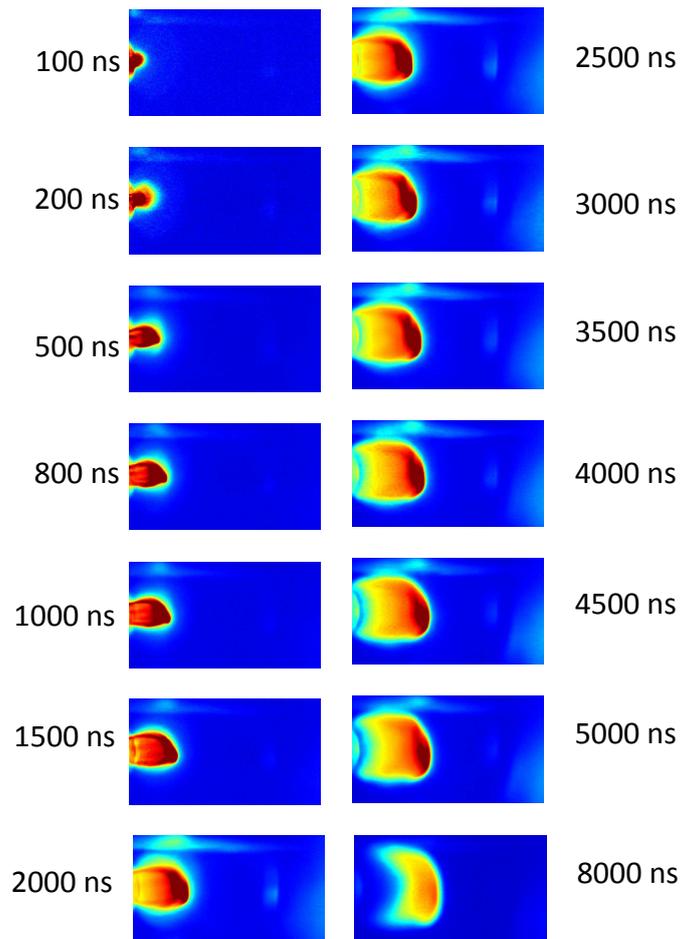
Figure 5.10 Images of barium plasma in the presence of 0.45 Tesla magnetic field in 10^{-1} Torr ambient Ar pressure

plume splitting is not observed where as tungsten plasma showed a fast component at the same pressure regime. The front part of the plume is more intense which can be attributed to the formation of Laser Supported Detonation (LSD) wave. Imaging results also showed that the dynamics of plasma at 10^{-1} Torr is similar to that at

10^{-2} Torr. The rear part of the plasma plume is completely detached from the target at 3000 ns in the case of 10^{-2} Torr pressure where as in case of 10^{-1} Torr pressure, it happened at 4500 ns. This may be due to the more thermalization of the plume at higher pressure.

5.4.4   1 Torr Ambient pressure

Imaging results of expanding barium plasma in presence of 0.45 Tesla magnetic field at 1 Torr pressure are shown in Fig. 5.11. At this pressure, a deviation from the usual spherical expansion of the plasma is observed in the plasma plume front at 800 ns. As the time delay increases, the disturbance can be seen clearly as R-T instability similar to that of tungsten plasma. It is observed that the growth time of instability in barium plasma is more compared to that of tungsten.

5.4.5   3 Torr Ambient pressure

2-D snapshots of barium plasma in presence of 0.45 Tesla magnetic field at 3 Torr pressure are shown in Fig. 5.12. There is no much difference between the dynamics of plasma plume at 1 Torr and 3 Torr pressures. Up to 1000 ns, a bright cloud appeared in the images at 3 Torr pressure. This may be due to the collissions of expanding electrons with the background gas. It is observed that the plasma plume front is smooth up to 800 ns and after that a distortion appears. This turbulence in the plasma plume is more in 3 Torr pressure compared to that of 1 Torr pressure. The non-uniformity of the plasma plume boundary at 1 Torr and 3 Torr can be attributed to the R-T instability as in the case of tungsten plasma. It is observed that tungsten plasma is more unstable compared to barium plasma. The the onset distance of the instability is nearly 5 mm in both 1 Torr and 3 Torr pressures.

5.4.6   R-t Plots at different ambient pressures

To understand the dynamics of plume at differnet Ar ambient pressures, we have plotted distance-versus time (R-t) plots and shown in Fig. 5.13. As shown
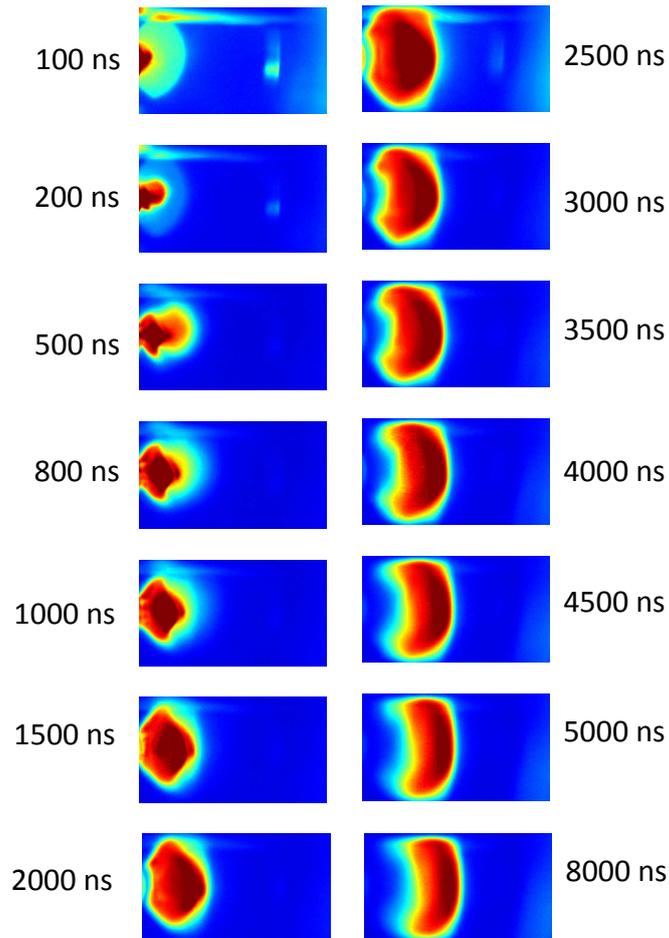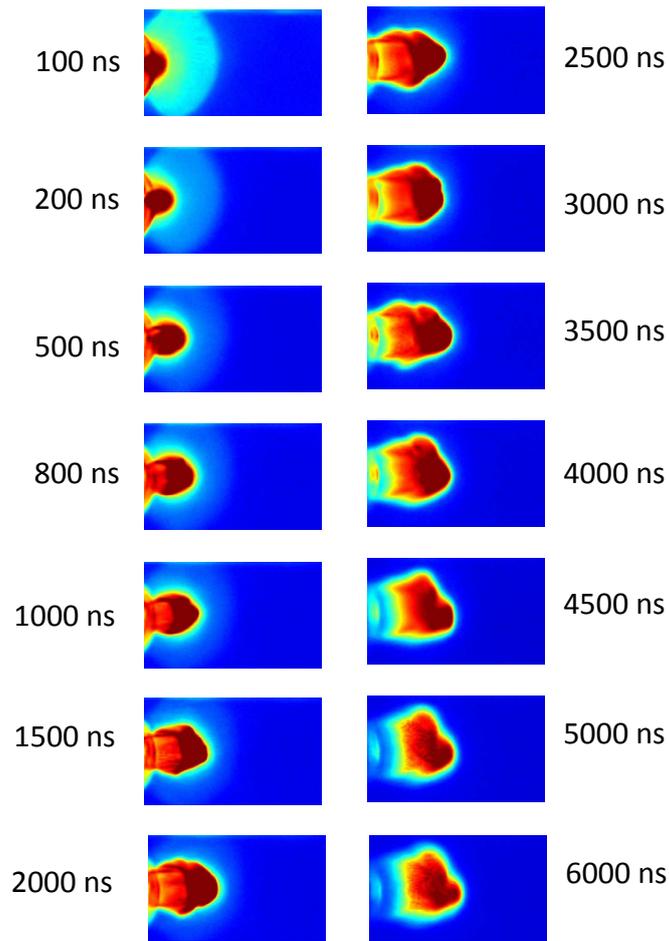
Figure 5.11 Images of barium plasma in the presence of 0.45 Tesla magnetic field in 1 Torr ambient Ar pressure

in the figure, the R-t plot showed retardation due to the magnetic field at 10^{-5} Torr pressure. The $z - t$ plots obtained from the time-of-flight profiles also shown deceleration in presence of magnetic field as discussed in section 3.3.5. It is also observed that, the plume is not fully stopped by the magnetic field and it penetrates through the magnetic field as observed in the previous experiments (Harilal et al., 2004). Around 2500 ns time delay, the plume is almost stagnant where after the plume length decreases because of recombination of ions and electrons. In the case of 10^{-2} Torr pressure, the R-t plot is similar to that of 10^{-5} Torr upto 600 ns.

After 1000 ns, the plume showed more retardation compared to the low background pressure. The plume at pressures of 10^{-1} Torr and 1 Torr shows same
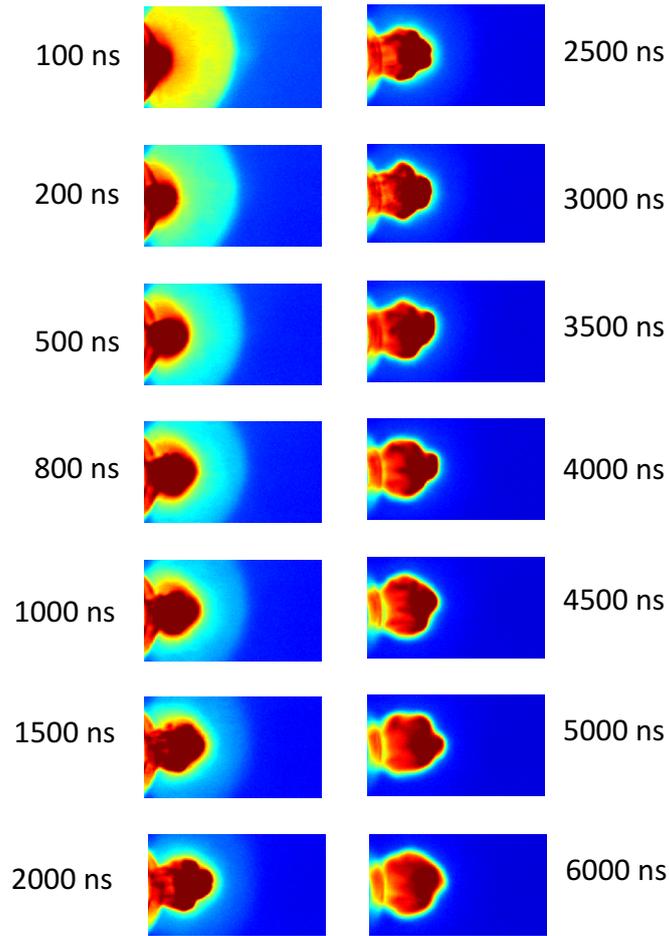
Figure 5.12 Images of barium plasma in the presence of 0.45 Tesla magnetic field in 3 Torr ambient Ar pressure

expansion radius upto 1500 ns whereas significant difference is observed between 1 Torr and 3 Torr pressures. In case of higher pressure of 3 Torr, the plume is almost stagnant after 2000 ns.

The plume dynamics in presence of ambient gas can be explained by various models. In the shock model, the expanding plasma ejected from the target accelerate the ambient gas to supersonic speeds and forms a shock wave. The shock wave position is defined by the Taylor-Seldov (T-S) theory of spherical blast waves emanating from strong point explosions as

$$R = \xi_0 \left(\frac{E_0}{\rho_0}\right)^{1/5} t^{2/5} \qquad (5.8)$$

here t is the time delay, ρ_0 is the ambient density , E_0 is the energy released during the explosion, and ξ_0 is a constant given by

$$\xi_0 = \left[\frac{75}{16\pi} \frac{(\gamma-1)(\gamma+1)^2}{(3\gamma-1)} \right]^{1/5}. \tag{5.9}$$

This model is valid at higher background pressures and at time delays after the formation of the shock. At low background pressure, and before the formation of shock, the plasma dynamics can be explained by drag model

$$R = R_0 \left(1 - exp(-\beta t)\right) \tag{5.10}$$

where R is the distance of the plume at a time t, R_0 is the stopping distance of the plume and β is the deceleration coefficient given by

$$R_0 \beta = v_0 \tag{5.11}$$

Here v_0 is the initial velocity of the ejected species. In the present experiments, the
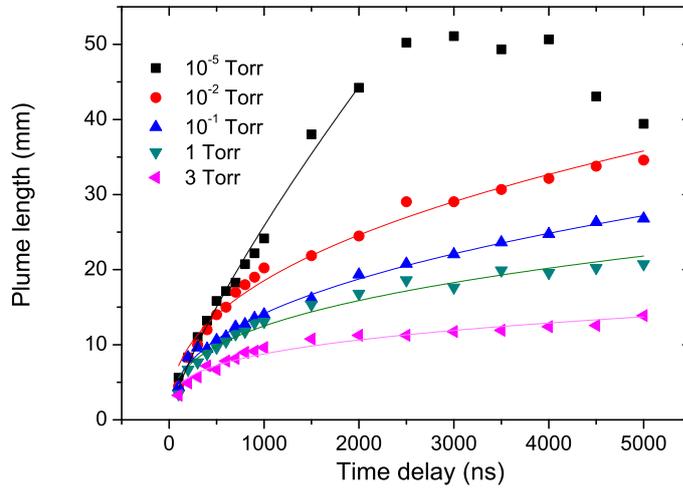
Figure 5.13 R-t plots of barium plasma at different ambient pressures

R-t plots of the plasma expansion could be best fitted with shock model $R = at^n$ where n varied from 0.35 for 3 Torr pressure to 0.409 for 10^{-2} Torr pressure.

5.4.7 Variation of Plume Length with Pressure

We have used the adiabatic expansion model to estimate the length of the plume at different ambient gas pressures (Harilal et al., 2003; Dyer, 1989). According to this model, expanding plasma pushes the background gas until the plasma and ambient pressures becomes equal. The maximum plume length of the plasma is given by

$$L = A[(\gamma - 1)E_0]^{1/3\gamma} \ P_g^{-1/3\gamma} V_p^{(\gamma-1)/3\gamma} \qquad (5.12)$$

Here A factor which depends on the expansion geometry and for a conical plume with an expansion angle θ, A is given by

$$A = \left(1 + \frac{1}{tan\ \theta}\right) \left(\frac{3\ tan\ \theta}{\pi + 2\ \pi\ tan\ \theta}\right)^{1/3} \qquad (5.13)$$

γ is the specific heat ratio of the gas, E_0 is the incident laser energy, P_0 is the ambient pressure, V is the initial volume of the plasma which can be estimated by $v_0 \tau_{laser} w_s$ where v_0 is the initial species velocity, τ_{laser} is FWHM of laser pulse, and w_s is the spot size at the target. By assuming $\theta = 10^0$, we have determined the plume length in various pressures, which are equal to 33 mm, 21 mm and 17 mm for the pressures 10^{-1} Torr, 1 Torr and 3 Torr. It is observed that there is a good agreement with the experimental values.

5.5 Conclusions

Fast imaging has been used to study the dynamics of tungsten and barium plasmas in presence of magnetic field and Ar ambient. Instability shown by these plasmas in presence of magnetic field in vacuum is discussed and electron-ion hybrid instability induced by the shear in the electron speed is identified as the potential mechanism for the observed instability. In case of tungsten plasma at 10^{-1} Torr ambient pressure, leading portion of the plasma forms a narrow jet due to the Laser Supported Detonation wave. Instability observed in the case of 3 Torr Ar ambient pressure is attributed to R-T instability due to the ambient gas.

CHAPTER 6

SUMMARY AND CONCLUSIONS

This chapter presents the summary of the results that are discussed in all the previous chpaters. Conclusions drawn from the present research work and possible future prospects are also discussed.

6.1   Summary

Irradiation of a material by a high power laser leads to rapid heating of the material and formation of the plasma. Laser produced plasma has many applications such as material characterization, pulsed laser deposition, laser plasma thruster, study of space plasmas, etc. External magnetic field can be used to control the dynamics of laser plasma. This thesis reports the effect of magnetic field on the dynamics and spectroscopy of barium and tungsten plasmas. The motive behind this study is applications of barium and tungsten in astrophysical and tokamak plasmas respectively. Optical emission spectroscopy, time-of-flight spectroscopy and fast imaging were the diagnostic tools used in the present studies.

A brief introduction to plasma and its diagnostics are given in chapter 1. Atomic processes, waves and instabilities in plasma and the applications of laser plasma are also discussed. A detailed literature review is also given in this chapter.

As a part of the research work, a magnetic trap was designed and developed for the study of plasma in an external magnetic field and three uniform magnetic fields of 0.3, 0.45 and 0.52 Tesla were obtained by varying the distance between the magnets as discussed in Chapter 2. Layout of the experimental setup, and specifications different components in the setup are also explained in this chapter. Different experimental techniques used in the present work have been discussed.

Dynamics and spectroscopy of the laser produced plasma are strongly effected by the external magnetic field. To get more insight into this, optical emission and time-of-flight spectroscopic studies of barium plasma expanding in vacuum have been carried out and reported in chapter 3. We have chosen two neutral and two ionic lines for this study. Dynamics of plasma were explained by plotting distance-time plots which indicated the confinement of plasma in presence of magnetic field. Electron temperature was estimated by the relative intensity of spectral lines while the electron density was measured by using stark broadened line. Electron density is observed to be less in presence of magnetic field compared to that of absence of field and attributed to magnetic confinement. Systematic study of the time-of-flight profiles at different distances has shown that the ionic profiles are temporally narrowed while the neutral profiles are broadened in presence of magnetic field. We have analysed the experimentally obtained temporal profiles by fitting with multi-component Shifted Maxwell Boltzmann (SMB) distribution . Possible mechanisms of populations of various SMB components are explained on the basis of collisions among the plume species and correlated to plasma parameters such as electron temperature, electron density, magnetic diffusion time, etc. The neutral profiles have shown three component structure where the first component is due to radiative cascade, second component is due to populations of meta-stable states while the third one is due to collisional or radiative cascading from the long lived Rydberg states. Ionic profiles could be best fitted with two SMB components, fast component is due to direct ablation while the slow component is due to super-elastic collisions. It is found that the relative intensity of spectral lines of singly ionized barium atoms decreases at higher fluence which may be due to increase of fraction of doubly ionized states at higher fluence.

Another major work that was carried out in this thesis is the study of effect of argon ambient gas on the expanding laser produced plasma in presence of magnetic field and is reported in Chapter 4. When the argon ambient is introduced, the temporal profiles of ions have shown a fast component due to the recombination of doubly ionized barium atoms with electrons. Results also indicated that ions are

completely ahead of neutrals in presence of magnetic field. It is observed that the temporal profiles of ionic lines are compressed significantly in the presence of magnetic field due to the resistive force by the magnetic pressure. By detailed analysis of the temporal profiles of ions at different distances, it is concluded that the ionic profiles have shown a pressure independent behaviour in presence of magnetic field at a distance of 6 mm from the target surface due to diamagnetic cavitization and a model is proposed. This observation is also correlated to the plasma parameters such as bubble radius, plasma beta, etc.

Intensity distributions of different components of temporal profiles in different pressures are analysed by fitting with multi-SMB distribution. It is observed that the intensity of fast component of neutral profiles decreased with pressure in the absence of magnetic field while the intensity increased with pressure in presence of magnetic field. Variation of laser fluence indicated a different behaviour of ions and neutrals in the absence and presence of magnetic field.

Chapter 5 is dedicated to the fast imaging studies of expansion of tungsten and barium plasmas in the absence and presence of different magnetic fields at various Ar ambient pressures. At 10^{-5} Torr pressure, plasma has shown a linear, hemi-spherical expansion in the absence of magnetic field while field aligned striations were observed in presence of magnetic field. Study of these striations at three different magnetic fields indicated that the separation of the striations decreases with increase in magnetic field. These striations are analysed by using Principal Component Analysis (PCA). It is proposed that instability is the possible reason for the striations in presence of magnetic field. Conditions, growth rates for different instabilities in a laser produced plasma were checked to identify the instability occurred in the present experiments. Electron-ion hybrid instability induced by the shear in the electron speed is identified as the potential mechanism for the observed instability.

The results of fast imaging of tungsten indicated that the leading portion of the plasma forms a narrow jet at 10^{-1} Torr pressure of argon due to heating of

123

plasma plume by Laser Supported Detonation (LSD) wave. At 1 Torr and 3 Torr pressures, barium and tungsten plasmas have shown R-T instability in the absence and presence of magnetic field.

6.2   Conclusions

Different components in the temporal profiles of expanding laser produced barium plasma could be resolved by fitting with Shifted Maxwell Boltzmann distribution. Electron temperature and density of the plasma are deduced by means of optical emission spectroscopy. Temporal of ions are compressed due to magnetic pressure while the neutral profiles are broadened due to collisions. Striations appeared at 10^{-5} Torr pressure in laser produced barium and tungsten plasmas in the presence of magnetic field are attributed to lower hybrid instability. R-T instability is appeared in expanding barium and tungsten plasmas at 1 Torr and 3 Torr pressures.

6.3   Future Prospects

The results of the experiments in the present thesis are useful in applications like pulsed laser deposition, laser plasma ion source, etc. The data gives more insight into the investigation of astrophysical plasmas using barium clouds. Study of tungsten plasma is useful in understanding the behaviour of tungsten as plasma facing components and plasma diagnostics in the fusion devices.

There is a scope of extending the present work by measuring the internal magnetic fields using magnetic probes. The theory of diamagnetic cavity and interpretation of the results can be made more strong by measuring these fields. Experimental estimation and three-dimensional mapping of magnetic field in a laser produced plasma gives insight of dynamics and instabilities of expanding plasma.

Magnetic reconnection is one of the possible phenomena that can happen in expanding laser produced plasma in presence of magnetic field. By measuring

the magnetic field evolution using proton radiographic images, we can understand the possibility of magnetic reconnection in nano second laser produced plasma. Double pulse experiments can be performed by confining the plasma produced by the first pulse using an external magnetic field. Other interesting work is, physics of colliding plasmas can be studied by confining plasmas with magnetic field. These experiments may give an insight into understanding astrophysical plasmas.

REFERENCES

1. Abdellatif, G. and Imam, H. (2002). A study of the laser plasma parameters at different laser wavelengths. *Spectrochimica Acta Part B: Atomic Spectroscopy*, 57(7):1155–1165.

2. Amamou, H., Bois, A., Ferhat, B., Redon, R., Rossetto, B., and Matheron, P. (2002). Correction of self-absorption spectral line and ratios of transition probabilities for homogeneous and LTE plasma. *Journal of Quantitative Spectroscopy and Radiative Transfer*, 75(6):747–763.

3. Amoruso, S., Bruzzese, R., Pagano, C., and Wang, X. (2007). Features of plasma plume evolution and material removal efficiency during femtosecond laser ablation of nickel in high vacuum. *Applied Physics A*, 89(4):1017–1024.

4. Amoruso, S., Bruzzese, R., Spinelli, N., and Velotta, R. (1999). Characterization of laser-ablation plasmas. *Journal of Physics B: Atomic, Molecular and Optical Physics*, 32(14):R131.

5. Amoruso, S., Sambri, A., and Wang, X. (2006). Propagation dynamics of a $LaMnO_3$ laser ablation plume in an oxygen atmosphere. *Journal of Applied Physics*, 100(1):013302.

6. Amoruso, S., Toftmann, B., Schou, J., Velotta, R., and Wang, X. (2004). Diagnostics of laser ablated plasma plumes. *Thin Solid Films*, 453:562–572.

7. Aragon, C., Bengoechea, J., and Aguilera, J. (2001). Influence of the optical depth on spectral line emission from laser-induced plasmas. *Spectrochimica Acta Part B: Atomic Spectroscopy*, 56(6):619–628.

8. Auciello, O. and Flamm, D. L. (2013). *Plasma Diagnostics: Discharge Parameters and Chemistry, Volume 1*. Academic Press.

9. Babushok, V., Jr., F. D., Gottfried, J., Munson, C., and Miziolek, A. (2006). Double pulse laser ablation and plasma: Laser induced breakdown spectroscopy signal enhancement. *Spectrochimica Acta Part B: Atomic Spectroscopy*, 61(9):999–1014.

10. Bachor, H. A. and Kock, M. (1981). Fast excitation and ionisation in a laser-pumped barium vapour: experiments and calculations. *Journal of Physics B: Atomic and Molecular Physics*, 14(16):2793.

11. Beiersdorfer, P., Olson, R. E., Brown, G. V., Chen, H., Harris, C. L., Neill, P. A., Schweikhard, L., Utter, S. B., and Widmann, K. (2000). X-ray emission following low-energy charge exchange collisions of highly charged ions. *Physical Review Letters*, 85(24):5090–5093.

12. Bellan, P. M. (2006). *Fundamentals of Plasma Physics*. Cambridge University Press.

13. Betti, R., Goncharov, V. N., McCrory, R. L., and Verdon, C. P. (1998). Growth rates of the ablative Rayleigh–Taylor instability in inertial confinement fusion. *Physics of Plasmas*, 5(5):1446–1454.

14. Bittencourt, J. A. (2013). *Fundamentals of Plasma Physics*. Elsevier.

15. Bleiner, D. and Lippert, T. (2009). Stopping power of a buffer gas for laser plasma debris mitigation. *Journal of Applied Physics*, 106(12):123301.

16. Borovsky, J. E. (1987). Limits on the cross–field propagation of streams of cold plasma. *Physics of Fluids (1958-1988)*, 30(8):2518–2526.

17. Bowley, H. J., Gerrard, D. L., Louden, J. D., Turrell, G., Gardiner, D. J., and Graves, P. R. (2012). *Practical Raman Spectroscopy*. Springer Science & Business Media.

18. Bret, A., Firpo, M., and Deutsch, C. (2005). Characterization of the initial filamentation of a relativistic electron beam passing through a plasma. *Physical Review Letters*, 94(11):115002.

19. Bulgakova, N. M., Bulgakov, A. V., and Bobrenok, O. F. (2000). Double layer effects in laser-ablation plasma plumes. *Physical Review E*, 62(4):5624–5635.

20. Camacho, J. J., Díaz, L., Santos, M., Juan, L. J., and Poyato, J. M. L. (2010). Time-resolved optical emission spectroscopy of laser-produced air plasma. *Journal of Applied Physics*, 107(8):083306.

21. Chen, F. F. (1984). *Introduction to Plasma Physics and Controlled Fusion Volume 1: Plasma Physics*. Springer US.

22. Chrisey, D. B. and Hubler, G. K. (1994). *Pulsed Laser Deposition of Thin Films*. Wiley New York.

23. Cirisan, M., Jouvard, J. M., Lavisse, L., Hallo, L., and Oltra, R. (2011). Laser plasma plume structure and dynamics in the ambient air: The early stage of expansion. *Journal of Applied Physics*, 109(10):103301.

24. Collette, A. and Gekelman, W. (2011). Structure of an exploding laser-produced plasmaa). *Physics of Plasmas*, 18(5):055705.

25. COMSOL Multiphysics Simulation Software (ver. 4.2), 2011 (https://www.comsol.co.in/comsol-multiphysics).

26. Cooper, J. (1966). Plasma spectroscopy. *Reports on Progress in Physics*, 29(1):35.

27. Cubaynes, D., Bizau, J. M., Wuilleumier, F. J., Carré, B., Roussel, F., Spiess, G., and Picqué, J. L. (1987). Electron spectrometry studies of collisional ionization in laser-excited barium vapour. *Europhysics Letters*, 4(5):549.

28. Dahmani, F. (1992). Ablation scaling in laser–produced plasmas with laser intensity, laser wavelength, and target atomic number. *Physics of Fluids B*, 4(6):1585–1588.

29. Davanloo, F., Juengerman, E. M., Jander, D. R., Lee, T. J., and Collins, C. B. (1990). Amorphic diamond films produced by a laser plasma source. *Journal of Applied Physics*, 67(4):2081–2087.

30. Dawson, J. M. (1964). On the production of plasma by giant pulse lasers. *Physics of Fluids*, 7(7):981–987.

31. Deutsch, C. and Tahir, N. A. (2006). Fusion reactions and matter-antimatter annihilation for space propulsion. *Laser and Particle Beams*, 24(04):605–616.

32. Dirnberger, L., Dyer, P., Farrar, S., and Key, P. (1994). Observation of magnetic-field-enhanced excitation and ionization in the plume of KrF-laser-ablated magnesium. *Applied Physics A*, 59(3):311–316.

33. Diwakar, P. and Hahn, D. (2008). Study of early laser-induced plasma dynamics: Transient electron density gradients via thomson scattering and stark broadening, and the implications on laser-induced breakdown spectroscopy measurements. *Spectrochimica Acta Part B: Atomic Spectroscopy*, 63(10):1038–1046.

34. Dreyfus, R. W. (1991). Cu^0, Cu^+, and Cu_2 from excimer-ablated copper. *Journal of Applied Physics*, 69(3):1721–1729.

35. Duan, B., Bari, M. A., Wu, Z. Q., Yan, J., and Li, Y. M. (2013). Electron-impact broadening parameters for Be II, Sr II, and Ba II spectral lines. *Astronomy & Astrophysics*, 555:A144.

36. Dyer, P. E. (1989). Electrical characterization of plasma generation in KrF laser Cu ablation. *Applied Physics Letters*, 55(16):1630–1632.

37. Ehler, W., Begay, F., Tan, T. H., Hayden, J., and McLeod, J. (1980). Effect of target purity on laser-produced plasma expansion. *Journal of Physics D: Applied Physics*, 13(2):L29.

38. Farid, N., Li, C., Wang, H., and Ding, H. (2013). Laser-induced breakdown spectroscopic characterization of tungsten plasma using the first, second, and third harmonics of an Nd:YAG laser. *Journal of Nuclear Materials*, 433(1):80–85.

39. Fridman, A. and Kennedy, L. A. (2004). *Plasma Physics and Engineering*. CRC Press.

40. Gambino, N., Hayden, P., Mascali, D., Costello, J., Fallon, C., Hough, P., Yeates, P., Anzalone, A., Musumeci, F., and Tudisco, S. (2013). Dynamics of colliding aluminium plasmas produced by laser ablation. *Applied Surface Science*, 272:69–75.

41. Ganguli, G., Lee, Y. C., and Palmadesso, P. J. (1988). Electron–ion hybrid mode due to transverse velocity shear. *Physics of Fluids*, 31(10):2753–2756.

42. Geohegan, D. B. (1992). Fast intensified-ccd photography of $YBa_2Cu_3O_7$ -x laser ablation in vacuum and ambient oxygen. *Applied Physics Letters*, 60(22):2732–2734.

43. Geohegan, D. B. and Puretzky, A. A. (1995). Dynamics of laser ablation plume penetration through low pressure background gases. *Applied Physics Letters*, 67(2):197–199.

44. George, S., Kumar, A., Singh, R. K., and Nampoori, V. P. N. (2009). Fast imaging of laser-blow-off plume: Lateral confinement in ambient environment. *Applied Physics Letters*, 94(14):141501.

45. George, S., Kumar, A., Singh, R. K., and Nampoori, V. P. N. (2010). Effect of ambient gas on the expansion dynamics of plasma plume formed by laser blow off of thin film. *Applied Physics A*, 98(4):901–908.

46. Goldstein, W. H., Walling, R. S., Bailey, J., Chen, M. H., Fortner, R., Klapisch, M., Phillips, T., and Stewart, R. E. (1987). Independent determinations of temperature and ionization balance in a laser-produced plasma by use of L-shell x-ray spectra. *Physical Review Letters*, 58(22):2300–2303.

47. Griegel, T., Drotleff, H. W., Hammer, J. W., and Petkau, K. (1990). The third continuum of the rare gases emitted by heavy ion beam induced plasmas. *The Journal of Chemical Physics*, 93(7):4581–4588.

48. Griem, H. R. (2005). *Principles of Plasma Spectroscopy*. Cambridge University Press.

49. Griem, H. R. (2012). *Spectral Line Broadening by Plasmas*. Elsevier.

50. Gupta, G. P. and Sinha, B. K. (1997). Effect of ionization and recombination coefficients on the charge-state distribution of ions in laser-produced aluminum plasmas. *Physical Review E*, 56(2):2104–2111.

51. Harilal, S. S., Bindhu, C. V., Tillack, M. S., Najmabadi, F., and Gaeris, A. C. (2002). Plume splitting and sharpening in laser-produced aluminium plasma. *Journal of Physics D: Applied Physics*, 35(22):2935.

52. Harilal, S. S., Bindhu, C. V., Tillack, M. S., Najmabadi, F., and Gaeris, A. C. (2003). Internal structure and expansion dynamics of laser ablation plumes into ambient gases. *Journal of Applied Physics*, 93(5):2380–2388.

53. Harilal, S. S., Miloshevsky, G. V., Diwakar, P. K., LaHaye, N. L., and Hassanein, A. (2012). Experimental and computational study of complex shockwave dynamics in laser ablation plumes in argon atmosphere. *Physics of Plasmas*, 19(8):083504.

54. Harilal, S. S., O'Shay, B., Tao, Y., and Tillack, M. S. (2006a). Ambient gas effects on the dynamics of laser-produced tin plume expansion. *Journal of Applied Physics*, 99(8):083303.

55. Harilal, S. S., O'Shay, B., Tao, Y., and Tillack, M. S. (2007). Ion debris mitigation from tin plasma using ambient gas, magnetic field and combined effects. *Applied Physics B*, 86(3):547–553.

56. Harilal, S. S., O'Shay, B., and Tillack, M. S. (2005a). Debris mitigation in a laser-produced tin plume using a magnetic field. *Journal of Applied Physics*, 98(3):036102.

57. Harilal, S. S., O'Shay, B., Tillack, M. S., Bindhu, C., and Najmabadi, F. (2005b). Fast photography of a laser generated plasma expanding across a transverse magnetic field. *Plasma Science, IEEE Transactions on*, 33(2):474–475.

58. Harilal, S. S., O'Shay, B., Tillack, M. S., and Mathew, M. V. (2005c). Spectroscopic characterization of laser-induced tin plasma. *Journal of Applied Physics*, 98(1):013306.

59. Harilal, S. S., Tillack, M. S., O'Shay, B., Bindhu, C. V., and Najmabadi, F. (2004). Confinement and dynamics of laser-produced plasma expanding across a transverse magnetic field. *Physical Review E*, 69(2):026413.

60. Harilal, S. S., Tillack, M. S., Tao, Y., O'Shay, B., Paguio, R., and Nikroo, A. (2006b). Extreme-ultraviolet spectral purity and magnetic ion debris mitigation by use of low-density tin targets. *Optics Letters*, 31(10):1549–1551.

61. Haverkamp, J. D., Bourham, M. A., Du, S., and Narayan, J. (2008). Plasma instabilities in magnetically assisted pulsed laser deposition. *Journal of Physics D: Applied Physics*, 41(11):115206.

62. Huba, J. D. (2004). NRL: Plasma formulary. Technical report, DTIC Document.

63. Hussain, S., Saleem, M., and Baig, M. A. (2006). Angular momentum dependence of photoionization cross sections from the excited states of lithium. *Physical Review A*, 74(5):052705.

64. Hutchinson, I. H. (2005). *Principles of Plasma Diagnostics*. Cambridge university press.

65. Instruction Manual, Acton Advanced Spectrograph SP2500A (http://www.princeton instruments.com).

66. Instruction Manual, Andor ICCD iStar (http://www.andor.com).

67. Instruction Manual, Continuum Powerlite 9030 (http://www.continuumlasers.com).

68. Instruction Manual, Goodfellow Inc., (http://www.goodfellow.com).

69. Instruction Manual, Hamamatsu PMT R943-02 (http://www.hamamatsu.com).

70. Instruction Manual, Hind High Vacuum, ED30 (http://www.hhv.in).

71. Instruction Manual, Horiba HR320 (http://www.horiba.com).

72. Instruction Manual, Pfeiffer Vacuum, TC 400 (http://www.pfeiffervacuum.com).

73. Instruction Manual, Plansee Inc., (http://www.plansee.com).

74. Instruction Manual, Stanford Computer Optics ICCD 4 Picos (http://www.stanford computeroptics.com).

75. Instruction Manual, Tektronix DPO 4104 (http://www.tek.com).

76. Issac, R., Varier, G., Gopinath, P., Harilal, S., Nampoori, V. P. N., and Vallabhan, C. (1998a). Prompt electron emission and collisional ionization of ambient gas during pulsed laser ablation of silver. *Applied Physics A*, 67(5):557–561.

77. Issac, R. C., Gopinath, P., Varier, G. K., Nampoori, V. P. N., and Vallabhan, C. P. G. (1998b). Twin peak distribution of electron emission profile and impact ionization of ambient molecules during laser ablation of silver target. *Applied Physics Letters*, 73(2).

78. Issac, R. C., Pillai, K. V., Harilal, S. S., Varier, G. K., Bindhu, C., Gopinath, P., Radhakrishnan, P., Nampoori, V. P. N., and Vallabhan, C. (1998c). Dynamics of laser produced silver plasma under film deposition conditions studied using optical emission spectroscopy. *Applied Surface Science*, 125(2):227–235.

79. Johnson, P. V., Eves, B., Zetner, P. W., Fursa, D., and Bray, I. (1999). Electron-impact excitation of the $(\ldots 6s5d\,^1D_2)$ to $(\ldots 6s6p\,^1P_1)$ transition in barium. *Physical Review A*, 59(1):439–454.

80. Jordan, R., Cole, D., and Lunney, J. (1997). Pulsed laser deposition of particulate-free thin films using a curved magnetic filter. *Applied Surface Science*, 109:403–407.

81. Kacenjar, S., Hausman, M., Keskinen, M., Ali, A. W., Grun, J., Manka, C. K., McLean, E. A., and Ripin, B. H. (1986). Magnetic field compression and evolution in laser-produced plasma expansions. *Physics of Fluids*, 29(6):2007–2012.

82. Kawasaki, H., Doi, K., Hiraishi, S., and Suda, Y. (2000). Effects of cross-magnetic field on thin film preparation by pulsed Nd:YAG laser deposition. *Thin Solid Films*, 374(2):278–281.

83. Kelley, M. C. and Livingston, R. (2003). Barium cloud striations revisited. *Journal of Geophysical Research: Space Physics*, 108(A1).

84. Kim, T. H., Nam, S. H., Park, H. S., Song, J. K., and Park, S. M. (2007). Effects of transverse magnetic field on a laser-produced Zn plasma plume and ZnO films grown by pulsed laser deposition. *Applied Surface Science*, 253(19):8054–8058.

85. Kokai, F., Koga, Y., and Heimann, R. (1996). Magnetic field enhanced growth of carbon cluster ions in the laser ablation plume of graphite. *Applied Surface Science*, 96:261–266.

86. Kramida, A., Yu. Ralchenko, Reader, J., and NIST ASD Team (2014). NIST Atomic Spectra Database (ver. 5.2), [Online]. Available: http://physics.nist.gov/asd . National Institute of Standards and Technology, Gaithersburg, MD.

87. Kroll, N. and Watson, K. M. (1972). Theoretical study of ionization of air by intense laser pulses. *Physical Review A*, 5(4):1883–1905.

88. Kumar, A., George, S., Singh, R. K., Joshi, H., and Nampoori, V. P. N. (2011a). Image analysis of expanding laser-produced lithium plasma plume in variable transverse magnetic field. *Laser and Particle Beams*, 29(02):241–247.

89. Kumar, A., Joshi, H., Prahlad, V., and Singh, R. K. (2010a). Effect of magnetic field on laser-blow-off plasma plume: Structured temporal emission profile. *Physics Letters A*, 374(25):2555–2560.

90. Kumar, A., Singh, R. K., and Joshi, H. (2011b). Effect of transverse magnetic field on the laser-blow-off plasma plume emission in the presence of ambient gas. *Spectrochimica Acta Part B: Atomic Spectroscopy*, 66(6):444–450.

91. Kumar, A., Singh, R. K., Prahlad, V., and Joshi, H. (2010b). Effect of magnetic field on the expansion dynamics of laser-blow-off generated plasma plume: Role of atomic processes. *Laser and Particle Beams*, 28(01):121–127.

92. Kumar, A., Singh, R. K., Prahlad, V., and Joshi, H. C. (2008). Comparative study of laser produced li plasma plumes from thin film and solid target. *Journal of Applied Physics*, 104(9):093302.

93. Kumar, A., Singh, R. K., Subramanian, K. P., Patel, B. G., Sunil, S., and Prajapati, I. A. (2006). Effects of ambient pressure and laser fluence on the temporal evolution of 426.7nm CII line in laser-blow-off of multilayered LiF-C thin film. *Journal of Physics D: Applied Physics*, 39(22):4860.

94. Kumar, A., Singh, R. K., Thomas, J., and Sunil, S. (2009). Parametric study of expanding plasma plume formed by laser-blow-off of thin film using triple langmuir probe. *Journal of Applied Physics*, 106(4):043306.

95. Kumari, S., Kushwaha, A., and Khare, A. (2012). Spatial distribution of electron temperature and ion density in laser induced ruby ($Al_2O_3 : Cr^{3+}$) plasma using langmuir probe. *Journal of Instrumentation*, 7(05):C05017.

96. Kwok, H., Kim, H., Kim, D., Shen, W., Sun, X., and Xiao, R. (1997). Correlation between plasma dynamics and thin film properties in pulsed laser deposition. *Applied Surface Science*, 109:595–600.

97. Li, Y., Hu, C., Zhang, H., Jiang, Z., and Li, Z. (2009). Optical emission enhancement of laser-produced copper plasma under a steady magnetic field. *Applied Optics*, 48(4):B105–B110.

98. Luke, J., Phipps, C., and McDuff, G. (2003). Laser plasma thruster. *Applied Physics A*, 77(2):343–348.

99. Lunney, J. G., Doggett, B., and Kaufman, Y. (2007). Langmuir probe diagnosis of laser ablation plasmas. *Journal of Physics : Conference Series*, 59(1):470.

100. Lv, G., Man, B., Zhang, Y., Liu, A., and Zhang, Q. (2004). Analysis of surface damage and plasma properties of pulsed laser ablation of gaas. *Optik - International Journal for Light and Electron Optics*, 115(8):347–350.

101. Manuel, M. J., Li, C. K., Séguin, F. H., Frenje, J., Casey, D. T., Petrasso, R. D., Hu, S. X., Betti, R., Hager, J. D., Meyerhofer, D. D., and Smalyuk, V. A. (2012). First measurements of Rayleigh-Taylor-induced magnetic fields in laser-produced plasmas. *Physical Review Letters*, 108(25):255006.

102. Matsuo, Y., Nakajima, T., Kobayashi, T., and Takami, M. (1999). Radiative lifetimes and collisional deactivation cross sections of the 5d6p states of laser-ablated Ba in He gas. *Physical Review A*, 59(3):2071–2077.

103. Matthews, G. F., Edwards, P., Hirai, T., Kear, M., Lioure, A., Lomas, P., Loving, A., Lungu, C., Maier, H., Mertens, P., Neilson, D., Neu, R., Pamela, J., Philipps, V., Piazza, G., Riccardo, V., Rubel, M., Ruset, C., Villedieu, E., Way, M., and the ITER-like Wall Project Team (2007). Overview of the iter-like wall project. *Physica Scripta*, 2007(T128):137.

104. Max, C. E. (1982). Physics of the coronal plasma in laser fusion targets.

105. McCavert, P. and Trefftz, E. (1974). Oscillator strengths of some Ba lines, calculated in MCHF approximation. *Journal of Physics B: Atomic and Molecular Physics*, 7(11):1270.

106. McKenna, N., Shah, N., Harilal, S. S., and Hassanein, A. (2014). Magnetic stopping of transient laser plasmas. *Plasma Science, IEEE Transactions on*, 42(10):2596–2597.

107. McNaught, A. D. and McNaught, A. D. (1997). *Compendium of Chemical Terminology, Volume 1669*. Blackwell Science Oxford.

108. Minami, H., Manage, D., Tsui, Y., Fedosejevs, R., Malac, M., and Egerton, R. (2001). Diamond-like-carbon films produced by magnetically guided pulsed laser deposition. *Applied Physics A*, 73(5):531–534.

109. Moeller, T. and Chang, Y. K. (2007). MACH2 simulations of a micro laser ablation plasma thruster. *Aerospace Science and Technology*, 11(6):481–489.

110. Mostovych, A. N., Ripin, B. H., and Stamper, J. A. (1989). Laser produced plasma jets: Collimation and instability in strong transverse magnetic fields. *Physical Review Letters*, 62(24):2837–2840.

111. N. R. Badnell, M. G. O'Mullane, H. P. Summers, Z. Altun, M. A. Bautista, J. Colgan, T. W. Gorczyca, D. M. Mitnik, M. S. Pindzola, and O. Zatsarinny (2003). Dielectronic recombination data for dynamic finite-density plasmas. *Astronomy & Astrophysics*, 406(3):1151–1165.

112. Neogi, A. and Thareja, R. K. (1999). Laser-produced carbon plasma expanding in vacuum, low pressure ambient gas and nonuniform magnetic field. *Physics of Plasmas*, 6(1):365–371.

113. Oraevsky, A., Da Silva, L., Rubenchik, A. M., Feit, M. D., Glinsky, M., Perry, M., Mammini, B., Small, W., and Stuart, B. C. (1996). Plasma mediated ablation of biological tissues with nanosecond-to-femtosecond laser pulses: relative role of linear and nonlinear absorption. *Selected Topics in Quantum Electronics, IEEE Journal of*, 2(4):801–809.

114. Orthaber, U., Petkovšek, R., Schille, J., Hartwig, L., Hawlina, G., Drnovšek-Olup, B., Vrečko, A., and Poberaj, I. (2014). Effect of laser-induced cavitation bubble on a thin elastic membrane. *Optics and Laser Technology*, 64:94–100.

115. Ovsyannikov, A. and Zhukov, M. F. (2000). *Plasma Diagnostics*. Cambridge Int Science Publishing.

116. Pagano, C., Hafeez, S., and Lunney, J. G. (2009). Influence of transverse magnetic field on expansion and spectral emission of laser produced plasma. *Journal of Physics D: Applied Physics*, 42(15):155205.

117. Pandey, P. K. and Thareja, R. K. (2013). Rotating copper plasmoid in external magnetic field. *Physics of Plasmas*, 20(2):022117.

118. Pant, H. C., Rai, V. N., and Shukla, M. (1998). Behavior of expanding laser produced plasma in a magnetic field. *Physica Scripta*, 1998(T75):104.

119. Pappas, D. L., Saenger, K. L., Bruley, J., Krakow, W., Cuomo, J. J., Gu, T., and Collins, R. W. (1992). Pulsed laser deposition of diamond–like carbon films. *Journal of Applied Physics*, 71(11):5675–5684.

120. Park, J. J., Song, J. K., Ha, J. S., and Park, S. M. (2012). The effects of magnetic field on pulsed laser deposition of Mg-doped ZnO thin films. *Applied Surface Science*, 258(22):8542–8547.

121. Patel, D. N., Pandey, P. K., and Thareja, R. K. (2013). Brass plasmoid in external magnetic field at different air pressures. *Physics of Plasmas*, 20(10):103503.

122. Pathak, K. A. and Chandy, A. J. (2009). Laser ablated carbon plume flow dynamics under magnetic field. *Journal of Applied Physics*, 105(8):084909.

123. Patra, A., Phukan, T., and Khare, A. (2005). Measurement of two-dimensional electron density profile in a low current spark using interferometry. *Plasma Science, IEEE Transactions on*, 33(5):1725–1728.

124. Peyser, T. A., Manka, C. K., Ripin, B. H., and Ganguli, G. (1992). Electron–ion hybrid instability in laser–produced plasma expansions across magnetic fields. *Physics of Fluids B*, 4(8):2448–2458.

125. Ping, Y., Sixing, Z., and Baowen, W. (1994). The preliminary experiments on laser ion source at IMP. *Review of Scientific Instruments*, 65(4):1275–1277.

126. Plechaty, C., Presura, R., and Esaulov, A. A. (2013). Focusing of an explosive plasma expansion in a transverse magnetic field. *Physical Review Letters*, 111(18):185002.

127. Pneuman, G. (1983). Magnetic flux expulsion as an acceleration mechanism for stellar winds. *Advances in Space Research*, 2(9):279–282.

128. Radziemski, L. J. and Cremers, D. A. (1989). Laser-induced plasmas and applications.

129. Raju, D., Kumar, A., and Singh, R. K. (2011). Study of laser-blow-off plume dynamics using singular value decomposition technique. *Plasma Science, IEEE Transactions on*, 39(2):630–636.

130. Raju, M. S., Singh, R. K., Gopinath, P., and Kumar, A. (2014). Influence of magnetic field on laser-produced barium plasmas: Spectral and dynamic behaviour of neutral and ionic species. *Journal of Applied Physics*, 116(15):153301.

131. Raju, M. S., Singh, R. K., Kumar, A., and Gopinath, P. (2015). Diamagnetic cavitization of laser-produced barium plasma in transverse magnetic field. *Optics Letters*, 40(10):2185–2188.

132. Ripin, B. H., McLean, E. A., Manka, C. K., Pawley, C., Stamper, J. A., Peyser, T. A., Mostovych, A. N., Grun, J., Hassam, A. B., and Huba, J. (1987). Large-larmor-radius interchange instability. *Physical Review Letters*, 59(20):2299–2302.

133. Riviere, P., Silva, R. E. F., and Martin, F. (2012). Pump-probe scheme to study the autoionization decay of optically-forbidden H_2 doubly excited states. *The Journal of Physical Chemistry A*, 116(46):11304–11310.

134. Rossa, M., Rinaldi, C. A., and Ferrero, J. C. (2009). Internal state populations and velocity distributions of monatomic species ejected after the 1064 nm laser irradiation of barium. *Journal of Applied Physics*, 105(6):063306.

135. Rothenberg, J. E. and Koren, G. (1984). Laser produced plasma in crystalline α-Al_2O_3 and aluminum metal. *Applied Physics Letters*, 44(7):664–666.

136. Rothenberg, J. E., Koren, G., and Ritsko, J. J. (1985). Temperature of molecular vapor in laser ablation of CuCl. *Journal of Applied Physics*, 57(11):5072–5074.

137. Rubenchik, A. and Witkowski, S. (1991). *Physics of Laser Plasma*. Elsevier Science Pub. Co., Inc; New York, NY (United States).

138. Rybicki, G. B. and Lightman, A. P. (2008). *Radiative Processes in Astrophysics*. John Wiley & Sons.

139. Shaikh, N. M., Rashid, B., Hafeez, S., Jamil, Y., and Baig, M. A. (2006). Measurement of electron density and temperature of a laser-induced zinc plasma. *Journal of Physics D: Applied Physics*, 39(7):1384.

140. Sharma, A. and Thareja, R. K. (2005). Plume dynamics of laser-produced aluminum plasma in ambient nitrogen. *Applied Surface Science*, 243(1):68–75.

141. Sharma, A. K. and Thareja, R. K. (2004). Characterization of laser-produced aluminum plasma in ambient atmosphere of nitrogen using fast photography. *Applied Physics Letters*, 84(22):4490–4492.

142. Shen, X. K., Lu, Y. F., Gebre, T., Ling, H., and Han, Y. X. (2006). Optical emission in magnetically confined laser-induced breakdown spectroscopy. *Journal of Applied Physics*, 100(5):053303.

143. Shen, X. K., Sun, J., Ling, H., and Lu, Y. F. (2007). Spectroscopic study of laser-induced Al plasmas with cylindrical confinement. *Journal of Applied Physics*, 102(9):093301.

144. Shiraishi, N., Kato, Y., Arai, H., Tsuchimine, N., Kobayashi, S., Mitsuhashi, M., Soga, M., Kaneko, S., and Yoshimoto, M. (2010). Room-temperature epitaxial growth of (Li,Ni)O thin film with Li content up to 60 mol %. *Japanese Journal of Applied Physics*, 49(10R):108001.

145. Signorell, R. and Reid, J. P. (2010). *Fundamentals and Applications in Aerosol Spectroscopy*. CRC Press.

146. Singh, J. P. and Thakur, S. N. (2007). *Laser-Induced Breakdown Spectroscopy*. Elsevier.

147. Singh, R. K., Kumar, A., Patel, B., and Subramanian, K. (2007). Role of ambient gas and laser fluence in governing the dynamics of the plasma plumes produced by laser blow off of LiF-C thin film. *Journal of Applied Physics*, 101(10):103301.

148. Singh, R. K. and Narayan, J. (1990). Pulsed-laser evaporation technique for deposition of thin films: Physics and theoretical model. *Physical Review B*, 41(13):8843–8859.

149. Singh, R. P., Gupta, S. L., and Thareja, R. K. (2013). Spectroscopic investigation of colliding plasma plumes. *Spectrochimica Acta Part B: Atomic Spectroscopy*, 88(0):54–62.

150. Singha, B., Sarma, A., and Chutia, J. (2001). Influence of magnetic field on plasma sheath and electron temperature. *Review of Scientific Instruments*, 72(5):2282–2287.

151. Smijesh, N., Chandrasekharan, K., Joshi, J. C., and Philip, R. (2014). Time of flight emission spectroscopy of laser produced nickel plasma: Short-pulse and ultrafast excitations. *Journal of Applied Physics*, 116(1):013301.

152. Smijesh, N. and Philip, R. (2013). Emission dynamics of an expanding ultrafast-laser produced Zn plasma under different ambient pressures. *Journal of Applied Physics*, 114(9):093301.

153. Spitzer, L. (2013). *Physics of Fully Ionized Gases*. Courier Corporation.

154. Stamper, J. A. (1991). Review on spontaneous magnetic fields in laser-produced plasmas: Phenomena and measurements. *Laser and Particle Beams*, 9(04):841–862.

155. Suckewer, S. and Fishman, H. (1980). Conditions for soft x-ray lasing action in a confined plasma column. *Journal of Applied Physics*, 51(4):1922–1931.

156. Tao, Y., Harilal, S. S., Tillack, M. S., Sequoia, K. L., O'Shay, B., and Najmabadi, F. (2006). Effect of focal spot size on in-band 13.5 nm extreme ultraviolet emission from laser-produced Sn plasma. *Optics Letters*, 31(16):2492–2494.

157. Taylor, G. (1950). The instability of liquid surfaces when accelerated in a direction perpendicular to their planes. I. *Proceedings of the Royal Society of London A: Mathematical, Physical and Engineering Sciences*, 201(1065):192–196.

158. Thareja, R. K., Saxena, H., and Narayanan, V. (2005). Laser-ablated ZnO for thin films of ZnO and $Mg_xZn_{(1-x)}O$. *Journal of Applied Physics*, 98(3):034908.

159. Timmer, C., Srivastava, S. K., Hall, T. E., and Fucaloro, A. F. (1991). Enhanced line emission from laser-produced plasmas. *Journal of Applied Physics*, 70(3):1888–1890.

160. Trinczek, M., Werdich, A., Mironov, V., Guo, P., Martínez, A. G., Braun, J., Urrutia, J. C. L., and Ullrich, J. (2006). A laser ion source for an electron beam ion trap. *Nuclear Instruments and Methods in Physics Research Section B: Beam Interactions with Materials and Atoms*, 251(1):289–296.

161. Uebbing, J., Brust, J., Sdorra, W., Leis, F., and Niemax, K. (1991). Reheating of a laser-produced plasma by a second pulse laser. *Appl. Spectrosc.*, 45(9):1419–1423.

162. Vadla, C., Niemax, K., Horvatic, V., and Beuc, R. (1995). Population and deactivation of lowest lying barium levels by collisions with He, Ar, Xe and Ba ground state atoms. *Zeitschrift für Physik D Atoms, Molecules and Clusters*, 34(3):171–184.

163. VanZeeland, M. and Gekelman, W. (2004). Laser-plasma diamagnetism in the presence of an ambient magnetized plasma. *Physics of Plasmas*, 11(1):320–323.

164. VanZeeland, M., Gekelman, W., Vincena, S., and Maggs, J. (2003). Currents and shear alfvén wave radiation generated by an exploding laser-produced plasma: Perpendicular incidence. *Physics of Plasmas*, 10(5):1243–1252.

165. Vertes, A., Gijbels, R., and Adams, F. (1993). *Laser Ionization Mass Analysis*. Wiley New York.

166. Wakiya, N., Muraoka, K., Kadowaki, T., Kiguchi, T., Mizutani, N., Suzuki, H., and Shinozaki, K. (2007). Preparation of ferromagnetic zinc-ferrite thin film by pulsed laser deposition in the magnetic field. *Journal of Magnetism and Magnetic Materials*, 310(2):2546–2548.

167. Wang, F., Fujioka, S., Nishimura, H., Kato, D., Li, Y., Zhao, G., Zhang, J., and Takabe, H. (2008). Charge-state distribution in a photoionized laser-produced plasma. *Journal of Physics: Conference Series*, 112(4):042004.

168. Zakharov, Y. (2002). Laboratory simulation of artificial plasma releases in space. *Advances in Space Research*, 29(9):1335–1344.

169. Zeldovich, I. B., Zeldovich, Y. B., and Raizer, Y. P. (2002). *Physics of Shock Waves and High-Temperature Hydrodynamic Phenomena*. Courier Dover Publications.

170. Zheng, Z., Gao, H., Gao, L., Xing, J., Fan, Z., Dong, A., and Zhang, Z. (2014). Laser plasma propulsion generation in nanosecond pulse laser interaction with polyimide film. *Applied Physics A*, 115(4):1439–1443.

LIST OF PAPERS BASED ON THESIS

PUBLISHED PAPERS

1. **Raju, M. S.**, Singh, R. K., Gopinath, P. and Kumar, A. (2014). Influence of magnetic field on laser-produced barium plasmas: Spectral and dynamic behaviour of neutral and ionic species. *Journal of Applied Physics*, 116(15), 153301.

2. **Raju, M. S.**, Singh, R. K., Kumar, A. and Gopinath, P. (2015) . Diamagnetic Cavitization of laser produced barium plasma in transverse magnetic field. *Optics Letters*, 40(10), 2185.

COMMUNICATED PAPERS

1. **Raju, M. S.**, Singh, R. K., Kumar, A. and Gopinath, P. Structure formation in laser produced tungsten plasma in presence of transverse magnetic field and ambient pressure. (Manuscript submitted to Physics of Plasmas)

PRESENTATIONS IN CONFERENCES

1. **Raju, M. S.**, Singh, R. K., Kumar, A. and Gopinath, P. (2012). Dynamics of Laser Produced Ba Plasma Expanding in Magnetic Field, 1st *PSSI-Plasma Scholars Colloquium PPSC-2012.* IPR, Gandhinagar, July 3-4, 2012.

2. **Raju, M. S.**, Singh, R. K., Kumar, A. and Gopinath, P. (2012). Effect of Uniform Magnetic Field on Laser Produced Barium Plasma, *IIST Research Scholars Day.* IIST, Thiruvananthapuram, December 17-19, 2012.

3. **Raju, M. S.**, Singh, R. K., Gopinath, P., A. and Kumar, A. (2013). Influence of Transverse Magnetic field on Barium Laser Produced Plasma using Time of Flight Spectroscopy, *DAE-BRNS National Laser Symposium (NLS-21).* BARC, Mumbai, February 6-9, 2013.

4. **Raju, M. S.**, Kumar, A. Gopinath, P. and Singh, R. K. (2013). Characteristic emissions from laser produced barium plasma in presence of transverse

magnetic field, *DAE-BRNS National Laser Symposium (NLS-21).* BARC, Mumbai, February 6-9, 2013.

5. **Raju, M. S.**, Singh, R. K., Gopinath, P. and Kumar, A. (2013). Effect of Magnetic Field at Different Pressures on the Laser Produced Barium Plasma, *Topical Conference on Atomic Processes in Plasmas (ISAMP-TC2013).* PRL, Ahmedabad, November 18-20, 2013.

6. **Raju, M. S.**, Singh, R. K., Kumar, A. and Gopinath, P. (2014). Intensity Dependent Confinement of Laser Produced Barium Plasma in a Transverse Magnetic Field, *International Conference on ULTRAHIGH INTENSITY LASERS 2014.* Goa, India, October 12-17, 2014.

7. **Raju, M. S.**, Singh, R. K., Kumar, A. and Gopinath, P. (2014). Spectral Behavior of Neutral Species in Laser Produced Barium Plasma in Ar Ambient and External Magnetic field, *DAE-BRNS National Laser Symposium (NLS-23).* SVU, Tirupati, December 3-6, 2014.

8. **Raju, M. S.**, Singh, R. K., Kumar, A. and Gopinath, P. (2014). Dynamics of Laser Produced Tungsten Plasma Expanding in a Transverse Magnetic Field, *20th National Conference on Atomic and Molecular Physics (NCAMP-XX).* IIST, Thiruvananthapuram, December 9-12, 2014.